Polyester Rope Analysis Tool

by

Juan Felipe Beltran
and
Eric B. Williamson
The University of Texas at Austin
Civil, Architectural and Environmental Engineering Department-STR

Final Project Report
Prepared for the Minerals Management Service
Under the MMS/OTRC Cooperative Research Agreement
1435-01-99-CA-31003
Task Order 17019
1435-01-04-CA-35515
Task Order 35981
MMS Project Number 369

and

OTRC Industry Consortium

May, 2006

OTRC Library Number: 5/06B171

For more information contact:

Offshore Technology Research Center
Texas A&M University
1200 Mariner Drive
College Station, Texas 77845-3400
(979) 845-6000

or

Offshore Technology Research Center
The University of Texas at Austin
1 University Station C3700
Austin, Texas 78712-0318
(512) 471-6989

A National Science Foundation Graduated Engineering Research Center

Acknowledgements

We wish to thank the Offshore Technology Research Center for providing financial support through their Cooperative Agreement with the Minerals Management Service and their Industry Consortium.

Abstract

The objective of this research is to develop a computational model to predict the response of synthetic-fiber ropes under both monotonic and cyclic loads. These types of ropes are believed to offer a better alternative to more traditional mooring systems for deepwater applications. Of particular interest for this study are the degradation of rope properties as a function of loading history and the effect of rope element failure on overall rope response.

A computational tool developed specifically for this research accounts for the change in rope properties as it deforms and the change in configuration of a rope cross-section due to the failure of individual rope components. The software includes both geometric and material nonlinearities, and it incorporates a damage index so the strength and stiffness degradation of the rope elements can be modeled. Following the failure of rope elements, the software considers the possibility that the failed rope elements can resume carrying their proportionate share of axial load as a result of frictional effects.

Using the computational model developed under this research, several rope geometries are studied. Virgin (i.e., undamaged) ropes and initially damaged ropes are considered. In all cases, experimental data for a monotonically increasing load are available for comparison with the analytical predictions. For most of the cases analyzed, the proposed numerical model accurately predicts the capacity of the damaged ropes, but the model overestimates the rope failure axial strain.

If failed rope elements resume carrying their proportionate share of axial load, numerical simulations demonstrate the existence of strain localization

around the failure region. Based on the damage model, damage localization occurs as well. This damage localization can cause the premature failure of rope elements and reduce the load capacity and failure axial strain of a damaged rope.

Possible extensions to the computational model include the treatment of variability in rope properties and a lack of symmetry of the cross-section. Such enhancements can improve the accuracy with which damaged rope response is predicted. With the availability of validated software, engineers can reliably estimate the performance of synthetic-fiber moorings so that the use of these systems can be used with confidence in deepwater applications.

Table of Contents

CHAPTER 1

Introduction

1.1 GENERAL BACKGROUND

Over the years, developments in the offshore industry have focused on deep and ultra-deep water (depths greater than 1700 meters) in order to explore new reservoirs of oil and gas. Conventional steel wire ropes and chains have been used in the past to moor floating platforms. As the exploration and production of oil and gas move to deeper and deeper water, conventional mooring systems are costly and may become unfeasible due to the high magnitude of vertical load (self-weight) and size of the anchor footprint needed.

One way to facilitate the exploration and production of oil and gas in (ultra) deep water is through the use of low-weight material to optimize the strength-to-weight ratio of the mooring system. In this context, synthetic-fiber ropes appear to be a promising alternative. Synthetic-fiber ropes offer several advantages over conventional mooring systems, such as substantial installation costs savings, reduced dead-weight loads, and reduction of the size of the seafloor footprint.

In order to illustrate the advantage of using synthetic-fiber ropes as a mooring system over conventional mooring systems, Figs. 1.1 and 1.2 show comparisons of strength and strength-to-weight ratio for steel rope (ST) and several types of synthetic-fiber ropes (PE: Polyethelyne, PP: Polypropelyne, NY: Nylon, PET: Polyester, AR: Aramid, HMPE: High Modulus Polyethelyne).

Considering Fig. 1.1, it is important to note that the current technology is capable of producing synthetic fibers stronger than steel, such as aramid and high modulus polyethelyne. Fig. 1.2 shows that synthetic-fiber ropes have greater strength-to-weight ratio than steel ropes. Thus, they appear to be a valid alternative for use with mooring systems for floating platforms in deep water.

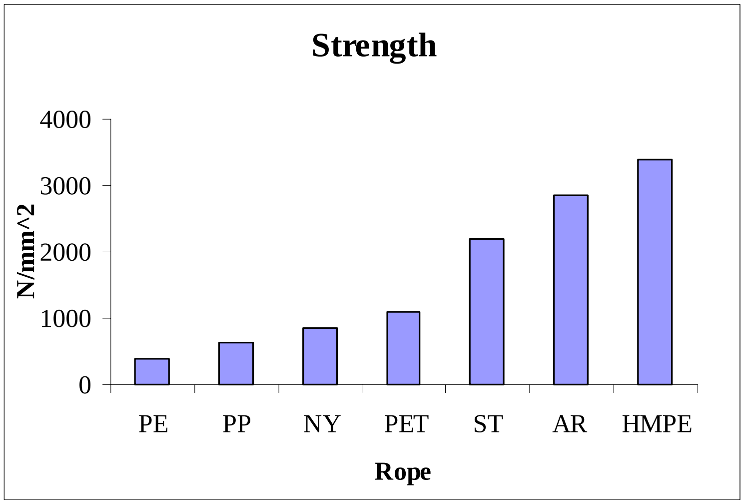

Fig. 1.1: Strength of steel and synthetic fibers

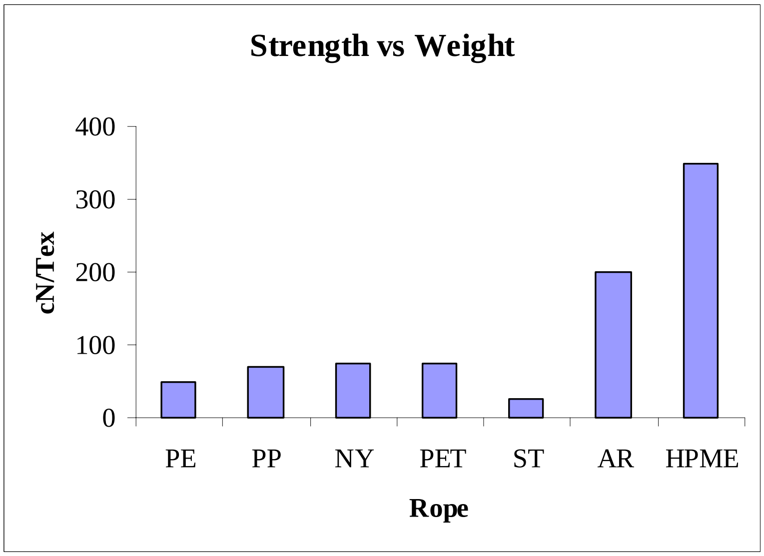

Fig. 1.2: Strength-to-weight ratio of steel and synthetic fibers

Synthetic-fiber ropes can either be used as taut-leg moorings or as insets in catenary mooring systems (Fig. 1.3). Taut-leg moorings rely on the elasticity of the mooring line to provide restoring forces that keep a platform in its desired position. Catenary moorings, however, rely on the weight of the mooring line to provide the restoring forces (Hooker, 2000).

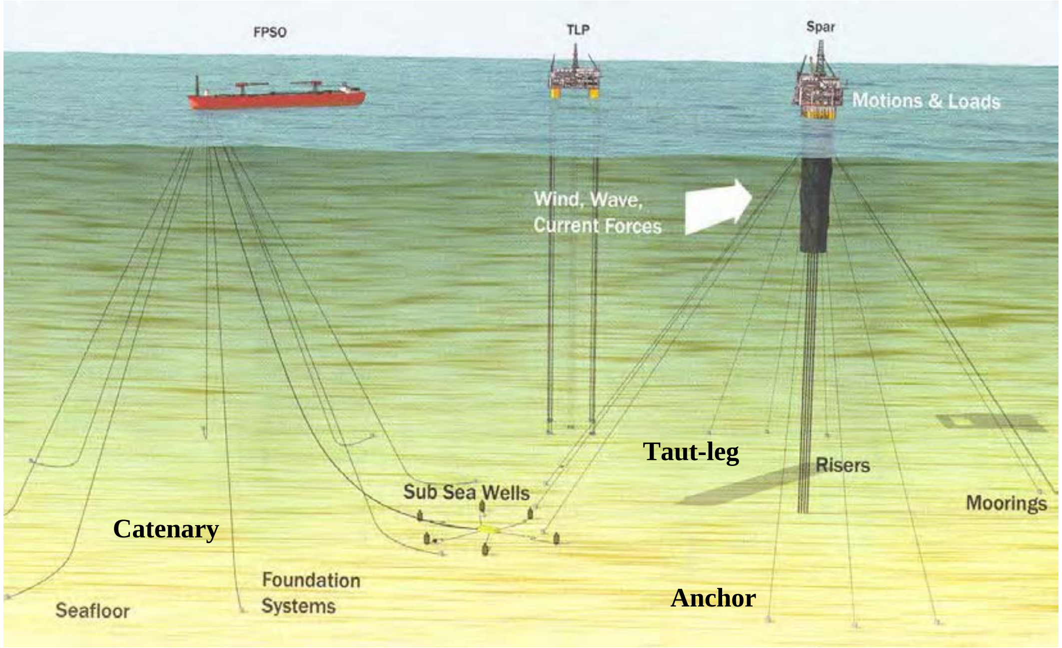

Fig. 1.3: Types of mooring systems: Taut-leg and catenary

Taut-leg moorings, in comparison to catenary moorings, give rise to a smaller sea floor footprint and can utilize shorter line lengths, but they require anchors that are capable of withstanding vertical load. Catenary moorings with synthetic inserts require long and heavy lengths of chain or steel wire rope near the seabed, but they can utilize standard drag anchors (Hooker, 2000).

The use of synthetic mooring lines in recent applications has brought to light several unknown aspects of behavior that can be categorized under the following headings (Hooker, 2000): (a) durability and (b) extension and modulus.

The durability of synthetic-fiber ropes is vital to their future success in offshore applications. Synthetic-fiber ropes in permanent mooring systems will need to exhibit design lives in excess of 20 years. When assessing the suitability for long-term design lives, it is important to first identify all the possible sources that could affect the performance of a mooring system. Some of these technical challenges are: special requirements during installation, complex loading history and associated time-dependent deformation during service, potential strength degradation due to hysteresis effects, seawater exposure, and fiber abrasion. These challenges may be overcome with long-term testing, development of models that can accurately predict deformation and failure, and additional field demonstration projects (Karayaka, et al., 1999; Hooker, 2000).

Extension (strength) and modulus characteristics are fundamental to the design of a mooring system because they determine the allowable loads and the vessel offset. The stiffness properties of synthetic-fiber ropes are generally not constant or linear. They can depend on time, tension history, temperature, moisture, and humidity. The slope of the load versus deformation plot becomes steeper with increasing tension. This nonlinear property is due to the characteristics of the synthetic-fiber ropes. The polymer fibers which make up a rope generally have nonlinear stress-strain behavior. Also, when tensioned, a rope structure compacts, decreasing the rope radius (r) and increasing the pitch distance, p, within the rope (Fig. 1.4). Typical synthetic-fiber rope curves can be reduced to a polynomial that can be used in static and dynamic analysis computer programs (Flory, 2001).

1.2 Research Objectives

The main purpose of the current study is to develop a computational model to predict the response of synthetic-fiber ropes under both monotonic and cyclic load. To investigate the effect of damage to a rope cross-section on overall rope response, a computational framework that quantifies the deterioration that takes place in a damaged rope throughout its loading history is needed. The computational model must be capable of tracing the behavior of a rope from its initial configuration to the onset of rope failure under the loads being considered.

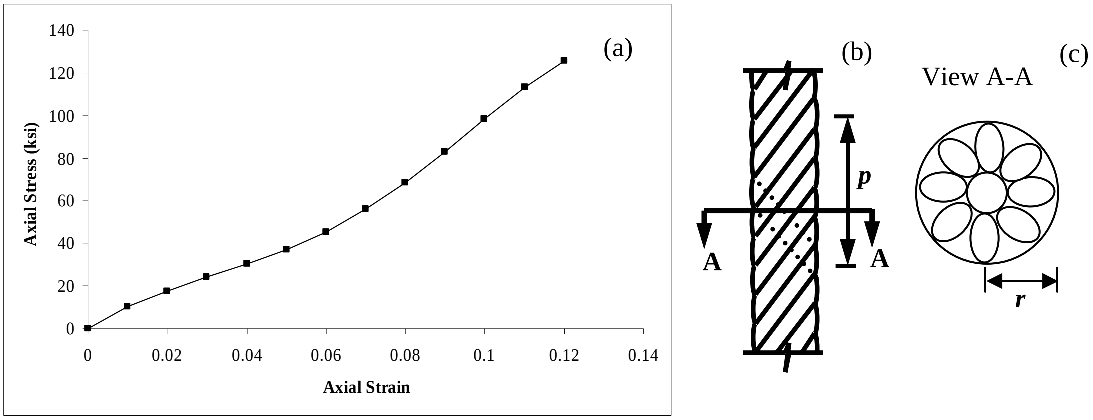

Fig. 1.4: (a) Stress-strain curve of a polyester rope, (b) rope pitch distance, and (c) rope radius

In order to include the deterioration experienced by ropes throughout their loading history, a damage model that evolves as a function of loading history is proposed. The failure of a synthetic-fiber rope is a complicated process that could depend on variety of factors. In this research, the combination of these factors is captured by the computation of a scalar quantity called the damage index parameter. In addition, by accounting for frictional effects, the ability of a failed rope component to resume carrying load is also considered in the predicted response. Using the developed computational model (presented in the subsequent chapters), analytical studies have been carried out to simulate damaged rope behavior.

1.3 Scope of Research

Additional background information and a literature review of rope modeling are presented in Chapter 2. Details of the most common rope cross-sections are also described along with their most common uses.

In Chapter 3, the modeling of synthetic-fiber ropes is presented. Details on the theoretical basis and formulation of the damage model to account for rope degradation are provided.

Calibration of the proposed damage model, based on experimental data, is discussed in Chapter 4. Analyses of synthetic-fiber ropes that are either damaged or undamaged prior to loading are presented. Modeling of softening behavior of synthetic-fiber ropes is also explained in this chapter.

A numerical procedure to estimate the effect of rope element(s) failure on overall rope response is presented in Chapter 5. Simulations of response for ropes that are damaged prior to loading, along with comparisons to experimental data, are also provided in this chapter.

In Chapter 6, a summary of the results obtained from the current research is presented. Conclusions are drawn regarding how synthetic-fiber ropes behave when loaded under monotonically increasing loads. In addition, opportunities for future research are identified.

CHAPTER 2

Background and Literature Review

This chapter consists of three sections. The first section provides an overview of the applications for ropes and cables in mechanical systems along with the most common materials used to construct them. The second section gives a general description of the available mathematical models to describe the behavior of these types of elements. In the third section, information about the most common type of rope constructions, including a summary of how such ropes are used, is provided.

2.1 BACKGROUND

The essential characteristic of a rope is that it has high axial strength and stiffness, in relation to its weight, combined with low flexural stiffness. This combination is achieved in a rope by using a large number of elements, each of which is continuous throughout the rope length. When loaded axially, each component within a rope provides tensile strength and stiffness, but when deformed in bending, the components have low combined bending stiffness provided their bending deformation is uncoupled. To facilitate handling, it is necessary to ensure that a rope has some integrity as a structure, rather than being merely a set of parallel elements. This characteristic is achieved by twisting the elements together (Chaplin, 1998).

2.1.1 Steel Wire Ropes

A rope can be a critical component in many engineering applications, including cranes, lifts, mine hoisting, bridges, cableways, electrical conductors, offshore mooring systems and so on. Different classes of ropes, suited for different purposes, have a different number and arrangement of rope elements within the rope cross-section, and rope elements can be made of different materials. Fig. 2.1 shows a longitudinal view of a steel wire rope. Its three basic components are the wire, the strand and the core (Schrems and Maclaren, 1997), and the typical cross-sectional arrangement of the elements include the spiral strand, six strand and multi-strand geometries (Chaplin, 1998).

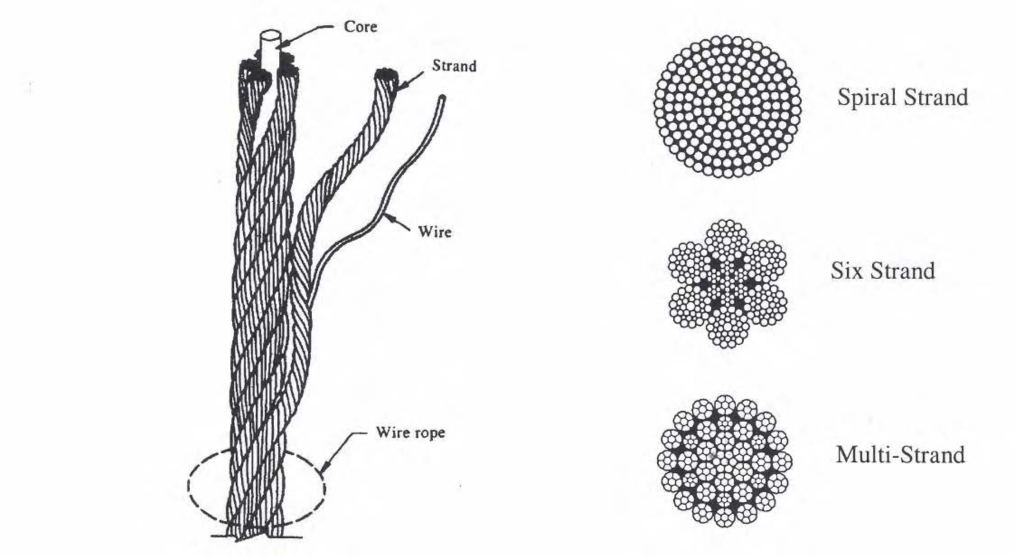

Fig. 2.1: Longitudinal view and typical types of steel rope constructions (Schrems and Maclaren, 1997; Chaplin, 1998)

The need to pull, haul, lift, hoist, hold or otherwise control objects has been a necessity since the beginning of civilization. In the earliest days, ropes were simply an assemblage of vines. Later, these assembles gave way to the use of vegetable or natural fibers from plants, usually original to a particular region. For example, the pyramids of Egypt and the Aztec dwellings, among others, could never have been built without these natural fiber ropes, quite probably aided by some mechanical schemes. The names for this assemblage of fibers twisted together in strands to form a strong, flexible and round strength member became cordage and rope (Foster, 2002).

As civilization became more progressive, so did the rope manufacturing. As McKenna et al. state "the Industrial Revolution (1800), which moved textile manufacturing in Britain and later elsewhere from cottages to factories, changed the yarn (fiber) production, including the preparatory stages of opening and cleaning, carding and drawing, from hand-spinning to machine processing". The most important consequence of the Industrial Revolution for the rope industry, however, resulted not from the machinery, but from the invention of steels that could be made into wires which could be assembled into wire ropes and cables. The usual construction was to wrap successive layers on top of each other, with alternating twist directions. Wire ropes came to dominate the newer engineering applications such as bridge cables, mine hoists, elevators, and cranes (McKenna et al., 2004).

The extensive use of steel wire ropes for load bearing elements is mainly due to the strength offered by steel coupled with the flexibility of rope construction, rope geometry and wire size that can be suited to the required application. Although a wire rope is essentially an element for transmitting a tensile load, the rope construction is such that the individual wires in a rope are subjected to bending and torsional moments, frictional and bearing loads, as well as tension. The magnitude and distribution of the stresses resulting from these loadings determine the overall rope response, which can be expressed in terms of the extension and rotation of the rope (Utting and Jones, 1984).

Over the years, each field of wire rope application has developed a specific body of knowledge, based on extensive testing and field experience, leading to empirical rules for each particular application. Unifying these empirical rules under some general mathematical and mechanical theory would allow a better understanding, and in the long term, a better prediction of the mechanical behavior of wire ropes as well as reduce the need for expensive tests under a variety of operating conditions. Thus, due to their extensive use and the need to predict their behavior, several researchers have presented analytical models that permit the calculation of wire rope response based on the wire material and geometry (Cardou and Jolicoeur, 1997).

2.1.2 Synthetic-Fiber Ropes

The birth of nylon polyamide fiber in the late 1930s started the concept of industrial-grade fibers. Fibers of higher tenacity (strength of a fiber of a given size) have since been developed. Some of these other fibers include nylon, polyester, polypropylene and polyethylene, making it possible to produce flexible tension members of much higher strength and durability (Foster, 2002). The second generation of synthetic polymer fibers consists of high-modulus fibers with low breaking extensions and tenacities more than twice that of nylon and polyester. The first high-modulus, high-tenacity (HM-HT) synthetic polymer fiber, which became available in the 1970s, was the para-aramid fiber (Kelvar). Kevlar was followed in the 1980s by high-modulus polyethylene (HMPE) fiber (Spectra, Dyneema), and more recently by fibers made of poly-para-phenylene bisoxazole (Zylon). The development of these new types of synthetic fibers has given to the cordage and rope industry the possibility to build high-strength members that can potentially replace steel wire ropes (Foster, 2002; McKenna et al., 2004).

2.2 LITERATURE REVIEW

In this section, a general description of mathematical models used to describe rope and cable behavior is given. The initial focus is on models that predict the behavior of steel wire ropes. These models have been studied in great detail due to the extensive use of steel wire ropes, and they are a starting point for developing a mathematical or analytical model to study synthetic-fiber rope behavior (Chapter 3). Following this initial discussion, a review of some experimental and analytical research conducted on synthetic-fiber rope behavior is presented.

2.2.1 Steel Wire Ropes Models

Several mathematical models are currently available to predict the response of twisted steel wire cables and aluminum conductor steel reinforced (ACSR) electrical conductors under axisymmetric loading (Jolicoeur and Cardou, 1991). In order to develop these mathematical models, some researchers such as Hruska (1951, 1952, and 1953), Machida and Durelli (1973), McConnell and Zemke (1982), Knapp (1975, 1979), Lanteigne (1985) and Costello (1990), among others, have used a discrete approach in which equations are established for each individual wire. Other researches such as Hobbs and Raoof (1982) and Blouin and Cardou (1989) have used a semi-continuous approach in which each wire layer is replaced by a transversely isotropic layer.

The aim of this section is to classify current discrete models based on the assumptions made in their development as well as by the manner in which they predict global cable deformation (axial strain and twist) under applied axial loads. In the literature, there are hundreds of works that could be classified as a discrete model, but just some of them are mentioned in this section. It should be noted, however, Costello (1978), Utting and Jones (1984) and Cardou and Jolicoeur (1997) have published detailed historical surveys of the available models to predict cable response.

Based on the works by Jolicoeur and Cardou (1991) and Cardou and Jolicoeur (1997), current discrete mathematical models can essentially be divided into two categories, which are based on the types of hypotheses employed: (a) fiber models, and (b) rod models.

2.2.1.1 Fiber Models

This type of model was developed by Hruska (1951, 1952, and 1953)**.** It is based on the simplest hypotheses: (a) no end conditions effects, although zero end rotation is assumed; (b) contact mode between wires is purely radial; (c) radial contraction is neglected; (c) wires are assumed to be subjected only to tensile forces, neglecting their flexural and torsional stiffness; (d) frictional forces are neglected and (f) wire deformations are small, obtained from purely geometrical considerations and expressed in terms of the axial strain and twist per unit length of the cable. The resulting stiffness matrix of the cable is linear, constant and symmetric. Hruska's equations were also rederived and extended by Knapp (1975, 1979), as well as by Lanteigne (1985), addressing the case of compressibility of the core and possibly large wire strains.

2.2.1.2 Helical Rod Models

These models are an extension of the fiber models. McConnell and Zemke (1982) simply added the sum of the torsional stiffness of all individual wires to the cable torsional stiffness, which is valid only for small ropes. Machida and Durelli (1973) and Knapp (1979) studied the effects of flexural and torsional stiffness of individual wires on the cable rigidity matrix. However, a more rigorous derivation was presented by Phillips and Costello (1973), based on the work by Love (1944) for curved rods, that leads to a set of nonlinear equations that have to be solved iteratively. In the first stage, it was assumed that no core was present and that frictional forces were negligible. The early models considered the effects of variations of helix angle and wire radius (Poisson's effect) in addition to lateral contact between the wires. Huang (1978) studied the problem of finite extension of an elastic strand including the radial constraint provided by the core to the helical wires, influence of Poisson effects on individual wires and frictional forces between wires.

Using the same approach, Costello (1983) studied the stresses in a multilayered cable, subjected to axial, bending and torsional loads. The resulting equations were linearized by Velinsky et al. (1984) considering small helix angles and still including radial contraction due to Poisson's effect. Although, no closed-form solutions were given for the cable stiffness matrix coefficients, these values were later obtained by Jolicoeur and Cardou (1991) by matrix inversion. Velinsky (1985) presented a general nonlinear theory to analyze multilayered cables. For the load range in which most of the wire cables are used, the author concluded that the nonlinear theory showed no significant advantage over the linear theory. Kumar and Cochran (1987) have also linearized Costello's equations including radial contraction, obtaining closed-form solutions for the analysis of elastic cables under tensile and torsional loads. Jiang (1995) has proposed a general linear and nonlinear formulation to analyze multilayered wire ropes. In his formulation, the rope is not treated as a collection of smooth rods (wires) as in previous works, but wires, strands and ropes are considered ropes by themselves, differing in their values of stiffness and deformation. Thus, according to this formulation, a rope is made up of smaller ropes which can give rise to complex cross-sections.

As mentioned by Samras et al. (1974), linearized models should satisfy the Maxwell-Betti reciprocity theorem. Accordingly, the stiffness matrix of a cable should be symmetric. In their work, Jolicoeur and Cardou (1991) showed that fiber models satisfy this condition while rod models deviate by a few percent. The origin of the lack of symmetry in the rod models was identified by Sathikh et al. (1996). In response to this finding, they developed a linear symmetric model based on the works by Wempner

(1981) and Ramsey (1988, 1990), and compared the relative significance of the individual contributions of wire forces and moments to the stiffness coefficients of the cable.

2.2.1.3 Semi-continuous Models

Hobbs and Raoof (1982) developed the Orthotropic Sheet Model (OSM) in which each wire layer is replaced with an orthotropic thin layer in a state of plane stress. In this model, four elastic constants are necessary. As Cardou and Jolicoeur (1997) stated, two of these constants are directly related to the properties of the wires considered as fibers. The other two constants are related to the contact stiffness between adjacent wires in the layer. The normal and tangential stiffness values are obtained from contact mechanics equations, using parallel cylinder results. Thus, this formulation is a mixed contact model in which in-layer lateral contact is considered as primary. Friction between adjacent wires is also included in the model, with a deformation process evolving gradually from a no-slip to a full-slip stage.

Another semi-continuous model was first developed by Blouin and Cardou (1989) and subsequently extended by Jolicoeur and Cardou (1994, 1996). This model also consists of replacing each layer with a hollow cylinder of orthotropic, transversely isotropic material. Cylinder thickness is arbitrary; thus the model is a three-dimensional one requiring five elastic constants. The following three principal directions are defined for the equivalent cylinder: radial, tangential and the longitudinal axis of the wires in the corresponding layer. Standard linear elasticity equations are then applied, resulting for the axial loading case in a set of ordinary differential equations (one for each layer). Among the five elastic constants, some can be used as free adjustable parameters or be estimated from the contact mechanics equations as in the case of OSM. This model has been described in detail by Jolicoeur and Cardou (1996).

2.2.2 Synthetic-Fiber Ropes Models

Synthetic-fiber ropes, which, unlike steel wire ropes, contain millions of fibers in their cross-sections, are extremely complicated structures, where the correct and detailed analysis of the mechanics is not easy to develop. This difficulty in modeling synthetic-fiber rope behavior arises mainly because of the varying nature of the fiber properties and the complexity of the rope geometry. Fiber moduli depend on prior loading history, currently applied load level, and changes in rope geometry that occur due to changes in load.

Most of the textile industry still relies on the traditional empirical approach for estimating rope behavior, but, in the last two decades, this situation has begun to change because synthetic-fiber ropes have started being used in demanding applications such as deepwater moorings. Much of the research on synthetic-fiber rope mechanics is based upon earlier work on the mechanics of twisted yarns described by Hearle (1969). This author, using an energy-based approach on the twisted continuous fibers following a helical geometry, considering only the tensile stress-strain properties of the rope components, established the equation to determine the axial stress in a yarn (formed by fibers) based on the deformation of the constituent fibers.

A major contribution to the modeling of synthetic-fiber rope behavior has been made by Leech (1987, 2002). The author assumes that the rope geometry has a hierarchical structure: the lowest structure in a rope is the textile yarn assembled from twisted fibers, and then the rope yarn is formed by twisting together a small number of textile yarns. The next structure, the strand, is formed by twisting a group of rope yarns. The final structure, the rope, is assembled from a small number of strands, often twisted together. In Fig. 2.2, the cross-section of a four-level rope is shown, where the structures considered are: fibers, rope yarn, strand and rope. Strains at each rope structure (or level) are determined by imposed deformations to the rope, using differential geometry concepts. External and internal forces are computed based on the principle of virtual work in which the strain energy is based only on the tensile stress-strain properties of the rope components. The model also addresses the effects of frictional forces, heat generation due to fiber hysteresis and fatigue on rope behavior (Banfield et al., 2001).

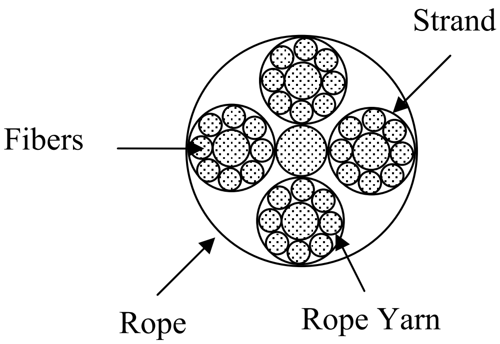

Fig. 2.2: Cross-section of a four-level rope

Some researchers, based on existing experimental data on yarns and ropes, have derived useful design information for synthetic-fiber ropes. Mandell (1987) proposed a model based on creep-rupture behavior of individual fibers and yarns to predict fatigue and abrasion failure for nylon and polyester ropes. Wu (1993) carried out experimental tests on double-braided (see Section 2.3.2) nylon and polyester ropes to study the effect of frictional constraints. In addition, he also investigated the slippage process between rope components that can cause abrasion failure. Banfield and Casey (1998) conducted experimental tests on aramid, polyester and HMPE ropes to evaluate several mechanical properties such as axial stiffness, modulus, hysteresis and elongation. Lo et al. (1999) established equations to account for the effects of creep deformation, estimated fatigue life, evaluated residual strength and remaining life, and considered long-term strength retention in polyester ropes subjected to a saline (i.e., sea water) environment. Fernandes et al. (1999), based on the work by Del Vecchio (1992), established an expression to deal with the nonlinear stiffness of polyester ropes, which depends on the average load, load amplitude and excitation period. Davies et al. (2000) presented regression analyses of tests on polyester ropes to evaluate their time-related mechanical properties. Creep and relaxation tests were conducted at different rope levels: fiber, yarn, rope yarn, sub-rope and ropes. Ghoreishi et al. (2004) presented a linearized model to predict the axial stiffness of small synthetic wire ropes based on the work presented by Labrosse et al.

(2000) and Nawrocki and Labrosse (2000). These authors also validated their model with experimental data and with a three-dimensional finite element rope model.

The development of mathematical models that can account for the degradation of the mechanical properties or damage of synthetic ropes during their loading history has also been a major focus of research. Karayaka et al. (1999) presented a damage model to predict the failure and residual strength of synthetic ropes due to creep and fatigue effects. Li et al. (2002) conducted experimental tests in small, damaged, synthetic-fiber ropes. The authors also presented a simple model to predict the breaking load of the damaged specimens tested. Beltran et al. (2003) and Beltran and Williamson (2004, 2005) validated the damage model proposed by Rungamornrat et al. (2002) and presented a methodology to estimate the evolution of damage in synthetic ropes under monotonically applied loads.

2.3 COMMON TYPES OF ROPE CONSTRUCTIONS

2.3.1 Overview

In Section 2.1, it was stated that the most common materials to build ropes are steel and synthetic fibers. In addition, Fig. 2.1 showed a longitudinal view of a steel wire rope along with the most common types of rope construction to clarify the ideas and concepts introduced. For additional details on steel wires rope constructions, readers are referred to, for example, the works by Walton (1996) and Chaplin (1998). Because the focus of the current study is on synthetic-fiber ropes, only these types of constructions will be considered in the current section and in the remainder of the document.

Synthetic ropes can be considered as structures made of textile fibers. As already discussed, ropes are defined as approximately cylindrical textile bodies whose cross-sections are small compared to their lengths, and they are primarily used as tension members. A synthetic rope structure contains large amounts of fibers in coherent, compact and flexible configurations, usually to produce a selected breaking strength and extensibility with a minimum amount of fibers (McKenna et al., 2004).

According to McKenna et al. (2004), synthetic-fiber ropes can be divided into two general categories: (1) laid and braided ropes and (2) low twist ropes. Laid and braided ropes are the most common structures for general purpose use. They are found in industrial, marine, recreation and general utility service. They include everything from small cords to large hawsers for mooring tankers. Conversely, low twist ropes are used for specialized and demanding applications where high strength-to-weight ratios and low extensibility are essential. Such situations include guys for tall masts, deep sea salvage recovery ropes, mooring lines for floating platforms and hoist cables for deep mines.

2.3.2. Common Synthetic-Fiber Rope Constructions

Leech (1987) established that the most common types of rope constructions used are 3-strand, 8-strand, double braided, parallel yarn/strand and wire ropes (Fig. 2.3). In the following subsections, each of these types of rope construction is described in detail.

2.3.2.1 Three-strand Laid Construction

The oldest and still the most widely used fiber rope structure consists of three strands laid together by a twisting process. The strands are laid (right helix: Z) in the opposite direction to the rope yarns (left helix: S) that make up the strand so that the rope yarns are nearly aligned with the rope axis. This orientation is the optimum arrangement for best external wear resistance (McKenna et al., 2004). Three-strand laid ropes are not torque free. Thus, if an axial force is applied to such a rope, the rope will rotate and tend to unwind as it elongates axially. Different types of fibers can be combined to construct a rope of this geometry. For example, the center of each strand may be made with polypropylene, and the rope yarns can be comprised of polyester. This arrangement has the benefits of the abrasion resistance of polyester on the outside coupled with the lightweight and lower cost of polypropylene on the inside. In general, three-strand laid ropes have lower strength and higher elongation than braided ropes of the same size and material. However, they have virtually identical strength/elongation properties as eight-strand ropes.

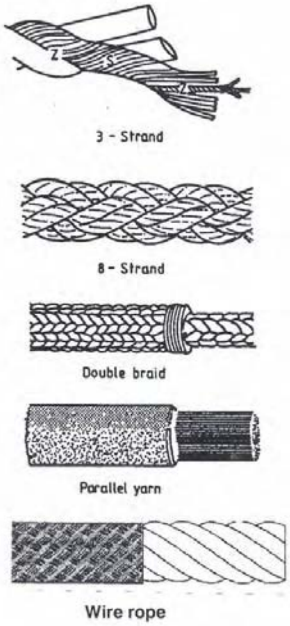

Fig. 2.3: Types of synthetic-fiber rope constructions (Leech, 1987)

2.3.2.2 Eight-strand Construction

The eight-strand construction is a torque balanced rope that is made by a braiding technique called plaiting. A braided structure has alternating strands laid in opposite directions. This construction can be made from the full range of high and low modulus fiber materials and can be used for general purposes as with three-strand ropes. Their typical applications are ship moorings and general utility service.

2.3.2.3 Double Braid Construction

A double braid rope is made by braiding a cover rope (sheath) over a braided core (Fig. 2.3). The tension in the rope is shared by both the core and cover. Most double braids are made of either all nylon or all polyester fiber, but combinations using different material may be found. High-modulus fibers in the cover and core result in inefficient load sharing between them and are rarely encountered. It should be noted that jackets of low-modulus fiber that do not support any load are often braided over a braided core of high-modulus fiber to provide abrasion protection. Although they have the appearance of a double braid construction, they are not considered as such (McKenna et al., 2004). Typical applications of double braid ropes are ship moorings and general utility service.

2.3.2.4 Parallel Yarn/Strand Construction

For the case of parallel yarn rope construction, a collection of a large number of parallel textile yarns, which may be enclosed in a jacket, form the rope structure. Because they lack twist or a helical construction, it is more difficult to achieve good load distribution among the fibers, particularly if high-modulus fibers are used, unless accurately controlled tension is maintained on all yarns as they are bundled into a rope (McKenna et al., 2004). Similarly to parallel yarn rope construction, strands in a parallel strand rope are aligned along the axis of loading of the rope. Strands are formed by many individual elements (rope yarns) held together by a braided jacket or twisted yarn bundles. A strand can be considered by itself to be a small rope and is often called a sub-rope. Strands can have a braided or laid structure. Parallel yarn rope construction, if carefully made and properly terminated, has very good strength efficiency. It is on the same order of magnitude as parallel strand and wire rope (see section 2.3.2.5) constructions. Their typical applications are antenna guys and moorings.

2.3.2.5 Wire Rope Construction

Synthetic-fiber ropes are often described as wire ropes when their cross-section resembles that of a steel wire rope. This rope construction was developed for fiber ropes because it achieved good fiber-to-rope strength with high modulus fibers such as aramid. Later, it was found to work well with low modulus fibers, especially polyester. Wire rope construction has low twist levels and a long pitch distance in the strands in order to achieve its high strength. A braided jacket is usually required to provide abrasion and snag protection. These types of ropes provide excellent tension-tension fatigue resistance and also perform well in bending fatigue. Their typical applications are moorings and dynamic applications such as lifting.

2.4 SUMMARY

It is well recognized that steel wire ropes have been used extensively as load-bearing elements due to the strength of steel coupled with the flexibility of rope construction, rope geometry and wire size that can be suited to the required application. For applications requiring tension members with high strength-to-weight ratios, the textile industry has been able to produce high-modulus fibers with high tenacities. Thus, the development of these new types of synthetic fibers has given to the cordage and rope industry the possibility to build high-strength members that can potentially replace steel wire ropes.

Several mathematical models are currently available to predict the response of twisted steel wire cables under axisymmetric loading. These models have been developed in great detail due to the extensive use of steel wire ropes. Based on the assumptions made in their development, the mathematical models can be classified as either discrete models or semi-continuous models. In the discrete models, equations are established for each individual wire. For the semi-continuous models, each wire layer is replaced by a transversely isotropic hollow cylinder. Both types of models compare well with experimental data, and their use depends on the problem under study.

For the case of synthetic-fiber ropes, few mathematical models have been developed to predict rope response. This situation exists in part due to the complexity of the rope geometry and the varying nature of the fiber properties coupled with the fact that the textile industry still relies on the traditional empirical approach for estimating rope behavior. However, this situation has begun to change because synthetic-fiber ropes have started being used in demanding applications such as deepwater moorings. Experimental tests on small and large ropes are being conducted along with the development of analytical models to study the behavior of rope response. The major concern of these studies is to evaluate and quantify the ability of synthetic ropes to withstand damage.

In the following chapter, the foundations of a mathematical model to predict synthetic-fiber rope response are presented. This model relies on the previous research conducted on steel wire ropes and synthetic-fiber ropes. The major contribution of the proposed model is the inclusion of a damage index, which quantifies the level of deterioration of rope properties when a rope is loaded. The model predictions are compared with available experimental data on virgin (i.e., undamaged) and on initially damaged ropes.

CHAPTER 3

Mathematical Modeling

In this chapter, an analytical model to predict the behavior of synthetic-fiber ropes is presented. The general assumptions made to develop the model are explained including the kinematics of deformation, constitutive models, cross-sectional behavior and equilibrium equations of a rope. This chapter also describes the use of a damage model, along with the use of a damage index, to account for strength and stiffness degradation.

3.1 KINEMATICS OF A ROPE

The mathematical description of the deformation of a rope element is described in this section. With this information known, the response of individual rope elements can be assembled to compute the response of an entire rope. Details are provided below.

3.1.1 Structure of a Synthetic-Fiber Rope

A synthetic-fiber rope is defined as a structural element constructed by twisting all components in hierarchical order. A typical rope consists of many levels of components. The diagram below and Fig. 3.1 show the typical hierarchy ranking from the highest to the smallest level (Liu, 1989, 1995; Leech, 2000).

$$\text{Rope} \rightarrow \text{Sub-rope} \rightarrow \text{Strand} \rightarrow \text{Rope yarn} \rightarrow \text{Textile yarn} \rightarrow \text{Fiber}$$

Thus, the rope itself is defined as level 1, and its components (e.g., sub-ropes and strands) comprise the structure at the second and third levels, respectively. This naming convention applies to all levels of a rope. Accordingly, level j includes all components in level j+1, which in turn includes all components in level j+2, etc. For example, Fig. 3.2 shows a rope cross-section with two levels of helical geometry because each sub-rope contains its own core element with components (strands) wound around the axis of the sub-rope. A complete description of the cross-section of each level is also presented in

Fig 3.2. Note that the components appear elliptical in cross-section due to the projection of the helix angle onto the section shown.

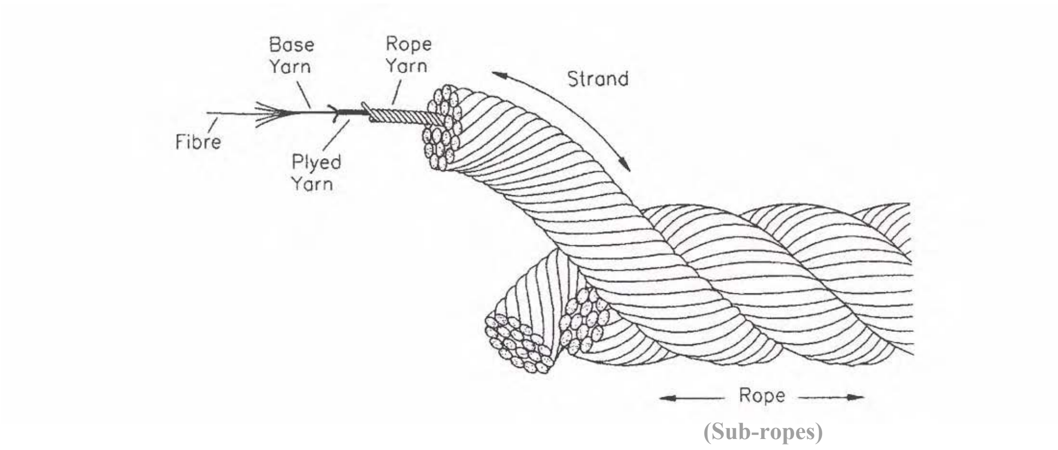

Fig. 3.1: Hierarchy ranking of rope elements

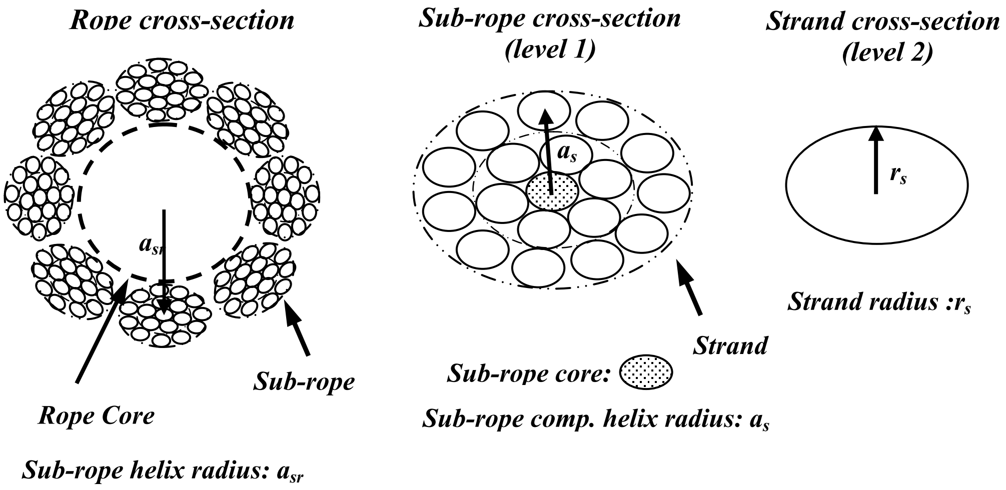

Fig. 3.2: Rope elements cross-section at different rope levels

3.1.2 Initial and Deformed Configuration of a Rope

A rope element is a structural element whose cross-section is small compared to its length. The so-called plane-sections hypothesis is assumed: rope element cross-sections that are plane before deformation remain plane after deformation, thus the motion of a rope element is described in terms of parameters that are a function of only its axial coordinate. It is assumed that in the deformed and initial configurations, the geometry of a rope element, represented by its centerline (longitudinal or helix axis), can be described by a circular helix curve. Curves in space can be seen as paths of a point in motion. In a Cartesian coordinate system, every point P of a curve C can be uniquely determined by its position vector $\boldsymbol{OP} = \boldsymbol{u}(\phi) = (x(\phi), y(\phi), z(\phi))$ where ϕ is a real variable defined in a closed interval I: $\phi_1 \leq \phi \leq \phi_2$. The position vector $\boldsymbol{u}(\phi)$ is called the parametric representation of the curve C, and the variable ϕ is called the parameter of this representation (Fig.3.3).

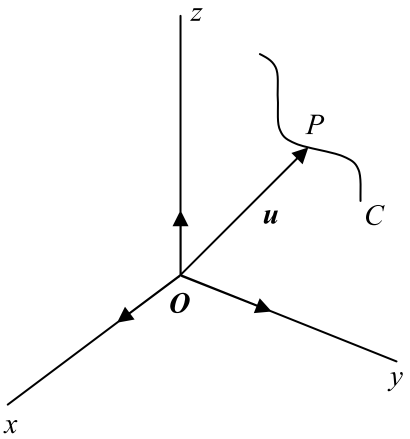

Fig. 3.3: Generic point *P* of a curve *C*

Two assumptions are made on the parametric representation $\boldsymbol{u}(\phi)$ of any curve C: (1) The functions $x(\phi)$, $y(\phi)$ and $z(\phi)$ are r (≥ 1) times continuously differentiable in I (where the value of r will depend on the problem under consideration); (2) For every value of ϕ in I, at least one of the three functions $dx(\phi)/d\phi$, $dy(\phi)/d\phi$ and $dz(\phi)/d\phi$ is different from zero. A parametric representation ***u(ϕ)*** of the a curve *C* satisfying these conditions is called an allowable parametric representation (Kreyszig, 1991).

Based on the descriptions given in Figs. 3.1 and 3.2, rope geometry can be represented by an n^{th} order helix (Lee, 1991). A 1-level rope can be represented by a single helix, because rope components are wound around a vertical axis (rope core) arranged in different layers. A 2-level rope can be represented by a double helix. Rope components of the second level can be represented by a single helix, but these components form the rope components of the first level, which has its own helical geometry. Accordingly, a 2-level rope possesses a double helix structure. Ropes that can be modeled with multiple levels generate multiple helix rope geometry.

The modeling of rope geometry follows a hierarchical approach with a defined number of levels, which mirrors the manufacturing process. Thus, the geometry of a multiple level rope can be analyzed considering each level as a single helix. The parametric representation of the centerline of each rope component (single helix) is given by

$$x(\phi) = a\cos(\phi) \tag{3.1a}$$

$$y(\phi) = a\sin(\phi): \qquad 0 \leq \phi \leq \frac{2\pi L}{p} \tag{3.1b}$$

$$z(\phi) = \frac{p\phi}{2\pi} \tag{3.1c}$$

where *a* is the helix radius, measured from the core axis of the level under consideration to the centerline of the rope component, ϕ is the swept angle, *p* is the pitch distance and *L* is the projected length of the rope component on the core axis. Based on the above parametric representation, the centerline of a rope component lies on the cylinder $x^2 + y^2 = a^2$ and winds around it in such a way that when ϕ increases by 2π, the *x* and *y* components return to their original value, while *z* increases by *p*, the pitch of the helix.

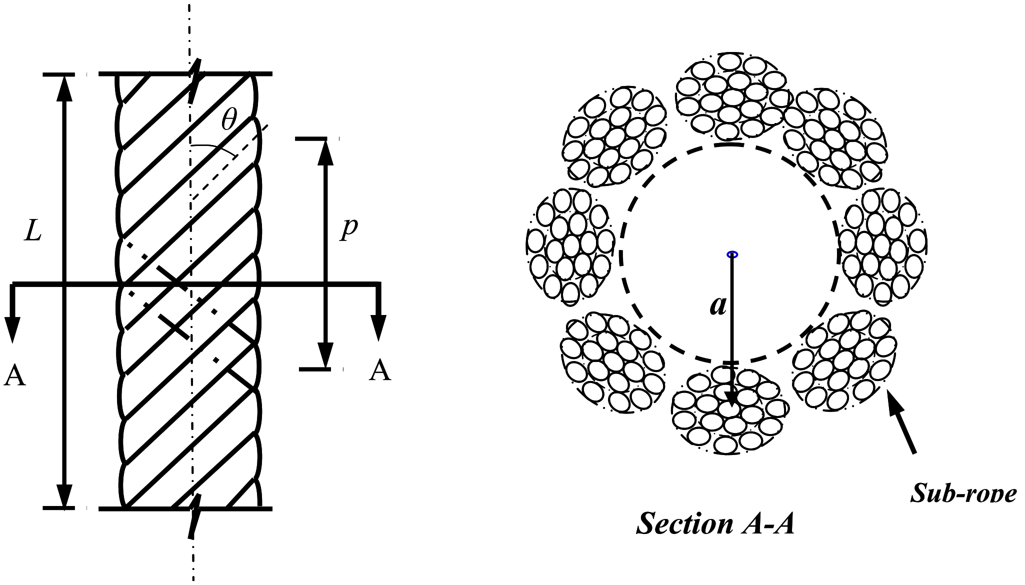

Fig. 3.4: Rope geometry

Based on Eqs. 3.1, three geometric parameters are needed to describe a rope component in a single helix configuration: helix radius (*a*), projected length of the rope component on the core axis (*L*) and pitch distance (*p*) as shown in Fig. 3.4. By definition, a circular helix curve makes a constant angle (helix angle) with a fixed line in space. This fixed line is the longitudinal axis of each component, and the helix angle (θ) is defined as the angle between the axis of the component and the axis of the core component (Fig 3.4). The helix angle (θ) can be computed using the following expression:

$$\tan(\theta) = \frac{2\pi a}{p} \tag{3.1d}$$

3.1.2.1 Curvature of a Rope

To analyze a rope element in space, it is convenient to use a local coordinate system at each point on its centroidal axis defined by the tangent ($\boldsymbol{x_1}$), normal ($\boldsymbol{x_2}$) and binormal ($\boldsymbol{x_3}$) vectors at that point (Fig. 3.5). This naming convention is referred to as the

Frenet frame at that point (Struik, 1988). The arc length of a helix curve in the space between two points is defined by the following expression:

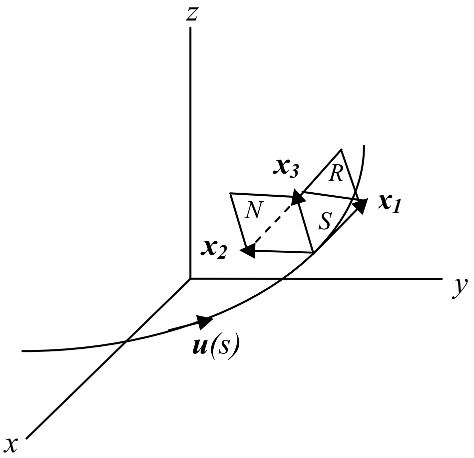

Fig. 3.5: Local coordinate system for a rope element

$$s(\phi) = \int_{\phi_0}^{\phi_1} \sqrt{\left(\frac{dx(\phi)}{d\phi}\right)^2 + \left(\frac{dy(\phi)}{d\phi}\right)^2 + \left(\frac{dz(\phi)}{d\phi}\right)^2} \tag{3.2}$$

where $x(\phi)$, $y(\phi)$ and $z(\phi)$ are defined from Eqs. (3.1a) through (3.1c). The solution of Eq. (3.2) yields the following expression for the arc length s of a helix curve in terms of the variable ϕ:

$$s(\phi) = \sqrt{a^2 + \left(\frac{p}{2\pi}\right)^2}\,\phi \tag{3.3}$$

where a and p were defined in Fig. 3.4. Thus, the arc length may be used as parameter in the parametric representation of the helix curve. Furthermore, ***u(s)*** satisfies the criteria defined above for use as an allowable parametric representation. It should be noted that the parameter s is often called the natural parameter (Kreyszig, 1991).

By definition, the unit tangent vector $\boldsymbol{x_1}(s)$ to the helix curve at the point $\boldsymbol{u(s)}$ is given by

$$\boldsymbol{x_1}(s) = \frac{d\boldsymbol{u}(s)}{ds} \tag{3.4}$$

All vectors at the point $\boldsymbol{u(s)}$ of the helix curve, which are orthogonal to the corresponding unit tangent vector, lie in a plane. This plane is called the normal plane (N) to the helix curve at $\boldsymbol{u(s)}$ (Fig. 3.5). An orthogonal vector to the unit tangent vector $\boldsymbol{x_1}(s)$ that measures the rate of change of the tangent vector along the curve is called the curvature vector and is given by $d\boldsymbol{x_1}(s)/ds$. The curvature vector is the intersection of the normal plane (N) of the helix curve and the osculating plane (S), which is the plane spanned by vectors $\boldsymbol{x_1}(s)$ and $d\boldsymbol{x_1}(s)/ds$ at the point under consideration (Struik, 1988). Thus, the unit principal normal vector $\boldsymbol{x_2}(s)$ to the helix curve at the point $\boldsymbol{u(s)}$ (Fig. 3.5) is given by

$$\boldsymbol{x_2}(s) = \frac{\dfrac{d\boldsymbol{x_1}(s)}{ds}}{\left|\dfrac{d\boldsymbol{x_1}(s)}{ds}\right|} \tag{3.5}$$

where |·| is the Eucledian norm or absolute value, defined for this particular case as a mapping |·|: $R^3 \rightarrow R$. A proportionality factor κ can be introduced to relate the curvature vector $d\boldsymbol{x_1}(s)/ds$ and the unit principal normal vector $\boldsymbol{x_2}(s)$ such that

$$\frac{d\boldsymbol{x_1}}{ds} = \kappa \boldsymbol{x_2}(s) \tag{3.6}$$

where κ is called the curvature of the curve at the point under consideration. Alternatively, if two tangent vectors $\boldsymbol{x}_1(s)$ and $\boldsymbol{x}_1(s) + \Delta\boldsymbol{x}_1(s + h)$ are compared, then $\boldsymbol{x}_1(s)$, $\Delta\boldsymbol{x}_1(s + h)$ and $\boldsymbol{x}_1(s) + \Delta\boldsymbol{x}_1(s + h)$ form an isosceles triangle with two sides equal to 1, enclosing the angle $\Delta\varphi$, the angle of contingency (Struik, 1988). If the absolute value of the vector $\Delta\boldsymbol{x}_1(s + h)$ is computed, $|\Delta\boldsymbol{x}_1(s + h)|$, and the result is linearized in terms of $\Delta\varphi$, it turns out that as $\Delta\varphi$ tends to zero, the following relation holds

$$\kappa = \left|\frac{d\boldsymbol{x}_1(s)}{ds}\right| = \left|\frac{d\varphi(s)}{ds}\right| \tag{3.7}$$

which is the usual definition of curvature κ in the case of a plane curve. For the case of a helix curve, the curvature κ is given by

$$\kappa = \frac{\phi^2 a}{L^2 + (\phi a)^2} \tag{3.8}$$

where L is the projected length of the rope component on the core axis, ϕ is the swept angle and a the helix radius.

3.1.2.2 Torsion of a Rope

As stated earlier, the intersection of the osculating plane (*S*) and the normal plane (*N*) is the unit principal normal vector $\boldsymbol{x}_2(s)$ (Fig. 3.5). All the vectors that lay in the osculating plane (*S*) can be spanned by the vectors $\boldsymbol{x}_1(s)$ and $\boldsymbol{x}_2$(s). The vector $\boldsymbol{x}_3(s)$, called the binormal vector (Fig. 3.5), can be obtained by the computing the cross product between vectors $\boldsymbol{x}_1(s)$ and $\boldsymbol{x}_2(s)$. Thus, by definition of the cross product, the vector $\boldsymbol{x}_3(s)$ is normal to the osculating plane (*S*) and also is the intersection of the normal plane (*N*) and the rectifying plane (*R*), which is plane spanned by the vectors $\boldsymbol{x}_1(s)$ and $\boldsymbol{x}_3(s)$ (Fig. 3.5). Due to the orthogonality of the vectors $\boldsymbol{x}_1(s)$, $\boldsymbol{x}_2(s)$ and $\boldsymbol{x}_3(s)$, they can be taken as a new frame of reference (Struik, 1988).

The rate of change of the vector defining the osculating plane (*S*) is given by d$\boldsymbol{x_3}(s)$/ds. Differentiating the relation $\boldsymbol{x_3}(s)\cdot\ \boldsymbol{x_1}(s) = 0$ with respect to s, using the expression given by Eq. (3.7) and considering the orthogonal property of the vectors $\boldsymbol{x_1}(s)$, $\boldsymbol{x_2}(s)$ and $\boldsymbol{x_3}(s)$, it can be shown that the vector d$\boldsymbol{x_3}(s)$/ds lies in the direction of the unit principal normal vector $\boldsymbol{x_2}(s)$. Thus, a proportionality factor ξ can be introduced to relate unit principal normal vector $\boldsymbol{x_2}(s)$ and the vector d$\boldsymbol{x_3}(s)$/ds such that

$$\frac{d\boldsymbol{x}_3(s)}{ds} = -\xi\boldsymbol{x}_2(s) \tag{3.9}$$

where ξ is called the torsion of the curve at the point under consideration. A scalar multiplication of Eq. (3.9) by $\boldsymbol{x_2}(s)$ yields the following expression for ξ

$$\xi = -\frac{d\boldsymbol{x}_3(s)}{ds}\boldsymbol{x}_2(s) \tag{3.10}$$

For the case of a helix curve, the torsion ξ is given by

$$\xi = \frac{\phi L}{L^2 + (\phi a)^2} \tag{3.11}$$

where L is the projected length of the rope component on the core axis, ϕ is the swept angle and a the helix radius.

3.1.2.3 Formulae of Frenet

The first derivates $d\boldsymbol{x_1}(s)/ds$, $d\boldsymbol{x_2}(s)/ds$ and $d\boldsymbol{x_3}(s)/ds$ of the unit vectors $\boldsymbol{x_1}(s)$, $\boldsymbol{x_2}(s)$ and $\boldsymbol{x_3}(s)$ can be taken as a linear combination of the vectors $\boldsymbol{x_1}(s)$, $\boldsymbol{x_2}(s)$ and $\boldsymbol{x_3}(s)$. The corresponding formulae are called the formulae of Frenet and have a kinematic interpretation when the frame of reference $\boldsymbol{x_1}(s)$-$\boldsymbol{x_2}(s)$-$\boldsymbol{x_3}(s)$ moves along a curve *C* (Kreyszig, 1991).

An expression for the vector $d\boldsymbol{x_2}(s)/ds$ in terms of the unit vectors $\boldsymbol{x_1}(s)$, $\boldsymbol{x_2}(s)$ and $\boldsymbol{x_3}(s)$ can be obtained by differentiating the identity $\boldsymbol{x_2}(s)\cdot \boldsymbol{x_2}(s) = 1$, which is the square of the absolute value of the vector $\boldsymbol{x_2}(s)$. Having done the differentiation, it turns out that if the vector $d\boldsymbol{x_2}(s)/ds$ is not the null vector, it is orthogonal to $\boldsymbol{x_2}(s)$ and consequently can be spanned by a linear combination of the unit vectors $\boldsymbol{x_1}(s)$ and $\boldsymbol{x_3}(s)$. Using the fact that the vectors $\boldsymbol{x_1}(s)$, $\boldsymbol{x_2}(s)$ and $\boldsymbol{x_3}(s)$ are orthogonal, and by differentiating with respect to s the expressions $\boldsymbol{x_2}(s)\cdot \boldsymbol{x_1}(s) = 0$ and $\boldsymbol{x_2}(s)\cdot \boldsymbol{x_3}(s) = 0$, the vector $d\boldsymbol{x_2}(s)/ds$ can be taken as

$$\frac{d\boldsymbol{x}_2(s)}{ds} = -\kappa\boldsymbol{x}_1(s) + \xi\boldsymbol{x}_3(s) \tag{3.12}$$

Eq. (3.12), along with Eqs. (3.6) and (3.9), are the formulae of Frenet, which in matrix notation has the following form:

$$\begin{pmatrix} \dfrac{d\boldsymbol{x}_1(s)}{ds} \\ \dfrac{d\boldsymbol{x}_2(s)}{ds} \\ \dfrac{d\boldsymbol{x}_3(s)}{ds} \end{pmatrix} = \begin{bmatrix} 0 & \kappa & 0 \\ -\kappa & 0 & \xi \\ 0 & -\xi & 0 \end{bmatrix} \begin{pmatrix} \boldsymbol{x}_1(s) \\ \boldsymbol{x}_2(s) \\ \boldsymbol{x}_3(s) \end{pmatrix} \tag{3.13}$$

The kinematic interpretation of the formulae of Frenet is based on Fig. 3.6. Consider that the frame of reference $\boldsymbol{x_1}(s)$-$\boldsymbol{x_2}(s)$-$\boldsymbol{x_3}(s)$ moves along a curve C with a constant velocity of a unit magnitude. Vectors $\boldsymbol{x_1}(s)$, $\boldsymbol{x_2}(s)$ and $\boldsymbol{x_3}(s)$ span a three-dimensional space, each with a constant length equal to 1. Thus, these vectors can be thought of as being inscribed on a rigid body B (Fig. 3.6), that performs the same motion as the frame of reference. Therefore, the kinematic interpretation of formulae of Frenet may be considered as a problem of rigid body kinematics. The study of the problem presented in Fig. 3.6, is summarized in the following theorem (Kreyszig, 1991): "The rotation vector $\boldsymbol{d}$ of the trihedron (frame of reference) of a curve C: $\boldsymbol{u}$(s) of class $r \geq 3$ ($\boldsymbol{u}(s)$ posseses continuous derivatives up to the order r, inclusive) with non-vanishing curvature, when a point moves along C with constant velocity 1, is given by the expression

$$\boldsymbol{d} = \xi \boldsymbol{x}_1 + \kappa \boldsymbol{x}_3 \tag{3.14}$$

where vector ***d*** is also called the vector of Darboux, whose absolute value $|\boldsymbol{d}|$ is the angular velocity of rotation".

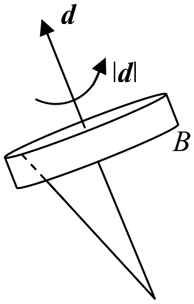

Fig. 3.6: Kinematic of a rigid body *B*

Based on Eq. (3.14), the torsion ξ and the curvature κ of a curve C are the projections of the angular velocity $|\boldsymbol{d}|$ of the trihedron (frame of reference) on the unit tangent vector $\boldsymbol{x}_1(s)$ and unit binormal vector $\boldsymbol{x}_3(s)$, respectively. If the curve C is a helix curve, both kinematic parameters, the torsion ξ and the curvature κ, are constant along the curve (Eqs. (3.8) and (3.11)), and the ratio between these two parameters is given by

$$\frac{\kappa}{\xi} = \tan(\theta) \tag{3.15}$$

where θ is the helix angle (Fig. 3.4).

3.1.2.4 Axial Deformation of Rope Elements

The axial strain of a rope element can be obtained using the fact that, as previously mentioned, the centerline of a rope element lies on the cylinder $x^2 + y^2 = a^2$ and winds around it in such a way that when ϕ increases by 2π, the x and y components return to their original value, while z increases by p, the pitch of the helix (Fig. 3.7). Based on trigonometric relations and the engineering strain definition, the axial strain of a rope element is given by (Costello, 1990)

$$\varepsilon_{er} = \sqrt{\frac{L^2 + (\phi a)^2}{L_0^2 + (\phi_0 a_0)^2}} - 1 \tag{3.16}$$

where L_0 is the projected length of the rope element on the core axis in the reference configuration, L is the projected length of the rope element on the core axis in the current (i.e., deformed) configuration, ϕ is the swept angle and a the helix radius.

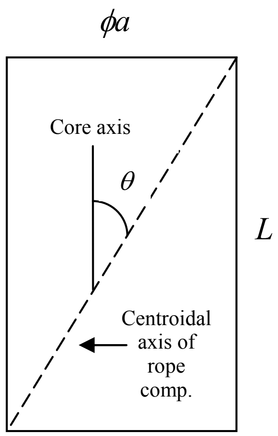

Fig. 3.7: Developed view of rope component helix

3.2 CONSTITUTIVE MODELS

The material behavior for synthetic-fiber ropes is assumed to be known at the lowest hierarchical level of a rope element and behaves elastically. The stress-strain relationship could be linear or nonlinear depending on the type of fiber used to construct the rope under investigation. Time-dependent behavior of the material fibers is not included in the current model. Any variability in fiber properties that could affect rope strength is also neglected. Due to the lack of available test data, and in order to be consistent with previous researchers (Liu, 1989, 1995; Leech, 1990; Fernandes et al., 1999; Flory, 2001), both normal and shear stresses are expressed as polynomial functions of the normal and shear strain, respectively, up to the fifth degree, having the following form (Rungamornrat et al., 2002):

$$\frac{\sigma}{\sigma_b} = a_1\left(\frac{\varepsilon}{\varepsilon_b}\right) + a_2\left(\frac{\varepsilon}{\varepsilon_b}\right)^2 + a_3\left(\frac{\varepsilon}{\varepsilon_b}\right)^3 + a_4\left(\frac{\varepsilon}{\varepsilon_b}\right)^4 + a_5\left(\frac{\varepsilon}{\varepsilon_b}\right)^5 \tag{3.17a}$$

$$\frac{\tau}{\tau_b} = b_1\left(\frac{\gamma}{\gamma_b}\right) + b_2\left(\frac{\gamma}{\gamma_b}\right)^2 + b_3\left(\frac{\gamma}{\gamma_b}\right)^3 + b_4\left(\frac{\gamma}{\gamma_b}\right)^4 + b_5\left(\frac{\gamma}{\gamma_b}\right)^5 \tag{3.17b}$$

where ε_b and γ_b are the normal and shear strain, respectively, at which an element reaches its maximum normal (σ_b) and shear (τ_b) stress under monotonic loading. The coefficients a_i and b_i are constitutive parameters and are chosen to provide a best fit to measured data of rope components that belong to the lowest hierarchical level of a rope.

3.3 CROSS-SECTION MODELING

In order to model the cross-section of a rope element, two types of arrangements of the components are considered: packing and wedging geometry (Fig. 3.8), which represent the extreme cases of transverse deformation of the cross-section for real ropes (Leech, 2002).

3.3.1 Packing geometry

It is assumed that all components of a rope element are initially straight and circular in cross-section and transversely stiff, and a twist of a specified number of turns is to the central component. Contact between components in the same level is assumed to be only in the radial direction, and slip at those points is prevented due to the assumptions made regarding the kinematics of deformation (Leech, 2002).

3.3.2 Wedging Geometry

In the wedging geometry, the components in the same level are allowed to deform transversely and change their shape into a wedge or truncated wedge, which is the shape that would develop for deformable components. It is assumed that there is circumferential contact pressure and friction acting along the length of components due to axial slip between contiguous components (Leech, 2002). Radial contact, however, is assumed to be negligible in comparison to the circumferential contact and is ignored for computational purposes.

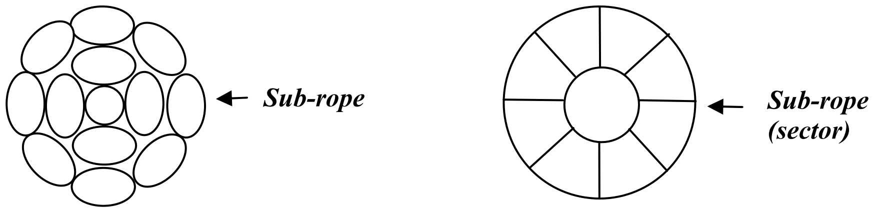

Packing Geometry ***Wedging Geometry***

Fig. 3.8: Type of rope constructions

3.3.3 Cross-Section Update

In general, the total deformation of a rope element is attributable to the following three effects: rope elongation, rope rotation, and a radial deformation of the rope element. The first two effects were already analyzed in Section 3.1. In this sub-section, the following three models are used to compute the radius *r* of a rope element in its deformed configuration: constant cross-section, constant volume and Poisson effect.

3.3.3.1 Constant Cross-Section Model

In this model, it is assumed that the cross-section of a rope element remains constant through its entire loading history. Thus, the value of *r* is given by

$$r = r_0 \tag{3.18a}$$

3.3.3.2 Constant Volume Model

In this model, it is assumed that the material of the rope element is incompressible, which means that its volume is preserved throughout its entire loading history. By equating the initial and current volume, the value of *r* in the deformed configuration is given by

$$r = \frac{r_0}{\sqrt{1+\varepsilon_{er}}} \tag{3.18b}$$

3.3.3.3 Poisson Effect Model

In this model, the transverse strain of a rope element is related to its axial strain by Poisson's ratio. Thus, the value of *r* is given by

$$r = r_0(1-\nu\varepsilon_{er}) \tag{3.18c}$$

where v is the Poisson's ratio of the material rope element, ε_{er} is given by Eq. (3.16) and r_0 is the radius of the rope element in its initial configuration.

3.4 EQUILIBRIUM EQUATIONS AND FRICTION MODELS

The following subsections describe the governing equilibrium equations for a element within a rope. First, general equations are provided that account for bending, twisting, axial, and shear deformations. Next, these expressions are simplified based on assumptions of the stress state in an individual rope element. Finally, friction models that account for the interaction of rope components within a given rope cross-section are described.

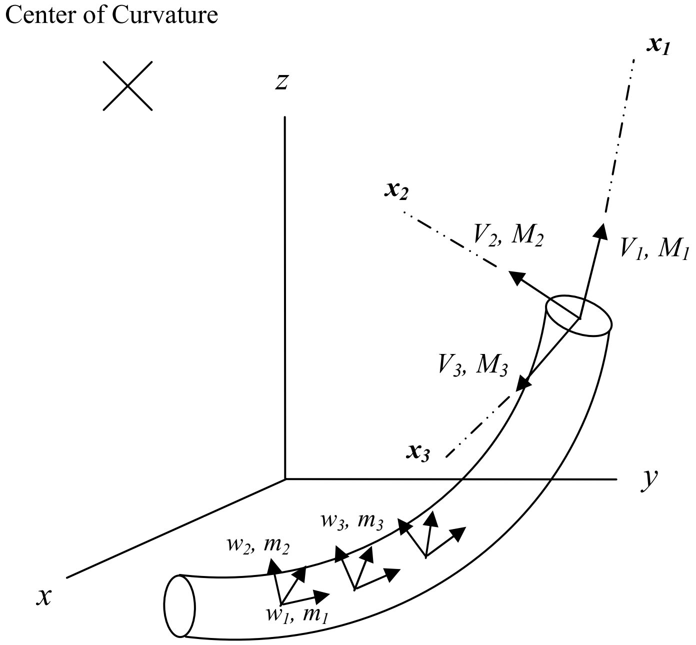

Fig. 3.9 Loads acting on a line circular helix element

3.4.1 Differential Equations of Equilibrium

In order to compute the stresses acting in a rope, each element that belongs to the lowest hierarchical level of a rope component is treated as a helical rod. As explained in Section 2.2.1.2, a helical rod has axial, shear, flexural and torsional stiffness. The tractions associated with a deformed configuration of an element are statically equivalent to three mutually orthogonal forces acting at the centroid of the cross-section along with couples around each axis (Fig. 3.9), where V_i are the forces in the i direction; M_i are the moments about the i axis; and w_i and m_i are the contact forces and distributed moment per unit length, respectively, in the i direction. Thus, equilibrium equations for an element are established along its centerline (defining a line (thin) element) in space, assuming incrementally small deformations.

Due to the assumptions made concerning the construction of a rope, axial elongation leads to the development of both tensile and torsional forces. Because of the geometric restrictions made on the kinematics of deformation, the state of stress and strain associated with axial elongation is constant along the centerline of each helical rope component. Therefore, stresses and loads in rope components can be described by the stresses and loads on a single transverse cross-section of a helical rope. The general differential form of the equilibrium equations of a line element is given considering an orthogonal local coordinate system $\boldsymbol{x}_1$- $\boldsymbol{x}_2$- $\boldsymbol{x}_3$ (Fig. 3.8), where $\boldsymbol{x}_1$ is the tangent vector, $\boldsymbol{x}_2$ is the normal vector and $\boldsymbol{x}_3$ is the binormal vector that form a Frenet frame (Section 3.1.2.1).

In order to obtain the equilibrium equations for a line element in space, Fig. (3.10) shows two planar views of length ds of a line element along with the forces (no moments) acting on it. Fig. (3.10a) shows a view looking down the $\boldsymbol{x}_3$ axis, whereas Fig. (3.10b) shows a similar view looking down the $\boldsymbol{x}_2$ axis. The direction cosines of the forces V_1+dV_1, $V_2+ dV_2$ and V_3+dV_3 with the axes $\boldsymbol{x}_1$, $\boldsymbol{x}_2$ and $\boldsymbol{x}_3$ are linearized using a Maclaurin series expansion. Thus, $\cos(\alpha_{k'l}) \approx 1$ and $\sin(\alpha_{k'l}) \approx \alpha_{k'l}$ with $\alpha_{k'l}$ (k', l = 1, 2, 3) the angle of rotation of the vectors $\boldsymbol{x'}_k$ relative to the vectors $\boldsymbol{x}_l$ (Fig. 3.10). Based on the definitions given for the curvature (Eq. 3.7) and torsion (Eq. 3.10) of a curve, the required direction cosines are listed in Table 3.1.

Table 3.1 Direction Cosines

Direction cosine	V_1+dV_1	V_2+dV_2	V_3+dV_3
$\boldsymbol{x}_1$	$\cos(\alpha_{1'1}) \approx 1$	$-\sin(\alpha_{2'1}) \approx -\kappa_3 ds$	$-\sin(\alpha_{3'1}) \approx -\kappa_2 ds$
$\boldsymbol{x}_2$	$\sin(\alpha_{1'2}) \approx \kappa_3 ds$	$\cos(\alpha_{2'2}) \approx 1$	$\sin(\alpha_{3'2}) \approx -\xi ds$
$\boldsymbol{x}_3$	$\sin(\alpha_{1'3}) \approx \kappa_2 ds$	$\sin(\alpha_{2'3}) \approx \xi ds$	$\cos(\alpha_{3'3}) \approx 1$

where κ_2 and κ_3 are the curvatures of the line element in the rectifying and osculating plane respectively, and ξ is the torsion of the line element. Based on Fig. 3.10, a summation of forces in the $\boldsymbol{x_1}$ direction, neglecting second and higher order terms, yields

$$dV_1 + w_1 ds - V_2\kappa_3 ds + V_3\kappa_2 ds = 0 \tag{3.19}$$

which becomes, upon normalizing by *ds*,

$$\frac{dV_1}{ds} + w_1 - V_2\kappa_3 + V_3\kappa_2 = 0 \tag{3.20}$$

Similarly, a summation of forces in the $\boldsymbol{x_2}$ and $\boldsymbol{x_3}$ directions yield

$$\frac{dV_2}{ds} + w_2 + V_1\kappa_3 - V_3\xi = 0 \tag{3.21}$$

and

$$\frac{dV_3}{ds} + w_3 - V_1\kappa_2 + V_2\xi = 0 \tag{3.22}$$

Following the procedure used to obtain the equilibrium equations for the forces, Fig. 3.11 shows the same line element of length *ds* loaded just with the moments that act on the element. The moments M_1+dM_1, M_2+dM_2 and M_3+dM_3 make the same angles $\alpha_{k'l}$ (k', l = 1, 2, 3) with respect to the axes $\boldsymbol{x_1}$, $\boldsymbol{x_2}$ and $\boldsymbol{x_3}$ as do the forces V_1+dV_1, V_2+dV_2 and V_3+dV_3. Thus, the direction cosines given in Table 3.1 can be used to establish the three moment equilibrium equations. Neglecting second order effects, a summation of moments about the $\boldsymbol{x_1}$ axis yields

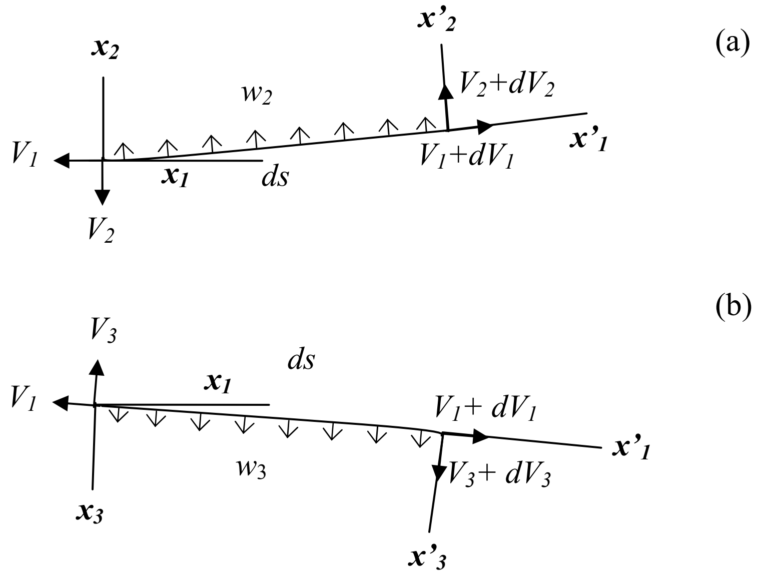

Fig. 3.10: Centerline of a line element looking down (no moments) (a) x_3 axis and (b) x_2 axis

$$\frac{dM_1}{ds} + m_1 - M_2\kappa_3 + M_3\kappa_2 = 0 \tag{3.23}$$

Similarly, a summation of moments about the x_2 and x_3 axes yield

$$\frac{dM_2}{ds} + m_2 + M_1\kappa_3 - M_3\xi - V_3 = 0 \tag{3.24}$$

and

$$\frac{dM_3}{ds} + m_3 - M_1\kappa_2 + M_2\xi + V_2 = 0 \tag{3.25}$$

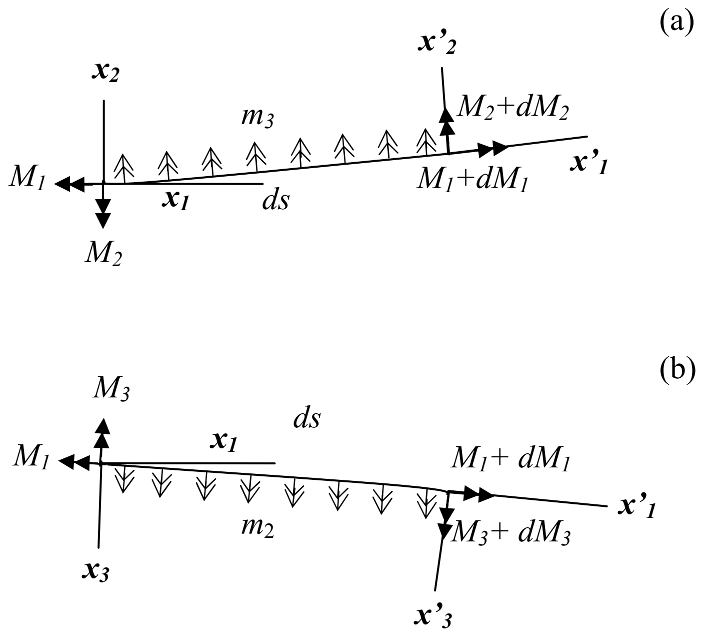

Fig. 3.11. Centerline of a line element looking down (no forces): (a) x_3 axis and (b) x_2 axis

Equations (3.20) through (3.25) are the six differential equations of equilibrium for the line element loaded as shown in Fig. 3.9 (Love, 1944).

3.4.2 Reduced Equilibrium Equations

The set of six differential equations of equilibrium previously described can be simplified using the assumptions made to describe the response of a rope element (Costello, 1990):

- A rope element develops constant stresses along its length, which means that any variation in a stress resultant with respect to the arc length s vanishes ($d()/ds = 0$).
- Based on Eq. (3.14), the curvature κ of a rope element is referred to the binormal axis $\boldsymbol{x_3}$, which means that $\kappa_3 = \kappa$ and $\kappa_2 = 0$.

- A rope element is not subjected to bending moments per unit length, that is, $m_3 = 0$ and $m_2 = 0$.

By letting $T_e = V_1$, $V = V_3$, $M_{te} = M_1$, $M_{be} = M_3$ and $X = w_2$, in which T_e is the tension force, V is the shear force in the binormal direction, M_{te} is the twisting moment, M_{be} is the bending moment about the binormal direction and X is the contact force per unit length in the normal direction, the equilibrium equations of a rope component reduce to

$$-V\xi + T_e\kappa + X = 0 \tag{3.26}$$

$$-M_{be}\xi + M_{te}\kappa - V = 0 \tag{3.27}$$

$$m_1 = V_2 = w_1 = w_3 = 0 \tag{3.28}$$

The contribution of the element stress resultants (axial force, shear force, twisting and bending moments) to the next higher level resultants can be determined as follows:

$$T_s = T_e \cos\theta + V \sin\theta \tag{3.29}$$

$$M_{bs} = M_{be} \cos\theta - M_{te} \sin\theta \tag{3.30}$$

$$M_{ts} = M_{te} \cos\theta + M_{be} \sin\theta + (T_e \sin\theta - V \cos\theta)a \tag{3.31}$$

where T_s, M_{bs} and M_{ts} are the axial force, bending and twisting moments on the next higher level, respectively, and a and θ are the helix radius and the helix angle of the rope element respectively, defined at the level of the rope element considered. It should be noted that if the arrangement of the elements in each layer is symmetric, the value of M_{bs} must vanish. However, there may be some situations in which the value of M_{bs} does not vanish, and an unbalanced bending moment can act on a rope. Some possible situations that can lead to an unbalanced bending moment include variation in material properties in rope elements, variation in cross-sectional geometry in rope elements, variation in the degree of damage experienced by rope elements, etc.

3.4.3 Force and Moment Resultants in a Rope Element

Once the deformed configuration of a rope element is known, and using the constitutive models proposed in Section 3.2, the internal stress resultants acting on the cross-section of a rope element can be computed. By enforcing the equilibrium conditions on the cross-section of a rope element between the internal and external load actions, the following well known expressions are obtained:

$$T_e = \int_A \sigma(\varepsilon) dA \tag{3.32}$$

$$M_{be} = \int_A \zeta \sigma(\varepsilon) dA \tag{3.33}$$

$$M_{te} = \int_A \rho \tau(\gamma) dA \tag{3.34}$$

where T_e is the tension force, M_{te} is the twisting moment, M_{be} is the bending moment about the binormal direction, and $\sigma(\varepsilon)$ and $\tau(\gamma)$ are the normal and shear stresses given by Eqs. (3.17a) and (3.17b), respectively. The distances ζ and ρ are measured from the centroid of a rope element and belong to the interval [-*r*, *r*], where *r* is the radius of the cross-section of the rope element as shown in Fig. 3.12.

It is assumed that both the normal strain due to bending and shear strain due to torsion vary linearly through the cross-section of a rope element, thus the following expressions hold:

$$\varepsilon = \varepsilon_{er} + \zeta(\kappa - \kappa_0) \tag{3.35}$$

$$\gamma = \rho(\xi - \xi_0) \tag{3.36}$$

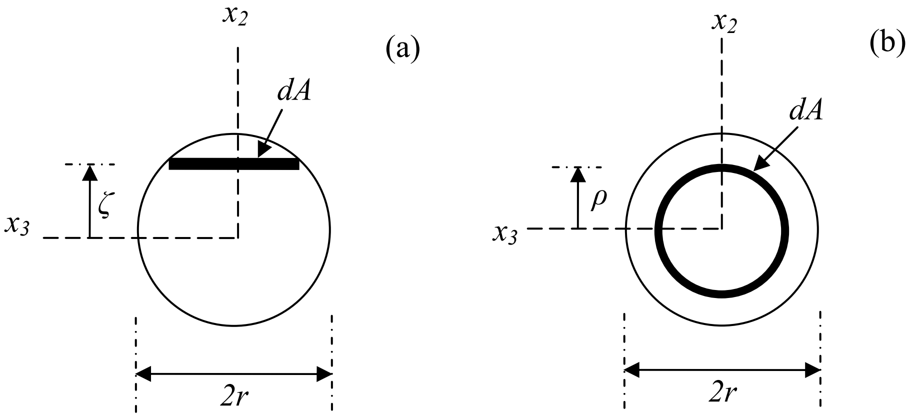

Fig. 3.12 (a) Cross-section for bending moment, (b) Cross-section for torsion

where ε_{er} is the axial strain of a rope element due to an extension and/or rotation of the rope given by (Eq. 3.16) and κ_0 and ξ_0 are the curvature and torsion in the initial configuration of the rope element, respectively. Based on Eqs. (3.35) and (3.36), Eqs. (3.32) through (3.34) can be solved using a numerical integration scheme (e.g., Gaussian Quadrature), and the resulting values of T_e, M_{te} and M_{be} are used with Eqs. (3.26) and (3.27) to obtain the values of the shear force V and contact force per unit length w that act on a rope element.

3.4.4 Friction Model

In any fiber rope structure where there is no bonding between rope elements, the results of any deformation must result in a slip of contiguous rope elements due to the assumption of geometry preservation and finite dimensions of the rope elements' cross-sections. Due to the helical geometry of the rope elements, the applied external action on the rope (loads or displacements) results in bearing pressures at the contact regions. The actual slip magnitude in the contact regions is a fraction of the rope elements' diameter, whereas bearing forces are functions of the rope geometry. Due to the relative slip and the presence of bearing pressures between contiguous rope elements, frictional forces can be developed. The slip at contact regions and the bearing pressure combine to give the work done by friction in opposing rope deformation. Although the magnitude of the contribution of frictional forces to rope force resultants is small, the number of slipping location and the repeated action of loading and unloading could have significant effects on the long-term performance of a rope. Thus, the energy loss through the accompanying friction hysteresis would be substantial and become an important factor in studying the deterioration of ropes during their loading history. Several modes of slip can be identified during rope deformation (Leech, 2002). In this study, however, only the two most important modes of slip identified by Leech (2002) are considered: slip due to stretch and slip due to change of the helix angle.

In order to estimate the magnitude of frictional forces, a simple model has been established, based on the classical slip-stick model, where frictional forces act in the direction opposite the relative slip direction between contiguous rope elements (Leech, 2002). The frictional force f is given in terms of the normal contact force, p_{nc}, as

$$f = f_a + \mu(p_{nc})^b \tag{3.37}$$

where f_a and b are friction parameters and μ is the coefficient of friction of the rope material. Based on the assumptions made to model the cross-sectional behavior of rope elements (Section 3.3), relative slip between elements vanishes for the packing geometry configuration because the contact region is assumed to be only in the radial direction. Consequently, frictional forces do not arise between rope elements. For the case of the wedging geometry configuration, the contact region is assumed to be in the circumferential direction and relative slip between contiguous rope elements is not prevented. Thus, the contact force, p_{nc}, normal to the contact region, is given by

$$p_{nc} = \frac{X}{2\cos\theta\sin\psi} \tag{3.38}$$

where X is the radial contact force obtained from Eq. (3.26), ψ is one half of the subtended angle of the wedge and is equal to π/n, with n the number of rope elements in the layer under study, and θ is the helix angle given by Eq. (3.1d). The contribution of the frictional forces to the force resultants of the rope can be obtained by adding the projected components of the frictional forces to Eqs. (3.29)–(3.31) as shown in Fig. (3.13).

The vertical (V_f) and horizontal (H_f) contribution of the frictional force f to the rope force resultants are given by

$$V_f = 2fD\sin(\theta) \tag{3.39}$$

and

$$H_f = fD\frac{2\cos^2(\theta)-1}{\cos(\theta)} \tag{3.40}$$

where $D = 2a\sin(\psi)$, a is the helix radius of the element and θ is the helix angle of the element.

3.5 DAMAGE MODEL

The following subsections describe the proposed damage model to account for the deterioration of rope element properties as a function of the loading history. First, a background of the possible factors that can cause damage of synthetic ropes is provided. Next, the proposed evolution law that describes the damage accumulation in rope elements throughout their loading history is presented. Finally, invoking principles of continuum damage mechanics, the effects of damage accumulation on rope strength and stiffness are described.

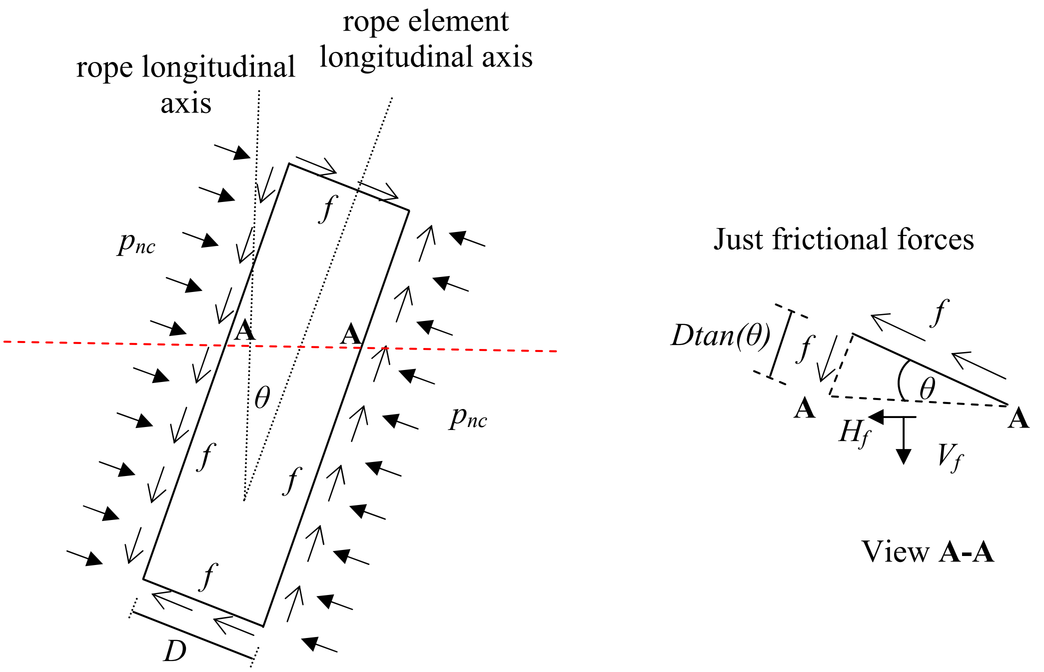

Fig. 3.13: Effect of frictional forces on rope force resultants

3.5.1 General Background

The deterioration of rope properties during loading has been observed in previous investigations (Liu, 1989, 1995; Lo et al., 1999; Banfield and Casey, 1998; Karayaka et al., 1999; Mandell, 1987). The failure of a rope element is a complicated process that could depend on a variety of factors such as strain range, abrasion, number of loading cycles, installation procedures, environmental interaction, etc. In the current model, the following three processes are considered: strain range, abrasion (due to frictional forces) and number of load cycles at a given stress range.

The damage of materials takes place when atomic bonds break at the microestructural level. The phenomenon of damage represents surface discontinuities in the form of microcracks or volume discontinuities in the form of cavities. In this study, the hypothesis of isotropic damage is assumed, which implies that the microcracks and cavities (defects) are uniformly distributed in all directions. Thus, the damaged state is completely characterized by the scalar damage index parameter *D*. This parameter evolves during the response history and modifies rope behavior when any of the rope elements experience damage (Rungamornrat et al., 2002; Beltran et al., 2003).

The degradation of the mechanical properties of a system is, in general, an irreversible process. As the damage index parameter captures the damage accumulation of the system, it should be represented by a continuous and monotonically increasing function with values that can vary from 0 to 1. A value of 0 corresponds to the undamaged state of a component, and $D=1$ indicates its complete rupture. In this particular study, the evolution rule of damage *D* is obtained experimentally, which includes curve fitting and eventually statistical analysis.

3.5.2 Damage Evolution Rule

As previously mentioned, Rungamornrat et al. (2002) proposed a damage evolution model in which the damage index parameter depends on the strain range, abrasion (due to frictional forces) and number of load cycles at a given stress range. Based on this model, the evolution rule of the damage index parameter *D* is given by

$$D = D_I + \alpha_1 \left(\frac{\varepsilon_m - \varepsilon_t}{\varepsilon_b} \right)^{\beta_1} + \alpha_2 \left(\frac{W_{fa}}{W_{fe}} \right)^{\beta_2} + \alpha_3 \left(\sum_i \frac{1}{N_i} \right)^{\beta_3} \tag{3.41}$$

The first term in the above equation represents the initial damage D_I that an element could have before being loaded. The second term relates to the maximum strain (ε_m) that an element experiences over its entire loading history. The term ε_t represents the threshold strain that must be exceeded before damage occurs, and ε_b is the strain at which an element reaches its maximum stress under monotonic loading. The third term is introduced to account for the effects of abrasion due to frictional forces induced from the slip between elements during loading. The accumulated work done due to friction (W_{fa}) is utilized to measure the degree of abrasion. The toughness of an element under monotonic loading (W_{fe}) is used to normalize W_{fa}. Using a linear approximation between two consecutive load steps, the value of (W_{fa}) for the k^{th} load step is given by

$$W_{fa}{}^{k} = W_{fa}{}^{k-1} + \frac{1}{2}\left[f^{k-1} + f^{k}\right]\Delta slip^{k} \tag{3.42}$$

where ($W_{fa}{}^{k-1}$) is the accumulated work done by frictional forces up to the $(k\text{-}1)^{th}$ load step, f^{k-1} and f^{k} are the frictional forces in the $(k\text{-}1)^{th}$ and k^{th} load step respectively, and $\Delta slip^{k}$ is the relative slip between two contiguous elements at the k^{th} load step given by

$$\Delta slip^{k} = \frac{l^{k}}{l^{k-1}} 2a^{k-1}\sin(\psi)\sin(\theta^{k-1}) - 2a^{k}\sin(\psi)\sin(\theta^{k}) \tag{3.43}$$

where $l^{k\text{-}1}$ and l^{k}, $a^{k\text{-}1}$ and a^{k} and $\theta^{k\text{-}1}$ and θ^{k} are the length, helix radius and helix angle of the rope element in the $(k\text{-}1)^{th}$ and k^{th} load step, respectively.

The toughness of an element (W_{fe}) is defined as the required work needed to break the element in pure tension. Thus, the value of (W_{fe}) is given by

$$W_{fe} = A_0 l_0 \sigma_b \varepsilon_b \left[\sum_{i=1}^{5} \frac{a_i}{i+1}\right] \tag{3.44}$$

where A_0, l_0 are the initial area and initial length of the element under consideration, σ_b and ε_b are the normal stress and axial strain, respectively, at the onset of element failure, and a_i are the constitutive parameters of the constitutive model for normal stress (Eq. 3.17a).

The fourth term corresponds to the effect of stress range experienced by an element in the entire loading history and is used to account for fatigue effects under cyclic loads. The parameters N_i represent the minimum number of cycles necessary to break the element under the stress range of the i^{th} cycle. The relation between N_i and the stress range $\Delta\sigma_i$ in the proposed damage rule is given by

$$\Delta\sigma_i = \sigma_0 e^{cN_i^{-k}} \tag{3.45}$$

where c and k are model constants, and σ_0 is the endurance limit of the element. The coefficients α_k and β_k are damage parameters and are selected based on experimental data.

3.5.3 Basic Concept of Continuum Damage Mechanics

Synthetic-fibers are produced from polymers. Thus, they are made of molecules tied together in long repeating chains. Damage in polymers can be defined as the existence of distributed broken bonds between long chains of molecules, whereas the process of breaking the bonds between molecules that causes progressive material degradation through strength and stiffness reduction is called damage evolution (Chaboche, 1988; Lemaitre and Chaboche, 1990). Among the various definitions of the damage variable D is the ratio of the damaged area to the total (undamaged or virgin) area at a local material point (Kachanov, 1986). Based on this definition, the effective stress (σ_e) that the damaged medium experiences is defined as

$$\sigma_e = \frac{\sigma}{1-D} \tag{3.46}$$

where σ is the actual or nominal stress.

An expression for D can be found relating the undamaged and damaged medium. In this particular study, the principle of strain equivalence is used. This principle states that the deformation behavior of a material is only affected by damage in the form of the effective stress. Lemaitre and Chaboche, (1990) define this principle such that "any deformation behavior, whether uniaxial or multiaxial, of a damaged material is represented by the constitutive laws of the virgin material in which the nominal stress is replaced by the effective stress." A schematic representation of the principle of strain equivalence is presented in Fig. 3.14.

Consider the constitutive response for the virtual and damaged materials as shown in Fig. 3.14. Based on the previous assumptions, it is assumed that the following relations hold:

$$\sigma_e = f(\varepsilon, \varepsilon^2, ...) \tag{3.47a}$$

$$\sigma = g(\varepsilon, \varepsilon^2, ...) \tag{3.47b}$$

If for each strain ε the difference between the above expressions is computed (based on the principle of strain equivalence), and the definition of σ_e given by Eq. (3.46) is applied, the following expression relating the constitutive functions in terms of the damage index D is obtained:

$$g(\varepsilon, \varepsilon^2, ...) = (1 - D) f(\varepsilon, \varepsilon^2, ...) \tag{3.48a}$$

or

$$D = 1 - \frac{g(\varepsilon, \varepsilon^2, ...)}{f(\varepsilon, \varepsilon^2, ...)} \tag{3.48b}$$

The expression given by Eq. (3.48a) is used to obtain the constitutive equations for a damaged system once the evolution of D is known, where $f(\varepsilon, \varepsilon^2, ...)$ can be either the normal stress σ or shear stress τ given by Eqs. (3.17a) and (3.17b), respectively. Similarly, $g(\varepsilon, \varepsilon^2, ...)$ can be either the normal stress σ_d or the shear stress τ_d of the damaged system (Rungamornrat et al., 2002). An equivalent expression for Eq. (3.48b), based on Eqs. (3.47a) and (3.47b), is given by

$$D = 1 - \frac{\sigma}{\sigma_e} \tag{3.48c}$$

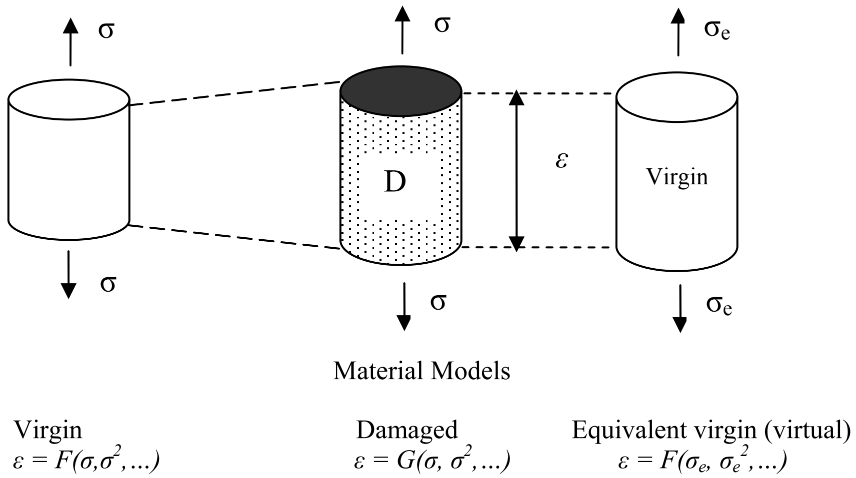

Fig. 3.14: Principle of strain equivalence (Lemaitre and Chaboche,1990)

Based on Eq. (3.48c), the definition of secant modulus $E_s = \sigma(\varepsilon)/\varepsilon,$ and the principle of strain equivalence previously explained, Eq. (3.48c) can be written as

$$D = 1 - \frac{E_{sd}(\varepsilon)}{E_{sv}(\varepsilon)} \tag{3.48d}$$

where $E_{sd}(\varepsilon)$ and $E_{sv}(\varepsilon)$ are the secant moduli of the damaged and virgin system, respectively, for a particular value of the axial strain ε.

3.6 SUMMARY

In this chapter, the foundations of a proposed mathematical model to predict the behavior of synthetic-fiber ropes under a variety of loads conditions have been presented. This model is an extension of the discrete helical rod model to study steel wire ropes and the model developed by Leech (2002) to analyze synthetic-fiber ropes. The kinematics of a rope, constitutive models, cross-section modeling, equilibrium equations and friction models described in this chapter are based on concepts from the two models previously mentioned. The major contribution that the proposed mathematical model addresses is the inclusion of a damage index to account for the effects of strength and stiffness degradation of rope elements. The calibration of the proposed damage model based on available experimental data is described in the next chapter. This model suggests that near the failure region, a strain concentration develops in the rope, reducing the overall rope capacity more significantly than the case in which this effect is ignored.

CHAPTER 4

Damage Model Calibration

4.1 OVERVIEW

The current study is focused on ropes loaded monotonically and subjected to a prescribed strain history. Under the assumption that frictional forces play a small role in affecting the breaking load of a rope under monotonic loading, and using the damage model evolution described in Section 3.5.2, deterioration of the mechanical properties of a rope is assumed to depend solely on the strain range of the response. According to this model (Eq. (3.41)), the contribution of the strain range to the evolution of the damage index *D* is given by

$$D = D_I + \alpha_1 \left(\frac{\varepsilon_m - \varepsilon_t}{\varepsilon_b} \right)^{\beta_1} \tag{4.1}$$

where the internal variable ε_m and the damage parameters D_I, ε_t, ε_b, α_1, β_1 are described in Section 3.5.2.

To calibrate the damage index evolution *D* given by Eq. (4.1), experimental data reported by Li et al. (2002) are used. In Fig. 4.1, the behavior of a one-level, two-layer rope loaded monotonically, along with its geometrical properties, is presented. In this rope construction, the strands do not contain their own core with components wound around it. As such, it is defined as having just one level. The strands are laid around the rope core giving rise to two layers (including the core). In this figure, two different curves are presented — simulation of rope response without any source of damage (considering a Poisson's ratio v equal to 0.25 (Li et al., 2002)), and experimentally measured data. The response of the rope without the effects of damage was computed using the governing equations presented in Chapter 3. The simulation of the rope response provides an upper bound for the experimental curve along the entire strain history. The differences between the predicted response and the experimental data can be related to many factors such as damage experienced by the rope, variability in rope properties, assumptions included in the computational model, etc.

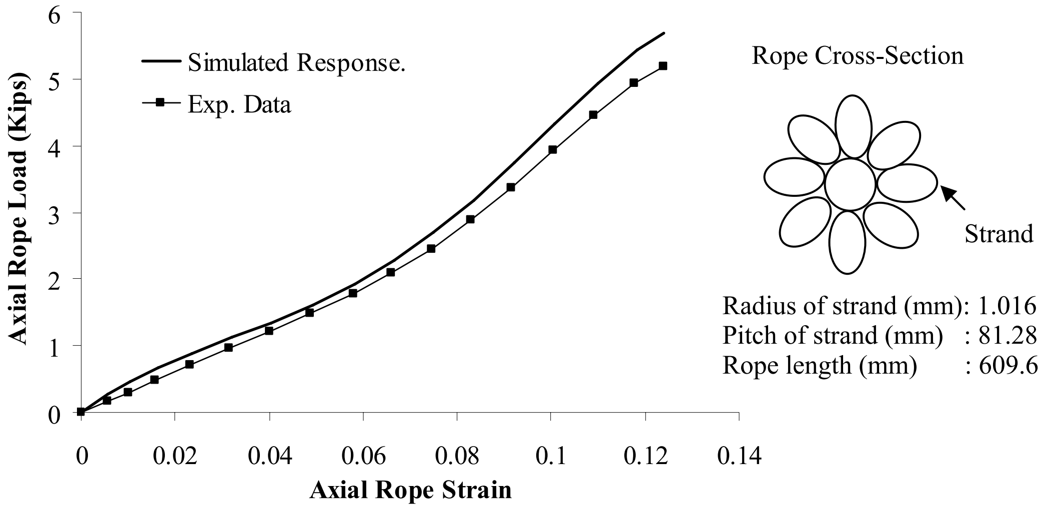

Fig. 4.1: Response of a one-level two-layer rope under monotonic strain history and cross-section and geometric parameters of the rope

In general, the analysis of a system is commonly performed assuming deterministic material properties. This approach disregards uncertainties with respect to the internal stresses, spatial variation of the mechanical properties, inhomogeneities of the material and other effects that lead to a random mechanical response of a system (stochastic response). For a realistic analysis, it is necessary to consider not only average values but also variances of the material parameters (stiffness, breaking stress, breaking strain, etc.). In order to consider stochastic material behavior, various experimental data are needed to determine the set or sets of parameters that can be used for the simulation of the random response of a system, which are associated with mean values, variances and probability density functions (Reusch and Estrin, 1998).

In this particular study, the extent of experimental data is not sufficient for a detailed statistical analysis to be performed. Accordingly, only the average values of the material parameters such as breaking stress, stiffness and breaking strain are used as input data to simulate rope response. In addition, at least in portions of a rope that are sufficiently far away from the terminations, the geometry of a rope does not present geometrical irregularities or discontinuities such as notches, holes or sharp corners that could affect the stress distribution. If irregularities or discontinuities were present, stresses near these locations would become concentrated in which small variations in the material properties may be accentuated and cause pronounced deviations of the overall stress values from the expected average behavior (Reusch and Estrin, 1998). For the reasons just mentioned, and in order to verify the assumptions made in developing the computational model including calibration of the proposed damage evolution equation, the differences between the predicted rope response and the experimental data are assumed to be related solely to the damage experienced by the rope (Fig. 4.1(a)).

Using experimental data, the values of ε_b and ε_t can be obtained directly. The value of ε_b is the strain at which a rope element (strand) reaches its maximum load, and ε_t is the strain at which the experimental curve starts deviating from the one determined by simulation. In order to compute the values of the damage parameters α_1 and β_1, concepts from continuum damage mechanics (CDM) introduced in Section 3.5.3 are invoked.

4.2 DAMAGE MEASUREMENT

In this section, two methods to quantify the evolution of damage experienced by rope elements are presented: secant moduli ratio and strain energy deviation. These methods are based on the comparison of the virgin (i.e, undamaged) curve and experimental curve (damaged) shown in Fig. 4.1.The formulation of both methods relies on the effective stress concept and principle of strain equivalence (Section 3.5.3)

4.2.1 Secant Moduli Ratio

As discussed earlier, the differences between the predicted response and the experimental data are assumed to be solely related to the damage experienced by the rope. According to the concepts presented in Section 3.5, it is expected that the damage index evolution be represented by an increasing monotonic function with values varying between 0 and 1. In order to achieve this behavior, based on the damage evolution given by Eq. (3.48b) (or Eq. (3.48d)), the following three conditions must be satisfied: (1) $f(\varepsilon, \varepsilon^2, ...)$, $g(\varepsilon, \varepsilon^2, ...) > 0$, (2) $f(\varepsilon, \varepsilon^2, ...) \geq g(\varepsilon, \varepsilon^2, ...)$ and (3) $\mathrm{d}(f(\varepsilon, \varepsilon^2, ...)) \geq [f(\varepsilon, \varepsilon^2, ...)/g(\varepsilon, \varepsilon^2, ...)]\cdot\mathrm{d}(g(\varepsilon, \varepsilon^2, ...))$ for every value of ε on $[\varepsilon_t, \varepsilon_b]$, where d() is the total derivate with respect to ε. In this particular application, the functions $f(\varepsilon, \varepsilon^2, ...)$ and $g(\varepsilon, \varepsilon^2, ...)$ are associated with the predicted response and experimental data curves, respectively (Fig. 4.1(a)). The value of ε is the axial rope strain, and it is assumed, due to the small size of the rope tested, that all rope elements (strands) experience the same axial strain as the rope. It is also assumed that the initial damage D_I (Eq. 4.1) is equal to zero.

It is important to note that the value of D, when computed using Eq. (3.48b), reaches a value approximately equal to 0.1 at the onset of failure based on the model selected for its evolution. Thus, before failure, rope elements have experienced a relatively low level of damage according to the model. This observation suggests that under increasing monotonic load, rope components have a quasi-brittle behavior and a rapid increase in the value of the damage index must occur just prior to complete failure. For each value of the strain ε, Eq. (3.48b) is applied to obtain the evolution of D based on the curves presented in Fig. (4.1a). The evolution obtained for D using this approach, however, does not satisfy the condition of being an increasing monotonic function because it fluctuates (i.e., local rate of change of damage is negative), especially for values of the threshold strain ε_t smaller than 0.04, where the oscillatory behavior of damage is more pronounced (Fig. 4.2).

As stated before, the simulation curve is always an upper bound for the experimental data, and, unlike the value for the breaking strain ε_b, the value of the threshold strain ε_t is not well defined. In addition, using Eq. (3.48b) to describe the damage index D does not satisfy the condition of zero damage for a value of a strain ε equal to ε_t (Fig. 4.2). In order to match the conditions of being an increasing monotonic function and having a zero value for strain ε equal to ε_t, a modified expression is used to compute the evolution of D, which is an empirically-based equation. The modified equation to compute the evolution of D throughout the strain history is derived using Eq. (3.48b) (or Eq. (3.48c)) and is given by

$$D(\varepsilon)=\frac{\sum_{\varepsilon_k\geq\varepsilon_t}^{\varepsilon} d(\varepsilon_k)}{H} \tag{4.2}$$

where $d(\varepsilon_k) = 1-\sigma_d(\varepsilon_k)/\sigma(\varepsilon_k)$ and $\varepsilon_t \leq \varepsilon_k \leq \varepsilon$, for every ε such that $\varepsilon_t \leq \varepsilon \leq \varepsilon_b$ and H is a normalizing constant. The values of $\sigma(\varepsilon_k)$ and $\sigma_d(\varepsilon_k)$ are the axial stress of the undamaged and damaged medium, respectively, for a particular value of the axial strain ε_k.

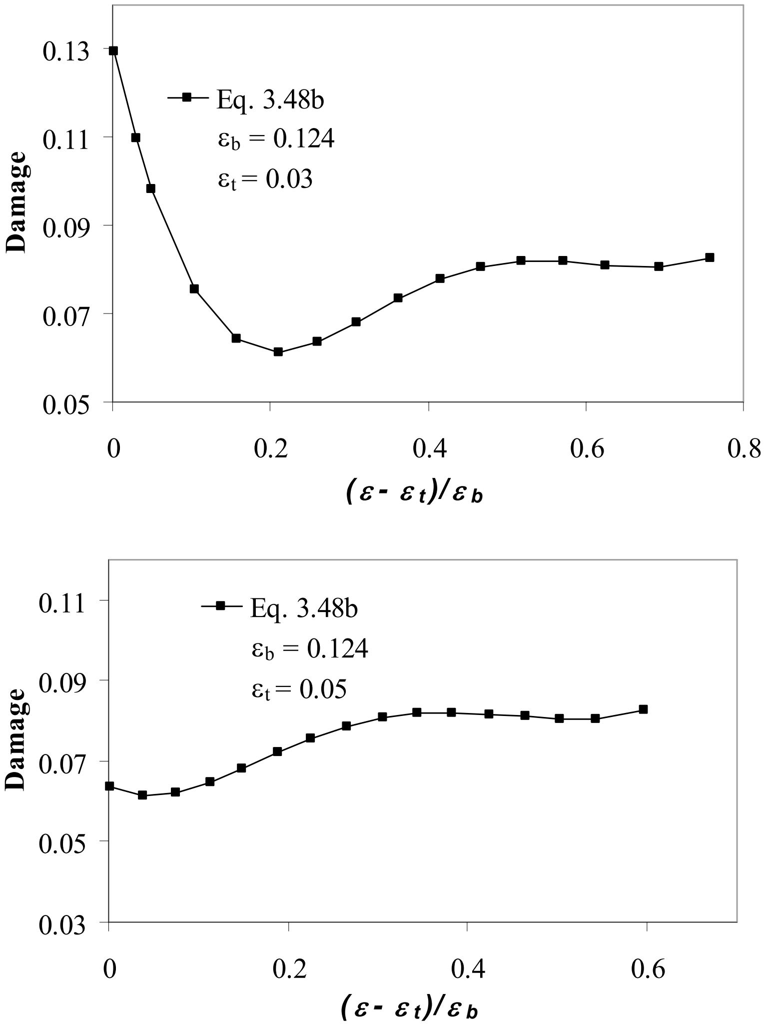

Fig. 4.2: Damage evolution based on Eq. (3.48b) for different values of the threshold strain ε_t

As previously mentioned, the direct use of Eq. (3.48b) is not appropriate for obtaining the evolution of the damage index for the case currently under investigation. Based on the results shown in Fig. (4.2), the difference between the predicted rope response and the experimental data, measured by the use of Eq. (3.48b), is not only due to damage. However, for values of the normalized variable $(\varepsilon - \varepsilon_t)/ \varepsilon_b$ greater than 0.2 for $\varepsilon_t = 0.03$, and greater than 0.1 for $\varepsilon_t = 0.05$, the use of Eq. (3.48b) results in values that meet the requirements to be considered as a valid damage model (i.e., values between 0 and 1 and increasing behavior as the value of the strain ε increases). The role of Eq. (4.2) is to smooth the values of the variable $d(\varepsilon_k)$ and construct an allowable function to measure the damage experienced by the rope for the general case.

The form of Eq. (4.2) satisfies two basic requirements of CDM principles: it ensures that the evolution of the damage index parameter $D(\varepsilon)$ is monotonically increasing and its value varies from 0 to 1. The first requirement is satisfied by accumulating the variable $d(\varepsilon_k)$, and the second one by using the normalizing constant H. It is important to note that the form of H could be more complex than a constant and may be described by a generalized function of the strain ε, and in general, will depend on the problem under study. This possibility is currently under investigation by the author. Some precautions must be taken when Eq. (4.2) is used however. As stated above, the value of the threshold strain defines when the damage starts being accumulated. Near the origin of the $\sigma - \varepsilon$ plane, there are small nonlinearities due to the rearrangement of rope elements (the so called "bedding in" effect) that are not considered to be a source of damage. For these conditions, it is best to ignore the small variations between the test and simulation values by defining a minimum value for the threshold strain.

Using Eq. (4.2) and the curves plotted in Fig. 4.1(a), the evolution of $D(\varepsilon)$ throughout the strain history is computed. For this particular application, the normalizing constant H has a value such that D will reach a maximum value equal to 0.1. This value was chosen because it is the value of the variable $d(\varepsilon_j)$ just prior to the onset of failure for individual elements within a rope. The use of this normalization scheme implies that the evolution of the damage index must vary rapidly to reach a value of one at the moment of rope element failure. Accordingly, this formulation suggests that under increasing monotonic load, rope elements have a quasi-brittle behavior, which is consistent with observations made from polyester ropes loaded to failure.

After the value for H is selected, a curve of the form of Eq. (4.1), setting the initial damage D_I equal to zero, is fitted to $D(\varepsilon)$ in order to obtain the damage parameters α_I and β_I so that the evolution of the damage index is represented as a continuous process. According to the experimental data reported by Li et al. (2002), the value of ε_b is well defined; however, as stated earlier, such is not the case for the value of ε_t. For this reason, evolution of the damage index $D(\varepsilon)$ for different values of threshold strain ε_t are presented in Fig. 4.3.

In all cases, the evolution of $D(\varepsilon)$ has a high value of coefficient of correlation (R^2) with a curve of the form of Eq. (4.1). However, for values of ε_t less than 0.03, the slope of the damage function is greater for small values of the variable $(\varepsilon - \varepsilon_t)/\varepsilon_b$ than it is for higher values of the variable $(\varepsilon - \varepsilon_t)/\varepsilon_b$. This behavior can be related to nonlinear effects rather than damage. The values of α_I and β_I depend on the value chosen for the threshold strain ε_t as is shown in Fig. 4.4. The damage index evolution becomes more linear as the value of the threshold strain ε_t increases (see Fig. 4.3).

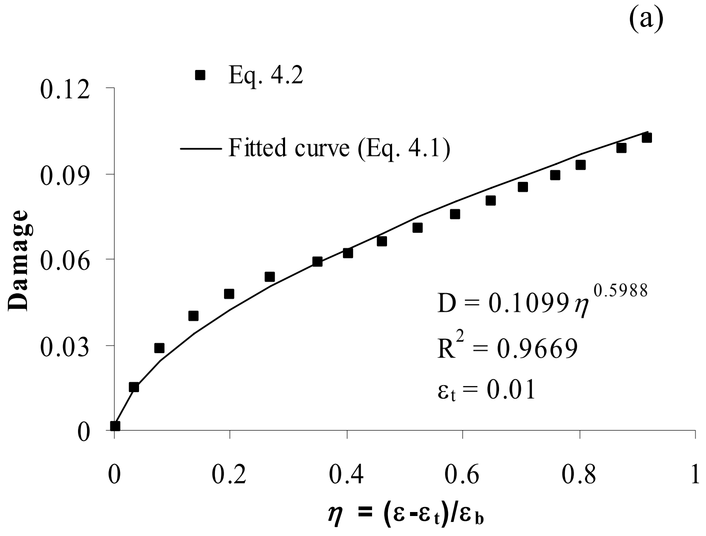

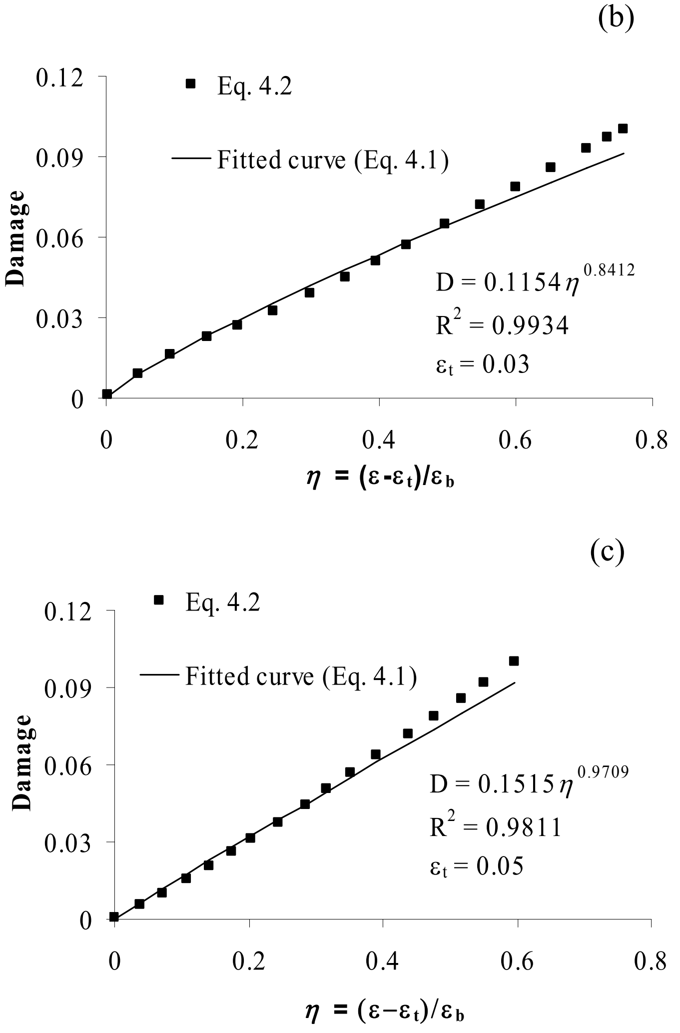

Fig. 4.3: (a), (b), (c) Damage index evolution for different values of ε_t and $\varepsilon_b = 0.124$

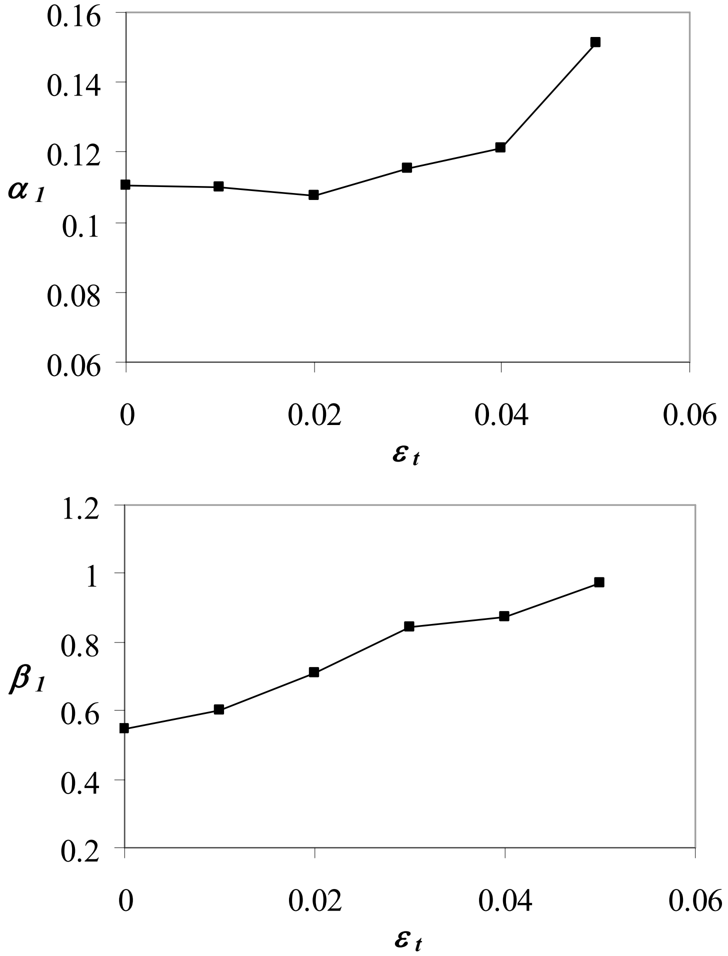

Fig. 4.4: Variation of the damage parameters α_1 and β_1 for different values of ε_t

4.2.2 Strain Energy Deviation

The density of elastic energy ψ_e of a virgin system can be defined as

$$\psi_e(\varepsilon) = \int_0^{\varepsilon} f(\rho)\,d\rho \tag{4.3}$$

where $\sigma = f(\varepsilon)$ represents the constitutive law for the virgin material and ε is the current strain of the system. For the case of the damaged system, the density of the elastic energy ψ_d can be defined as

$$\psi_d(\varepsilon) = \int_0^{\varepsilon} g(\rho)d\rho \tag{4.4}$$

where $\sigma_d = g(\varepsilon)$ represents the constitutive law for the damaged system.

Based on the concept of effective stress and the principle of strain equivalence described in Section 3.5.3, the density of the elastic energy ψ_d for the damaged system can be described as

$$\psi_d(\varepsilon) = \int_0^{\varepsilon} (1 - F(\rho))f(\rho)d\rho \tag{4.5}$$

where $F(\rho)$ is the damage index that, based on the assumption made in Section 4.1 for the case of monotonic loading, solely depends on the strain range of the system.

Defining the density of the elastic strain energy deviation (*SED*) as the difference between the density of the elastic energy of the virgin system and damaged system (Najar, 1987), the evolution of *SED*, using the property of linearity of the integral operator and the principle of strain equivalence, can be described as (Fig. 4.5)

$$SED(\varepsilon) = \int_0^{\varepsilon} F(\rho)f(\rho)d\rho \tag{4.6}$$

If it is assumed that the behavior of the virgin system $f(\varepsilon)$ and damaged system are known, the value of $SED(\varepsilon)$ can be computed for any value of ε. Thus, Eq. (4.6) becomes a linear integral equation for the unknown function $F(\varepsilon)$. This equation could be solved, for example, by replacing the integral $\int F(\rho) f(\rho)d\rho$ over the interval $[0, \varepsilon]$ by a numerical

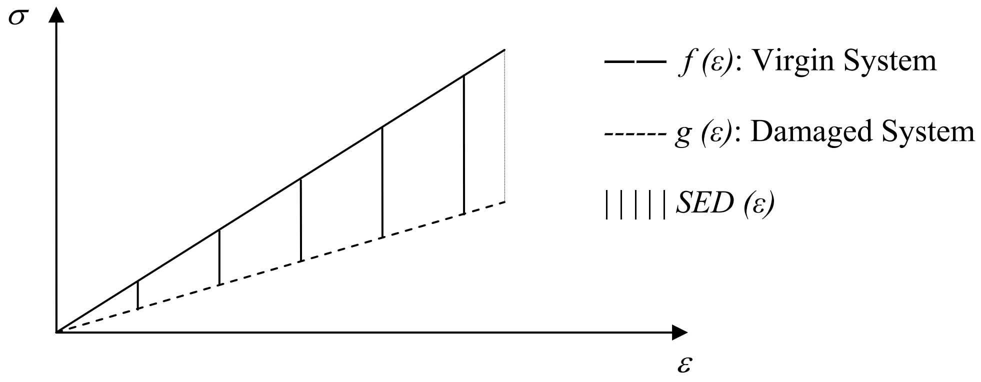

Fig. 4.5: Strain Energy Deviation (SED) definition

integration rule. Thus, the interval of integration [0, ε] is discretized into points such as $0 \leq \varepsilon_1 \leq \cdots \leq \varepsilon$ and the integral is replaced by a quadrature on these points. This procedure leads to a system of linear equations whose solution gives the values of *F(ε)* at the points in which the interval [0, ε] was discretized (Linz, 1979). If Eq. (4.6) is solved using the procedure just described, the evolution obtained for the function *F(ε)* would be the same as the one obtained using Eq. (3.48b), and consequently Eq. (4.2) would be used again to obtain an allowable damage evolution expression *F(ε)*. An alternative procedure to obtain damage evolution *F(ε)*, based on Eq. (4.6), is used in which the generalized mean value theorem for integrals is invoked.

According to Bartle and Sherbert (1982), the generalized mean value theorem for integrals states: “if *p(x)* is continuous and *q(x)* is integrable on [*a, b*] such that $q(x) \geq 0$ (or $q(x) \leq 0$) on [a, b], then

$$\int_a^b p(x)q(x)dx = p(\zeta)\int_a^b q(x)dx \tag{4.7}$$

for some ζ on [a, b]". Thus, the value $p(\zeta)$ is the weighted-average of the function $p(x)$ over the interval [a, b], with $q(x)$ the weighting function.

Considering that the function $f(\rho)$ in Eq. (4.6) is continuous on [ε_t, ε_b], and by hypothesis the function $F(\rho)$ is also continuous and positive on [ε_t, ε_b], the above theorem can be applied to the definition of *SED* given by Eq. (4.6). The following expression results:

$$F(\zeta_\varepsilon) = \frac{SED(\varepsilon)}{\int_{\varepsilon_t}^{\varepsilon} f(\rho)d\rho} \tag{4.8}$$

Thus, the damage of the system $F(\varepsilon)$ at a strain ε, such that $\varepsilon_t \leq \varepsilon \leq \varepsilon_b$, can be estimated by its weighted-average value $F(\zeta_\varepsilon)$, where ζ_ε is some point on [ε_t, ε]. Provided that the damage index F is an increasing function, the following relation holds: $F(\zeta_\varepsilon) \leq F(\varepsilon)$ for every ε on [ε_t, ε_b]. It is important to note that the denominator in above equation is the accumulated density of strain energy of the virgin system from ε_t through ε. Using the fact that an integral is a linear operator, the scalar factor L_ε can be introduced such as

$$L_\varepsilon = \frac{\int_{\varepsilon_t}^{\varepsilon} f(\rho)d\rho}{\int_{\varepsilon_t}^{\varepsilon_b} f(\rho)d\rho} \tag{4.9}$$

Thus, the factor L_ε is a measured of the stored density of strain energy at strain ε ($\varepsilon \leq \varepsilon_b$) with respect to the stored density of strain energy at strain $\varepsilon = \varepsilon_b$ (U_v) of the virgin system and $L_\varepsilon \leq 1$. Then, Eq. (4.8) can be written as

$$F(\zeta_\varepsilon) = \frac{SED(\varepsilon)}{L_\varepsilon \int_{\varepsilon_t}^{\varepsilon_b} f(\rho)d\rho} \tag{4.10}$$

for every ε on $[\varepsilon_t, \varepsilon]$. The use of Eq. (4.10) generates a series of increasing values for $F(\zeta_\varepsilon)$ less than 1 provided the following three conditions are satisfied: (1) the values of $L_\varepsilon \cdot U_v$ and $SED(\varepsilon)$ are positive on $[\varepsilon_t, \varepsilon_b]$, (2) $L_\varepsilon \cdot U_v \geq SED(\varepsilon)$ on $[\varepsilon_t, \varepsilon_b]$ and (3) $[(L_\varepsilon \cdot U_v)/SED(\varepsilon)] \cdot \mathrm{d}(SED(\varepsilon)) \geq \mathrm{d}(L_\varepsilon \cdot U_v)$ for every value of ε on $[\varepsilon_t, \varepsilon_b]$, where d() is the total derivate with respect to ε. By definition, the first two conditions are satisfied, but the third condition could not be satisfied for every value of ε on $[\varepsilon_t, \varepsilon_b]$ because, as stated in Section 4.2.1, damage is not the only cause of the deviation of the experimental curve from the virgin curve (Fig. 4.1), especially for small values of strain ε. In Fig. 4.6, Eq. (4.10) is used to obtain the evolution of $F(\zeta_\varepsilon)$ on $[\varepsilon_t, \varepsilon_b]$ for two values of ε_t, 0.03 and 0.05, as used in Fig. 4.2 (Section 4.2.1). The evolution obtained for $F(\zeta_\varepsilon)$ using this energy-based approach does not satisfy the condition of being an increasing monotonic function. In fact, the evolution obtained is similar to the evolution obtained using the secant moduli ratio method (Eq. 3.48b) presented in Fig. 4.2, but smoother. Thus, the energy-based method smoothes the damage evolution obtained by the secant moduli ratio method.

If Eq. (4.10) is used with the value of L_ε equals one for every value of strain ε on $[\varepsilon_t, \varepsilon_b]$, an increasing lower bound evolution for $F(\zeta_\varepsilon)$ on $[\varepsilon_t, \varepsilon_b]$ can be obtained. This evolution meets the CDM requirements to be considered as an allowable damage function, in which the value of $F(\zeta_\varepsilon)$, given by Eq. (4.10), at $\varepsilon = \varepsilon_b$ is achieved. The procedure described in Section 4.2.1 is again used here: the evolution of $F(\zeta_\varepsilon)$ is computed for different values of the threshold strain ε_t and then a curve is fit to the data points obtained. The use of this method, based on the strain energy deviation concept, leads to a polynomial evolution of the damage index $F(\zeta_\varepsilon)$, having the following form:

$$F = F_I + \omega_1\left(\frac{\varepsilon_m - \varepsilon_t}{\varepsilon_b}\right)^1 + \omega_2\left(\frac{\varepsilon_m - \varepsilon_t}{\varepsilon_b}\right)^2 + \omega_3\left(\frac{\varepsilon_m - \varepsilon_t}{\varepsilon_b}\right)^3 \tag{4.11}$$

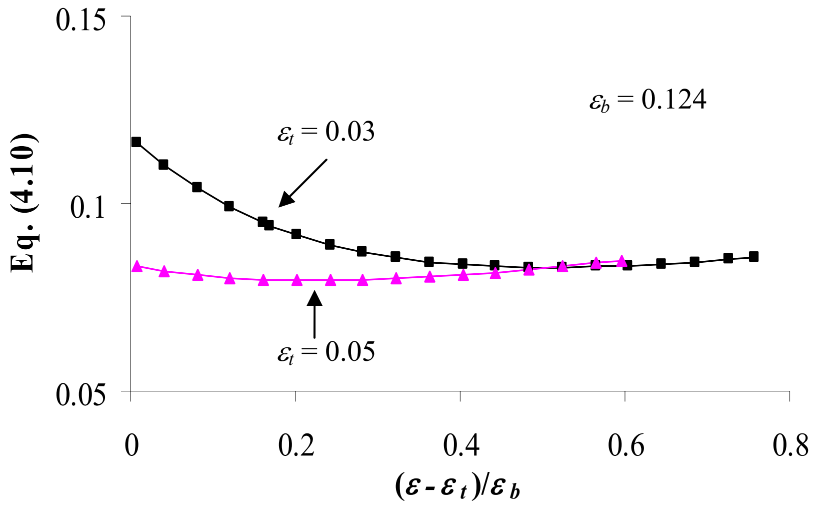

Fig. 4.6: Energy-based method (Eq. (4.10))

where the internal variable ε_m and the damage parameters F_I, ε_t, ε_b were described in section 3.5.2, being F_I the initial damage, and the parameters ω_1, ω_2, and ω_3 are obtained by fitting a curve of the form of Eq. (4.11) to $F(\zeta_\varepsilon)$ obtained based on Eq. (4.10) with the value of the factor L_ε equals to one for every value of strain ε on $[\varepsilon_t, \varepsilon_b]$. As before, the value of the initial damage F_I is set equal to zero. Evolution of the damage index $F(\zeta_\varepsilon)$ for different values of threshold strain ε_t are presented in Fig. 4.7.

4.2.3 Softening Behavior

Based on the concepts of CDM, at the moment of failure, the load carrying capacity of the system should be zero. Therefore, at a certain value of strain ε_u (ultimate strain), the system has no stress. According to the system behavior shown in Fig. (4.1), after the rope reaches its maximum load, the system should undergo a softening behavior in which the stiffness of the system decreases rapidly as strain ε increases. This effect cannot be captured for reasonable values of strain using the evolution laws of the damage index parameter proposed in Eqs. (4.1) and (4.11).

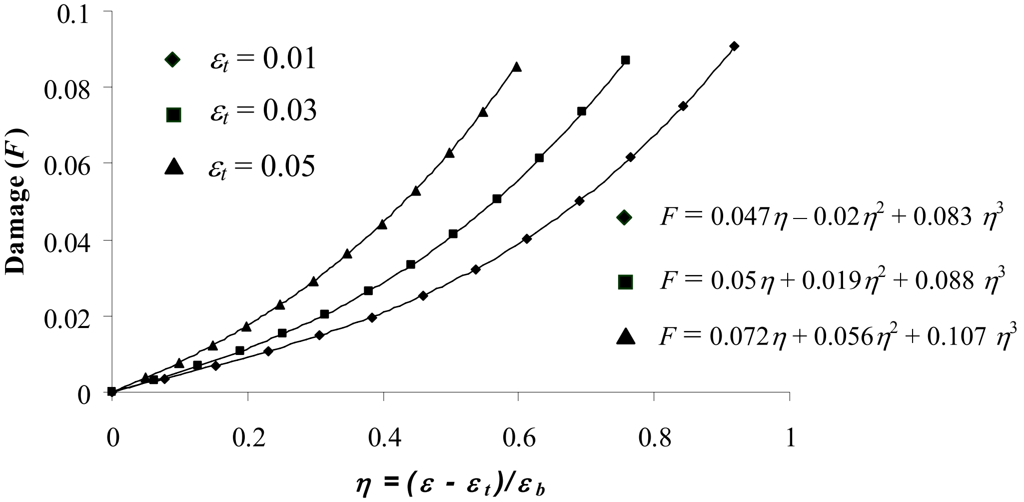

Fig. 4.7: Damage index evolution for different values of ε_t and $\varepsilon_b = 0.124$

To simulate the softening behavior of the system, it is assumed that after the maximum load is reached, the system experiences softening in a very small region of the axial force-strain plane (in comparison to the region in which the system develops its maximum capacity). The reason why this assumption is made is given later when numerical values of the damage index are obtained. In this small region, the rate of change of the slope of the damage index parameter $D(\varepsilon)$ (Section 4.2.1) or $F(\zeta_\varepsilon)$ (Section 4.2.2) ($F(\zeta_\varepsilon)$ will be also referred as $D(\varepsilon)$ in the subsequent discussion because both measures the damage of the system) governs the behavior of the system. Accordingly, the evolution of the damage index parameter $D(\varepsilon)$ can be expressed as a continuous process along the strain history of the system using the asymptotic expansion technique (perturbation method) as described below.

The kinetic equations that describe the evolution of the damage index parameter $D(\varepsilon)$ presented in Eqs. (4.1) and (4.11) along the entire strain history are (Beltran and Williamson, 2004)

$$\theta_1 \frac{d^2 D(\eta)}{d\eta^2} - \frac{dD(\eta)}{d\eta} + \alpha_1 \beta_1 \eta^{\beta_1 - 1} = 0 \tag{4.12}$$

and

$$\theta_2 \frac{d^2 D(\eta)}{d\eta^2} - \frac{dD(\eta)}{d\eta} + \omega_1 + 2\omega_2 \eta + 3\omega_3 \eta^2 = 0 \tag{4.13}$$

respectively, where θ_1 and θ_2 are constants much smaller than 1 (θ_1, θ_2 << 1), and η is a dimensionless variable defined as (ε - ε_t)/ ε_b . The boundary conditions that Eqs.(4.12) and (4.13) must satisfy are

$D(\eta) = D_I$ at $\eta = 0$ (4.14a)

$D(\eta) = 1$ at $\eta = \eta_u$ (4.14b)

In order to obtain uniform solutions (approximations) valid throughout the entire domain of these equations ($\eta_t = 0$ to η_u), a perturbation method technique is used in which the uniform solutions of Eqs. (4.1) and (4.11) are expressed as a power (perturbation) series in θ (Logan, 1997; Lagerstrom, 1988; Holmes, 1995) of the form

$$D(\eta) = D_0(\eta) + \theta D_1(\eta) + \theta^2 D_2(\eta) + \cdots \tag{4.15}$$

where the functions D_0, D_1, D_2 … are to be determined by substitution of Eq. (4.15) into Eqs. (4.12) and (4.13). The term D_0 in the perturbation series is called the leading-order term and it is the solution of the unperturbed problem ($\theta_i = 0$, $i = 1, 2$.). In this particular study, Eqs. (4.1) and (4.11) are the leading-order terms of Eqs. (4.12) and (4.13), respectively.

By construction, Eqs. (4.12) and (4.13) are singular equations because the unperturbed problem ($\theta_i = 0$, $i = 1, 2$) cannot satisfy the two boundary conditions specified (Eq. (4.14)). The singularity occurs in the vicinity of η_u where the approximate solutions of Eqs. (4.12) and (4.13) develop the so-called boundary layer region, which is a narrow interval where $D(\eta)$ changes very rapidly. Conversely, the function $D(\eta)$ varies more slowly in the larger interval called the outer region away from the ultimate strain (η_u).

The uniform approximations of Eqs. (4.12) and (4.13) are formed by an outer and inner approximation. The outer approximation is valid only in the outer region and satisfies the boundary condition at $\eta = 0$ (Eq. (4.14a)). Conversely, the inner approximation is valid only in the boundary layer and satisfies the boundary condition at $\eta = \eta_u$ (Eq. (4.14b)). Both approximations have the form of Eq. (4.15), but because of the significant changes in $D(\eta)$ that take place in the boundary layer, a new strain scale on the order of some function of θ is introduced when the inner approximation is obtained.

To obtain a composite expansion that is uniformly valid throughout the interval [0, η_u], Van Dyke's matching rule is used (Nayfeh, 1973). This rule is based on the fact that there is an overlap domain that is intermediate between the boundary layer and outer region where both expansions, inner and outer, are valid. This matching condition is illustrated in Fig. 4.8 for a function $y(t)$ that develops a boundary layer near the origin. For this particular study, consider a 2-term composite expansion of Eqs. (4.12) and (4.13) does not give more information about the evolution of the damage index than the information given by the one-term composite expansion (Appendix). Thus, just a one-term composite expansion of Eqs. (4.12) and (4.13) is used to capture the evolution of the damage index. For the case of Eq. (4.12), the composite or uniform solution for the damage index, including a non-zero value of the initial damage D_I, is given by

$$D(\eta) = D_I + \alpha_1 \eta^{\beta_1} + (1 - \alpha_1 \eta_u{}^{\beta_1} - D_I) e^{\frac{\eta - \eta_u}{\theta_1}} + \theta_1 (\alpha_1 \beta_1 \eta^{\beta_1 - 1} - \alpha_1 \beta_1 \eta_u{}^{\beta_1 - 1} e^{\frac{\eta - \eta_u}{\theta_1}}) \tag{4.16}$$

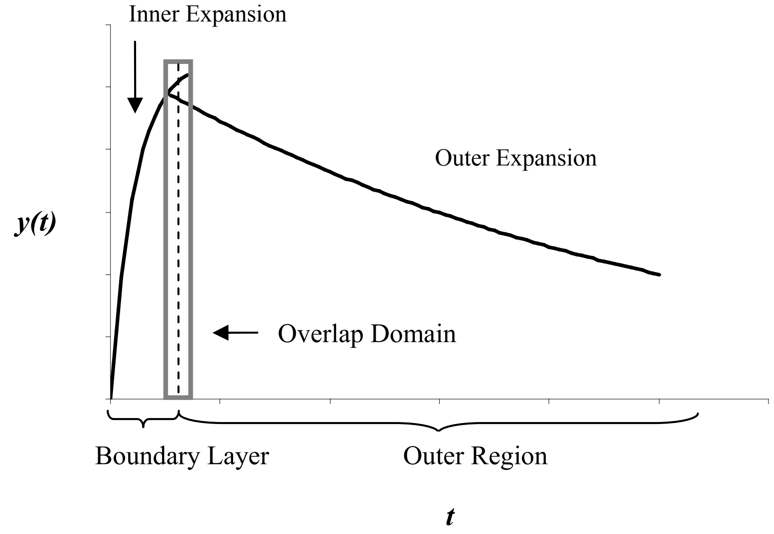

Fig. 4.8 Overlap domain

and the one-term composite expansion of Eq. (4.13) including a non-zero value of the initial damage D_I has the following form

$$D(\eta) = D_I + \omega_1\eta + \omega_2\eta^2 + \omega_3\eta^3 + \left[1 - (D_I + \omega_1\eta_u + \omega_2{\eta_u}^2 + \omega_3{\eta_u}^3)\right]e^{\frac{\eta-\eta_u}{\theta_2}} \qquad (4.17)$$

The values of the dimensionless parameters θ_1 and θ_2 are obtained by requiring equations (4.1) and (4.16), and (4.11) and (4.17) match, within a prescribed tolerance, in the outer region of the corresponding damage index evolution $D(\eta)$. Using this approach, the following condition is used to determine the value of θ_i (i = 1, 2)

$$\theta_i \le \frac{\eta_b - \eta_u}{\ln(tol)} \qquad \text{for } i = 1, 2 \qquad (4.18)$$

where the variable *tol* is the tolerance defined to guarantee that Eqs. (4.16) and (4.17) represent the damage index evolution $D(\eta)$ along the entire strain history.

Near the vicinity of $\eta_{u,}$ both damage models (Eqs. (4.16) and (4.17)) predict similar behavior for $D(\eta)$ because, in this region (boundary layer), the behavior of $D(\eta)$ is governed by the term $e^{(\eta-\eta u)/\theta}$, which is a common factor for both models. As the value of θ gets smaller, the boundary layer region gets smaller as well, making the function $D(\eta)$, discontinuous in the limit as $\theta \rightarrow 0$ (Appendix).

4.3 NUMERICAL IMPLEMENTATION

Once the evolution of the damage index is completely determined, damaged rope behavior can be simulated using either the model described by Rungamornrat et al. (2002) or the polynomial damage model presented in this study (Eq. 4.17). In Figs. 4.9 and 4.10, three types of curves are presented: simulation of the rope response without any source of damage, experimentally measured data, and simulation of damage-dependent rope response. The first two types of curves were already described and plotted in Fig. 4.1(a). For the case of the damaged rope response curves, the evolution of $D(\eta)$ computed by the energy-based method (Fig. 4.9) and secant moduli ratio method (Fig. 4.10) are used. In both cases, the value of the variable *tol* was set equal to 1E-5, the ultimate strain ε_u was arbitrarily considered to be 3% greater than the value of the strain at which the rope components reach their maximum capacity (ε_b) (just for the sake of the example), and the value of threshold strain ε_t was treated as a parameter and allowed to vary from 0.03 to 0.05. The damage parameters associated with each model are given in Table 4.1.

For the cases shown in Figs. 4.9 and 4.10, simulation curves (considering degradation model and softening behavior) agree well with the experimental curve for values of axial strain greater than 0.05. In addition, predictions made using both damage models predict the maximum axial load with very good accuracy (error varies from 0.6% to 1.5% in stress and from 1.7% to 2% in strain, with respect to the experimental data).The simulated curve (virgin rope response) that ignores the effects of damage overestimates the breaking load by 10 %. The first jump in the simulation curves is related with the failure of the core, and the second one is related with the failure of the remaining elements (Figs. 4.9 and 4.10).

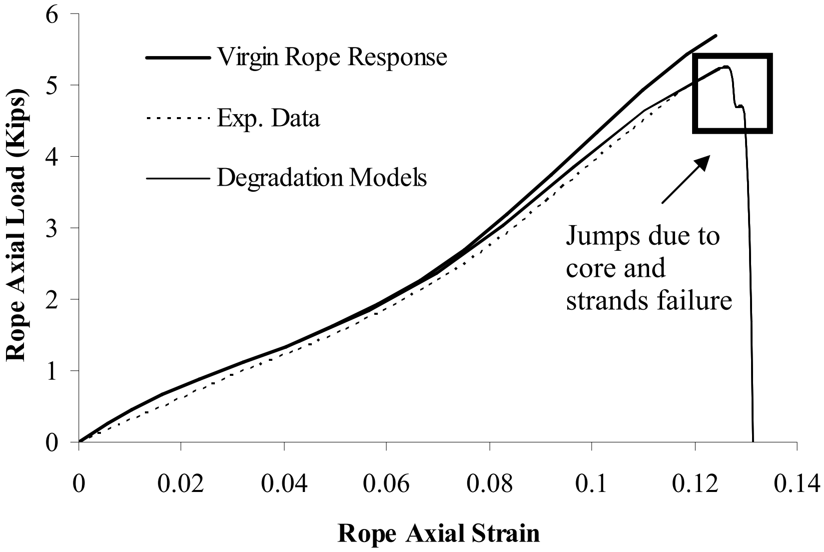

Fig. 4.9: Rope response using energy-based damage model

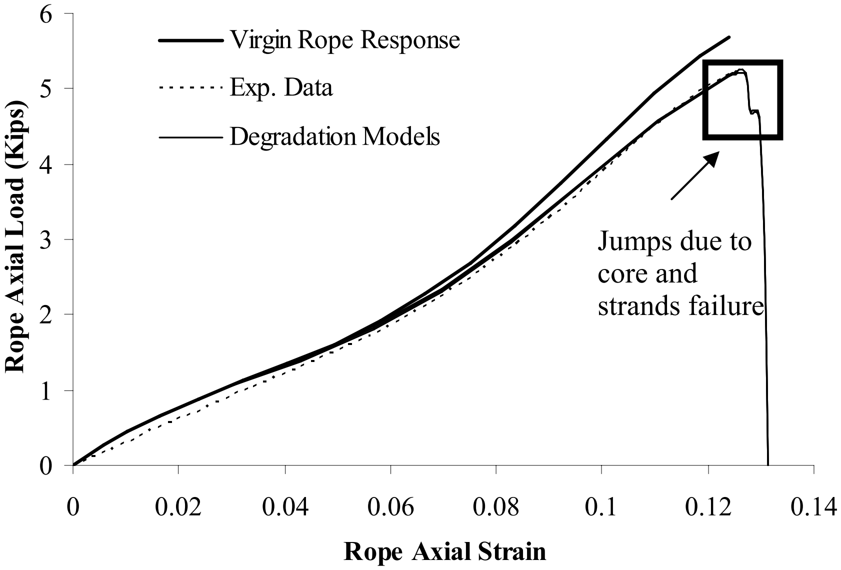

Fig. 4.10: Rope response using secant moduli ratio damage model

Table 4.1: Summary of values of damage parameters and predictions of the damage models

	Power Law Damage Evolution				Polynomial Damage Evolution				
ε_t	α_1	β_1	Max Load [kips]	Strain at max Load	ω_1	ω_2	ω_3	Max Load [kips]	Strain at max Load
0.03	0.12	0.84	5.217	0.1264	0.05	0.019	0.088	5.248	0.1261
0.04	0.12	0.87	5.251	0.1264	0.058	0.036	0.096	5.254	0.1261
0.05	0.15	0.97	5.221	0.1264	0.072	0.056	0.107	5.255	0.1261

Max. load of virgin rope response: 5.68 [kips]
Max. load experimental data: 5.19 [kips]
Strain at max. load experimental data: 0.124

A more detailed analysis in presented in Fig. 4.11. For a value of ε_t equal to 0.05, the predicted curves derived from the energy-based and secant moduli ratio methods are compared relative to the experimental data. As stated before, simulation curves agree quite well with the experimental curve and the jumps in them reflect first the core failure and then the failure of the remaining elements (strands). However, the predicted curve given by the energy-based method can be considered as an upper bound of the rope response, because it slightly overestimates the predicted curve given by the secant moduli ratio method and the experimental data.

In Fig. 4.12, the cross-section of a two-level, one-layer rope, along with its geometrical properties, is presented. This rope is composed of three rope elements of the type shown in Fig. 4.1 (b) wound around a soft core (not shown), and each rope element is formed by nine strands.

In Fig. 4.13 and 4.14, three types of curves are presented with respect to the rope cross-section shown in Fig. 4.12: simulation of the rope response without any source of damage, experimentally measured data, and simulation of rope response including damage. The difference between Fig 4.13 and 4.14 is the value of the threshold strain ε_t

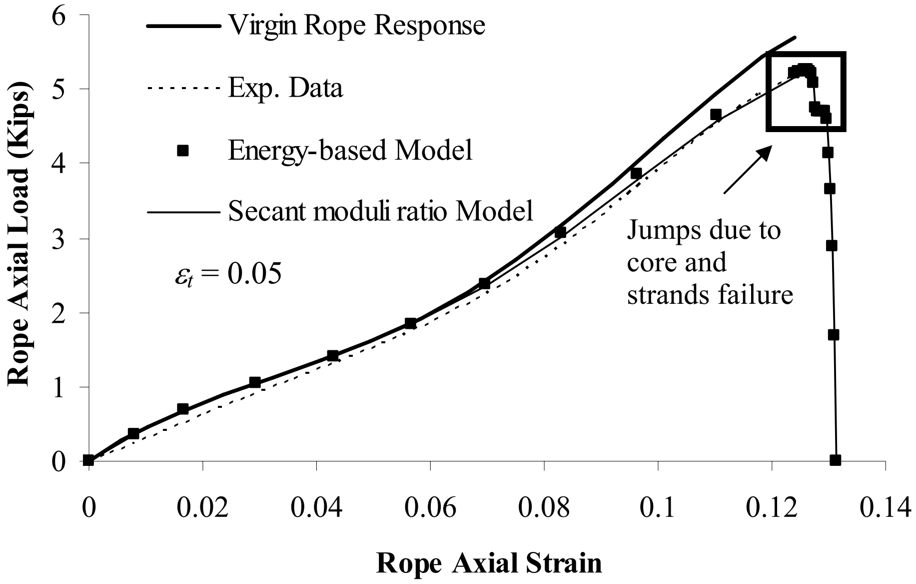

Fig. 4.11: Response of a 1 level rope under monotonic strain history: experimental, virgin response and damaged simulation curves

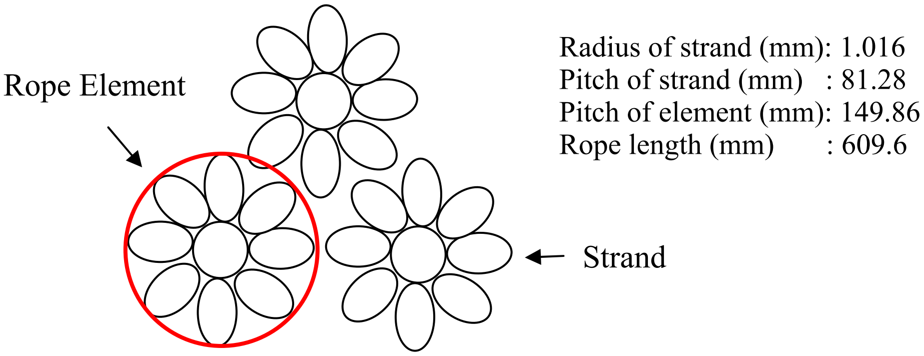

Fig. 4.12: Cross-section and geometrical properties of a two-level, one- layer rope.

chosen to compute the damaged rope response. The simulation curve without any source of damage overestimates the maximum capacity of the rope by approximately 15%. The simulation curves that include damage were computed using the damage parameters presented in Table 1 for each of the models used. In this particular analysis, a value of ε_t equal to 0.04 and 0.05 were chosen, the variable *tol* was set equal to 1E-5, and the ultimate strain ε_u was arbitrarily considered 1% greater than the value of the strain at which the rope components reach their maximum capacity (just for the sake of the example).

As in Fig. 4.11, and based on Figs. 4.13 and 4.14, the simulation curves obtained using the damage models based on the deviation strain energy and secant moduli ratio provide similar rope response along the whole strain history. For the case of the damage model based on the deviation of strain energy, these curves overestimate the maximum capacity of the breaking load by approximately 8% and in the corresponding strain by nearly 1.5%. The simulation curves based on the secant moduli ratio damage model overestimate the maximum capacity of the breaking load by approximately 6%. As with the previous method, the corresponding strain at the breaking load is overestimated by 1.5%. Similarly to Figs. 4.10 and 4.11, rope response curves show two jumps — the first one is related to the core failure of each rope element and the second one to the failure of the remaining components (strands) of each rope element (Figs. 4.13 and 4.14). Table 4.2 summarizes the damage parameters used and the predictions of the damage models.

In the previous examples, computed results were compared against data used to calibrate the damage models. As expected under these conditions, the predicted response, obtained by the use of both damage models, matches the measured values very well. To evaluate the performance of the proposed damage models, it is necessary to compare the results from simulations to data obtained from other tests. Computations were carried out using the results shown in Figs. 4.9, 4.10, 4.11, 4.13 and 4.14 and summarized in Tables 4.1 and 4.2. For the subsequent analyses, only the damage model based on the secant moduli ratio is considered. Therefore, the computational model, including the damage evolution obtained by using Eq. (4.2), is now used to predict the response of a rope that is damaged prior to testing. The damage parameters used to predict the damaged rope response were $\alpha_1 = 0.12$ and $\beta_1 = 0.87$, associated with a value of ε_t equal to 0.04. These values were selected from the results obtained in the calibration study described in Section 4.2.1.

In Figs. 4.15 and 4.16, four types of curves are presented to simulate the response of 1-level, 2-layer ropes that were damaged prior to loading: simulation of virgin rope as a reference, simulation of rope response accounting degradation of its mechanical properties (based on the proposed damage model), experimental data reported by Li et al. (2002) and simulation of rope response neglecting the contribution of cut strands (net area effect) including degradation of its mechanical properties. Also, the cross-sections of the damaged ropes are shown, indicating the rope elements that were cut prior to testing. For initial conditions, the cut rope elements are assigned a value of the initial damage D_I equal to 1 (i.e., complete failure). The geometrical parameters of the ropes are: strands radius: 1.016 mm, pitch of the strands: 81.28 mm and rope length: 609.6 mm. The damaged simulation curves agree quite well with both experimental data curves along the entire strain history and predict with good accuracy the maximum capacity of the damaged ropes.

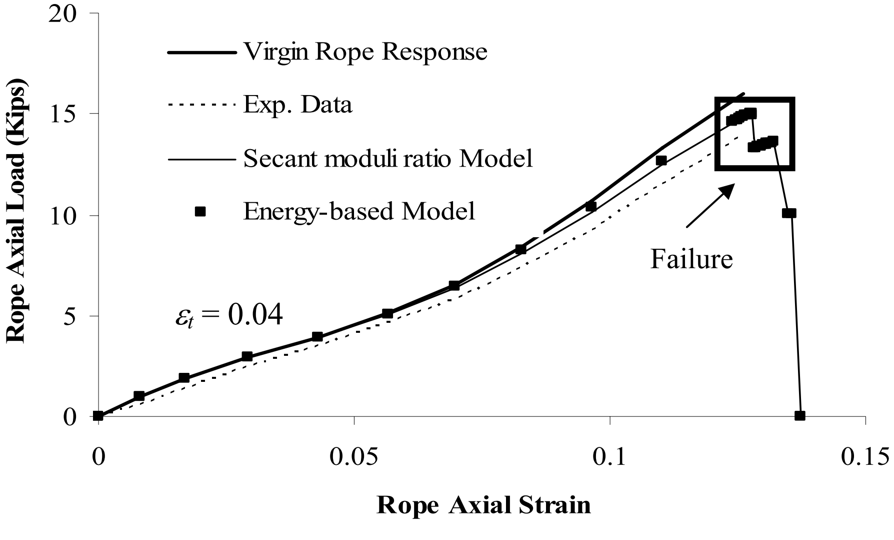

Fig.4.13: Response of a two-level rope under monotonic strain history

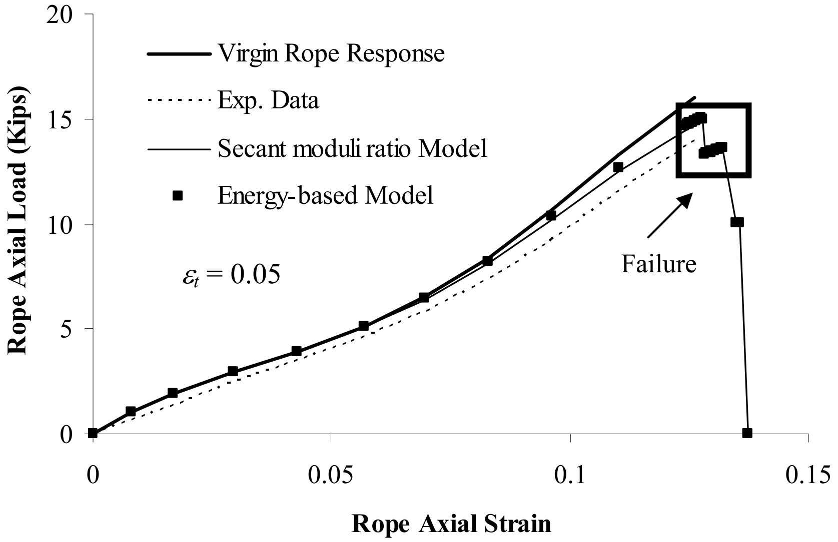

Fig. 4.14: Response of a two-level rope under monotonic strain history

Table 4.2: Summary of values of damage parameters and predictions of the damage models

Power Law Damage Evolution					Polynomial Damage Evolution				
ε_t	α_1	β_1	Max Load [kips]	Strain at max Load	ω_1	ω_2	ω_3	Max Load [kips]	Strain at max Load
0.04	0.12	0.87	14.92	0.1276	0.058	0.036	0.096	15.02	0.1276
0.05	0.15	0.97	14.87	0.1276	0.072	0.056	0.107	15.03	0.1276

Max. load of virgin rope response: 16.01 [kips]

Max. load experimental data: 13.95 [kips]

Strain at max. load experimental data: 0.126

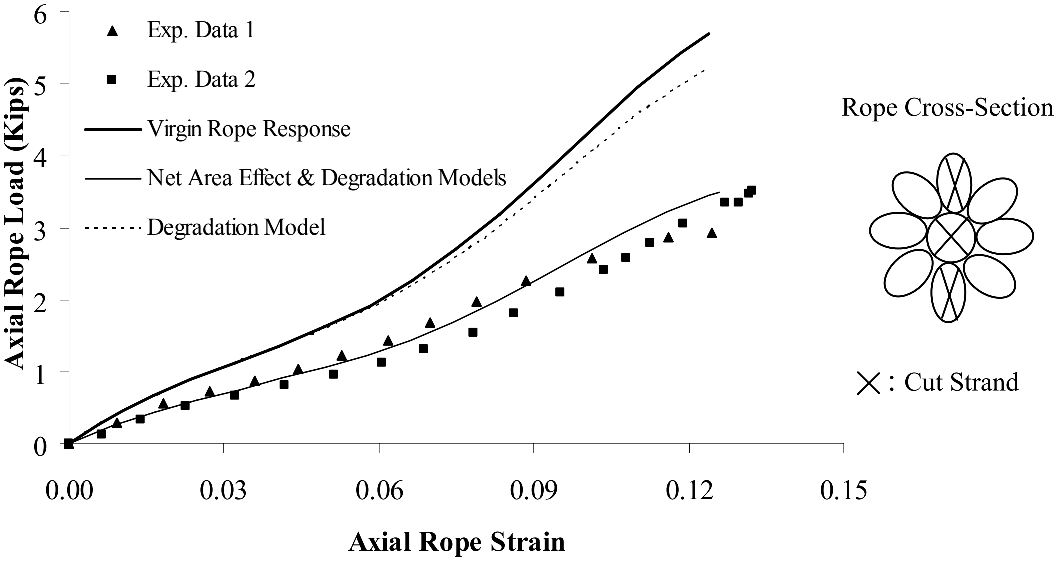

Fig. 4.15: Simulations of rope response and rope cross-section

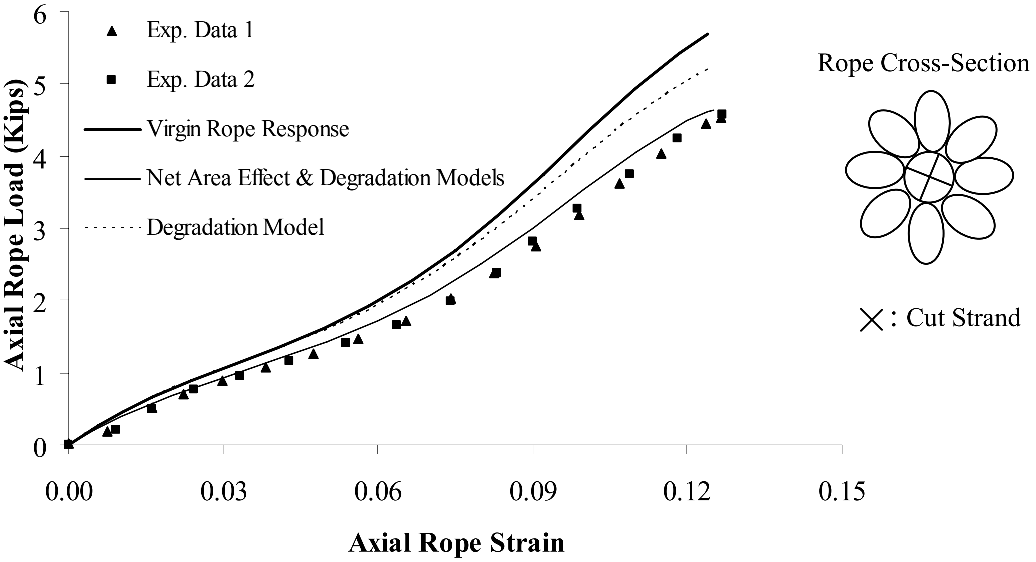

Fig. 4.16: Simulations of rope response and rope cross-section

4.4 SUMMARY

In this chapter a power law and polynomial damage evolution laws to account for degradation of synthetic-fiber ropes under increasing monotonic load have been presented. Both models rely on the concept of effective stress and the principle of strain equivalence. The damage parameters involved in both models are calibrated using available experimental data in small polyester ropes. Concepts of secant moduli ratio and strain energy deviation are used to calibrate the power law and polynomial damage laws, respectively. Softening behavior of rope elements is simulated using the perturbation method technique. Thus, damage models evolve as a continuous process from an initial value D_I through the complete failure of the rope elements (D =1). Numerical simulations compare well with available experimental data for virgin ropes (i.e., undamaged ropes, D_I = 0 for all rope elements) and initially damaged ropes prior loading (i.e., $D_I > 0$ for some rope elements). A numerical procedure to estimate the effect of rope elements failure (D =1) on overall rope response is presented in the next chapter.

CHAPTER 5

Numerical Simulation of Damage Localization in Synthetic-Fiber Mooring Ropes

In this chapter, an analytical model to estimate the effects of damage on overall rope response is presented. Damage can be represented through a degradation of the properties of individual rope components, and it can also include the complete rupture of one or more elements. The general assumptions made to estimate the length over which damage propagates along the rope length and the numerical procedure developed to account for this length are explained in this chapter. In addition, numerical predictions of polyester rope response are compared with experimental data obtained from static capacity tests.

5.1 OVERVIEW

In the previous two chapters, a computational model to predict the behavior of synthetic-fiber ropes was presented, addressing the issue of strength and stiffness degradation through the use of a damage index. For rope elements that have a damage index less than 1 (i.e., $D < 1$), the damage-dependant response can be computed using the equations described in Section 3.5.3. In this chapter, a numerical procedure is proposed to account for the effect of rope element(s) failure (i.e., $D = 1$) on overall rope response. This feature of the computational model is considered to be essential given the results of observations made from recent experimental studies on large-scale damaged ropes (Ward et al., 2005).

Several studies have shown that if friction develops along rope elements, a broken rope element is capable of supporting its total share a load within a relatively short distance of the rupture location. This length is called the *recovery length* and is defined as the distance measured from the failure end of a broken rope element to the point at which this element resumes carrying its proportionate share of axial load. The frictional forces that develop depend on the contact forces between rope elements (due to their helical nature) and the surface characteristics (i.e., coefficient of friction) of the elements in contact.

The value of the recovery length, and thus the effect of rope element failure on overall damaged rope response, depends on the type of rope construction as well as the position and number of broken rope elements distributed around a rope cross-section. If multiple rope elements fail in a relatively short length of a rope, strain localization around the failure zone could develop, as can damage localization. Aside from the load carrying capacity, the rope breaking strain and stiffness are dependant upon the number of broken rope elements, their failure locations along the rope length, and whether or not their recovery lengths are fully developed.

Hankus (1981), Chaplin and Tantrum (1985), and Cholewa (1989) have carried out experimental studies for measuring the recovery lengths of individual wires in axially loaded cables (strands and ropes). These references have recommended a range of values for the recovery length expressed as a percentage of the strand pitch of the rope or rope diameter.

On the theoretical side, Chien and Costello (1985) published an analytical model for estimating the recovery length in cables. They used the rigid-plastic Coulomb friction model and invoked Saint-Venant's principle to investigate the recovery length of the central (straight) core wire of a seven-wire helical strand, and they also studied the recovery length associated with the outer layer of six-strand ropes. Raoof (1991) extended the theoretical model of Chien and Costello (1985) to include the transition between full-slip and no-slip friction interaction along the core wire of an axially pre-loaded, multi-layered helical strand. This model was also used by Raoof and Huang (1992) to address the problem of estimating the recovery length in parallel wire cables prestressed by external wrapping or intermittent bands. This later problem was originally studied by Gjelsvik (1991); only the case of full slippage along the entire recovery length was considered. As with the previous work by Chien and Costello (1985), Gjelsvik's (1991) work relied upon the rigid-plastic Coulomb friction model.

Raoof and Kraincanic (1995 and 1998) presented a theoretical model for determining the recovery length in helical wires in any internal layer of an axially loaded, multi-layered spiral strand. Their model accounts for the effects of hoop and radial inter-wire contact forces, and they suggested a direct procedure for determining the recovery length of a broken wire. Subsequent theoretical parametric studies over a wide range of cable configurations, including changes in wire diameters and helix angles, led to recommendations concerning the determination of the required minimum length of test specimens to be used for axial fatigue tests in order for the test results to represent the actual behavior of longer cables under service conditions.

For the current research, the works by Chien and Costello (1985) and Raoof and Kraincanic (1995 and 1998) were extended for the case of synthetic-fiber ropes to compute the recovery length value of a failed rope element. The resulting model considers the rope cross-section modeling presented in Chapter 3 (Section 3.3) to compute the normal forces acting on rope elements and the fact that a rope cross-section can consist of many levels of components (Section 3.1). The numerical algorithm presented by Raoof and Kraincanic (1998) to compute the value of the recovery length was also extended to consider the case of a nonlinear relationship between frictional forces and contact forces, as the one given by Eq. (3.37) if the parameter *b* is different than 1.

5.2 THEORY: CALCULATION OF NORMAL FORCES AND RECOVERY LENGTH

In general, there are two basic approaches for quantifying the effect of a broken rope element(s) on overall rope response: (1) ignore the contribution of the broken rope element(s) after failure (the so-called net area effect), and (2) include the contribution of the broken rope element(s) after determining its (their) recovery length value(s). In essence, however, both of these models can be considered as depending upon the estimated length over which rope damage (broken rope element(s)) propagates along the rope length. For the case of the net area effect model, rope damage is assumed to propagate over a distance greater than the rope length (i.e., the recovery length required for a failed rope element to resume carrying load exceeds the length of the rope). Accordingly, broken rope elements do not contribute to rope response after their failure. With this approach, the stiffness and strength loss of the rope are proportional to the area that the broken rope elements represent with respect to the total rope area, and the rope breaking strain remains unchanged. This effect on rope response is captured by the computational model presented in Chapters 3 and 4, neglecting the potential lack of symmetry of the rope cross-section.

A rope element can fail at any position along its length. Contrary to the net area effect concept, theoretical investigations and tests on actual ropes suggest that a broken element can eventually start contributing to rope response. The ability of a broken element to resume carrying load will depend upon the value of its recovery length and whether or not it is physically admissible. For example, if the failure region of a broken rope element is located at the mid-length position, the value of the recovery length of this broken rope element is admissible if it is smaller than $L/2$, with L defined as the total rope length. If such is the case, a strain localization region around the failure site could develop, and, based on the damage model, damage localization may also occur. This damage localization can cause the premature failure of rope elements, reducing the maximum load and maximum strain that the damaged rope is capable of resisting.

In order to estimate the value of the recovery length of a broken rope element, the normal forces exerted on this element must first be computed. In general, a rope element is subjected to normal forces in two directions: radial (inter-layer contact forces) and circumferential (inter-element contact forces). Thus, assuming a friction model based on normal forces, the gradual increase in tension in a broken rope element is partly due to the radial forces exerted on the broken rope element from the inner and outer neighboring layers and partly due to the circumferential forces exerted on the broken rope element from the unbroken rope elements in the same layer. In Fig. 5.1, the pattern of inter-layer/inter-element contact forces in an axially loaded rope element is presented. The $g_{i+1,i}$ and $g_{i-1,i}$ are the line inter-layer contact forces exerted on a rope element located in layer i by rope elements of layer $i+1$ and $i-1$, respectively; $p_{nc,i}$ is the line inter-element contact force exerted on a rope element located in layer i by the other elements of the same layer i; and X_i is the is the radial line body force necessary to preserve the helical geometry of a rope element.

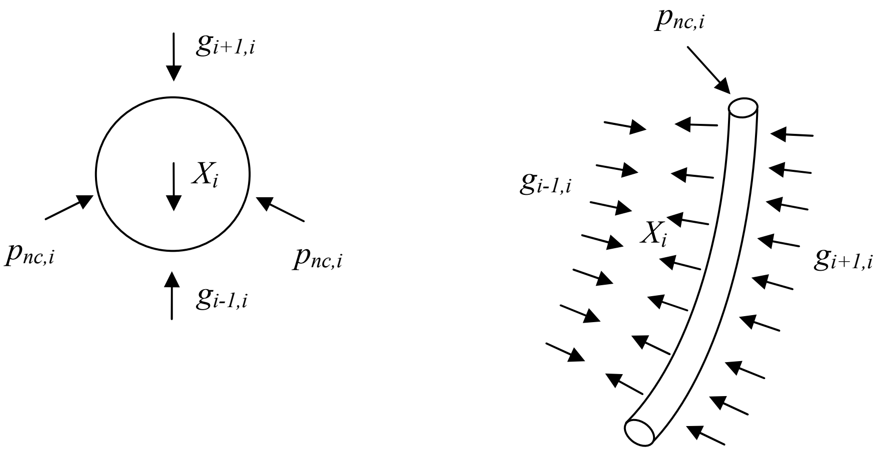

Fig. 5.1: Pattern of inter-layer/inter-element contact forces in an axially loaded rope element

Based on the cross-section modeling of rope elements presented in Chapter 3 (Section 3.3), two types of patterns of inter-layer/inter-element contact forces in an axially loaded rope element are considered. In packing geometry, contact between rope elements in the same level is assumed to be only in the radial direction (inter-layer contact forces). With wedging geometry, radial contact is assumed to be negligible in comparison to the circumferential contact and is ignored for computational purposes. However, there exists an inter-element type of contact between rope elements in the same level for a given layer for ropes with wedging geometry. Accordingly, based on this discussion, one can note that the value of the contact normal forces exerted on a broken rope element, its gradual increase in tension for a given friction model, and the value of its recovery length depend on the modeling of the rope cross-section for the particular case being evaluated. Considering the case of a one-level rope, Beltran and Williamson (2005) presented a derivation of the equations that govern the gradual increase in tension in a broken rope element for each type of contact pattern previously described, considering the friction model given by Eq. (3.37). Having the prescribed value of the tension force that the broken element should achieve based on the equilibrium equations and the geometric parameters of the broken rope element, such as curvature and helix angle, the equations that govern the gradual increase in tension in that broken rope element can be used to estimate the value of its recovery length.

5.3 NUMERICAL ANALYSIS OF DAMAGED ROPES

To evaluate and quantify the effect of rope element failure on overall rope response, it is first necessary to determine if broken rope elements can take up their appropriate share of axial load by considering the equilibrium equations that govern rope behavior and computing their recovery lengths. In order to simplify the analysis, the gradual increase in load carried by broken rope elements that develop admissible recovery lengths is ignored. Thus, only the full value of axial load at distances outside the recovery length is taken into consideration.

As previously mentioned, Beltran and Williamson (2005) studied the problem of recovery length in synthetic-fiber ropes in which the inter-layer/inter-element contact forces are induced between rope elements because of their helical nature. It is also important to note, however, that contact forces between rope elements can be induced by the confinement exerted by the rope jacket. In general, a typical rope jacket has a double braid construction. In order to represent its effect on the radial pressure exerted on rope elements, the rope jacket is considered as a thin-walled tube for the purposes of modeling. In Fig. 5.2, the effect of the rope jacket thickness on the value of the recovery length of a rope element, along with the rope cross-section of a 1-level, 2-layer rope, is presented. For comparison purposes, the rope cross-section is modeled with both a packing and a wedging geometry, and one rope element of the outermost layer is initially cut at the rope midspan. For the sake of the example, the constitutive axial law of the rope jacket is assumed to be the same as that of the rope elements (strands). As expected, as the jacket strength increases and provides more confinement to the rope, the recovery length associated with a broken element decreases relative to the case in which no jacket is present.

The recovery length of the broken rope element is computed for a prescribed deformation level of the rope (ε, ψ), where ε is the rope axial strain and ψ is the rate of twist of the rope cross-section. If this value is admissible (i.e., within the physical length constraints of the rope being analyzed), the rope is discretized into "sub-rope" elements (S_i), with lengths L_{Si}, based on the value of the recovery lengths computed. In Fig. 5.3, two possible rope discretizations are presented along with the "sub-rope" element cross-sections, where the broken rope elements have been identified with an "X." The values of u and φ are the rope axial displacement and the rope axial rotation, respectively. The two possible discretizations are based upon the location of the failed rope component: (a) the failure region is located near one end of the rope (splice), and (b) the failure region is located near the rope midspan.

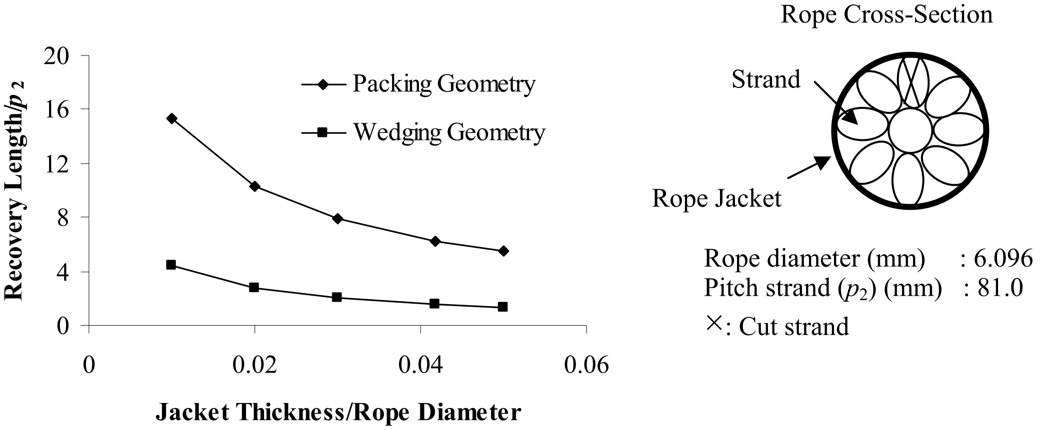

Fig. 5.2: Effect of the rope jacket on the recovery length value

Each "sub-rope" is modeled as a two-noded axial-torsional element of length L_{Si}, with two degrees of freedom at each node: axial displacement (u_i) and axial rotation (φ_i). Associated to these degrees of freedom are the corresponding axial force F_i and torsional moment M_i (Fig. 5.4). This model captures the effect of having a weakened cross-section acting over a localized region defined by the recovery length.

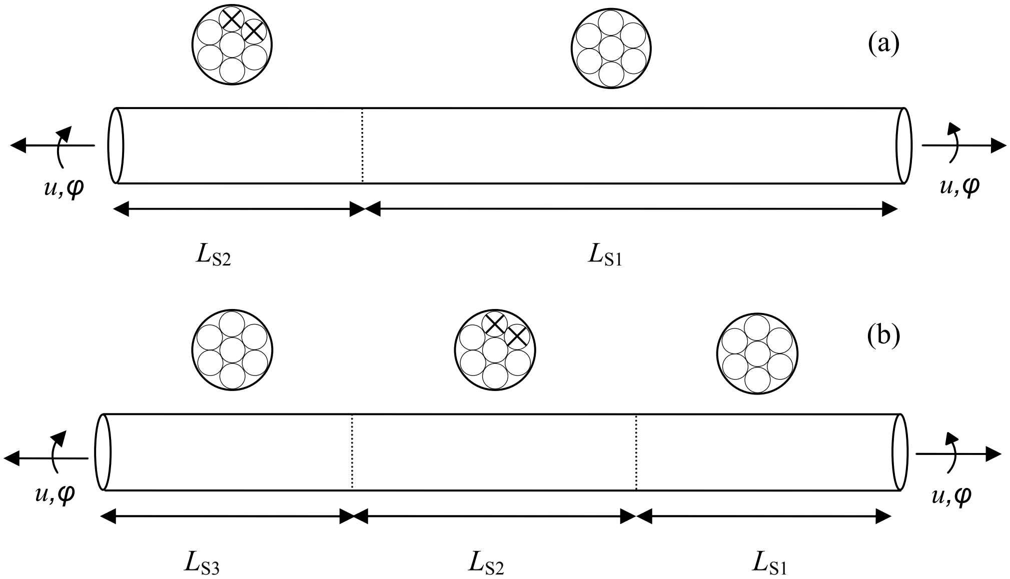

Fig. 5.3: Damaged rope discretizations: (a) failure located at one end of the rope and (b) failure located around the midspan of the rope

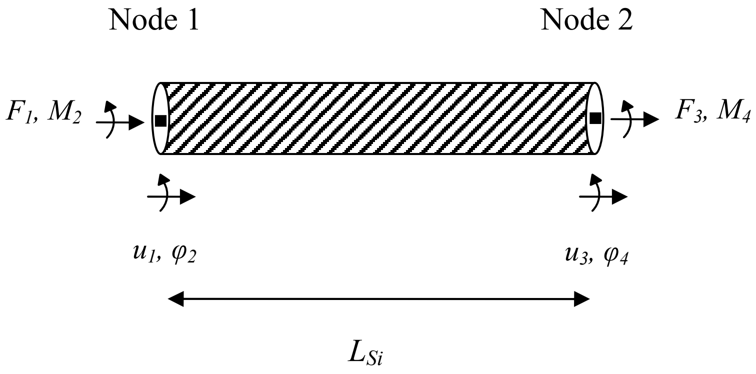

Fig. 5.4: Two-noded axial-torsional "sub-rope" element

The tangent stiffness matrix of each "sub-rope" element S_i is computed, and then each tangent stiffness matrix is assembled to obtain the tangent stiffness matrix of the entire rope. For each “sub-rope” element, a 2-by-2 stiffness matrix is computed having the following form:

$$[\boldsymbol{k}_{sr}]_i = \begin{bmatrix} k_{\varepsilon\varepsilon} & k_{\varepsilon\psi} \\ k_{\psi\varepsilon} & k_{\psi\psi} \end{bmatrix}_i$$

(5.1)

where no closed-form expressions exist to compute the stiffness coefficients due to the nonlinear geometry and nonlinear constitutive laws of the rope elements. Thus, these coefficients are computed by inducing small perturbations $(\delta\varepsilon, \delta\psi)_i$ to a prescribed level of deformation $(\varepsilon, \psi)_i$ for each “sub-rope” element S_i. These induced perturbations are applied separately, generating two different perturbed deformations. At each perturbed deformation level, the strains and deformations, constitutive laws, including the effects of damage, and the equilibrium equations of each rope element are used to compute the corresponding axial force and twisting moments of the “sub-rope” element S_i. These computed loads, along with the loads associated with the unperturbed deformation level $(\varepsilon, \psi)_i$, are used to compute the stiffness coefficients (Beltran and Williamson, 2005). The 4-by-4 tangent stiffness matrix $[\boldsymbol{K}_{sr}]_i$ of the “sub-rope” element S_i described in Fig. 5.4 can be obtained through consideration of equilibrium. Thus, with the 2-by-2 “sub-rope” element stiffness matrix $[\boldsymbol{k}_{sr}]_i$ computed, $[\boldsymbol{K}_{sr}]_i$ can be calculated as follows:

$$[\boldsymbol{K}_{sr}]_i = \begin{bmatrix} [\boldsymbol{k}_{sr}]_i & -[\boldsymbol{k}_{sr}]_i \\ -[\boldsymbol{k}_{sr}]_i & [\boldsymbol{k}_{sr}]_i \end{bmatrix} \tag{5.2}$$

A displacement control analysis is carried out to obtain overall rope response. Increments in axial strain, $\delta\varepsilon$, and axial rotation per unit length, $\delta\psi$, are specified for the entire rope. The aim of the analysis is then to obtain the values of the increments of axial displacements δu_i and axial rotations $\delta\varphi_i$, as well as the increments in the external loads (axial force and torsional moment), required to produce the specified increment in the deformation level $(\delta\varepsilon, \delta\psi)$ of the rope. Increments in axial strain and axial rotation per unit length (ε_i and ψ_i, respectively), for each “sub-rope” S_j (j = 1, 2, 3) are computed using the standard engineering strain definition. Using the damage-dependant constitutive equations corresponding to the current level of rope deformation, the increments in forces on the “sub-rope” elements due to axial deformations are then computed. Because of the nonlinearity of the system properties, iterations are performed until equilibrium is achieved.

5.4 NUMERICAL EXAMPLES

The analyses presented hereafter are carried out on polyester ropes that were damaged prior to loading. The damage introduced to such ropes was made by cutting a predetermined number of rope elements, either at the rope midspan or near one of the rope splices (ends). When data are available, numerical predictions of rope response are compared with experimental results obtained from static capacity tests. For the sake of the analyses, all ropes are modeled as two-level ropes, and the following frictional and damage parameters were assumed for the analyses (Eqs. (3.37) and (4.1)): $f_a = 0$, $\mu = 0.1$ and $b = 1$, $\alpha_1 = 0.12$, $\beta_1 = 0.84$, $\varepsilon_t = 0.04$. These values were obtained from numerical parameter studies performed on small-scale ropes that were tested previously (Li et al., (2002)). For clarification purposes, a description of the legends used in the upcoming plots and analyses is presented in Table 5.1.

Fig. 5.5 shows the damaged cross-section of a two-level rope along with some of its geometrical parameters used for the present example. Fig. 5.6 provides the analysis results for the response of this rope. For computational purposes, the second level of the rope is modeled using wedging geometry, and the first level of the rope is treated as having a packing geometry. Results computed with the net area effect and degradation model and the strain localization and degradation model accurately predict the damaged rope response for two of the three sets of experimental data (Li et al. (2002)) presented in Fig. 5.6. This figure shows that the model with strain localization effects results in a stiffer rope response that corresponds better with the experimental data and provides a smaller value of the rope breaking strain relative to the net area effect model. Both of these models, however, give values of rope breaking strain and rope breaking load that are smaller than those indicated by the test data. The difference between the theoretical upper bound response curve and the other curves is mainly due to the effects of the degradation of each rope element's properties throughout the response history and the helical nature of the rope geometry.

Table 5.1 Summary of the models used to predict damaged rope behavior

Model	Outline of the model
Strain Localization and Degradation Model (Including Net Area Effect)	The recovery length of each broken rope element is computed. If this value is admissible, the rope is discretized into "sub-rope" elements, and the numerical procedure outlined in Section 5.3 is used to analyze the rope. Degradation of each "sub-rope" element's properties is accounted for through use of Eq. 4.1. The broken rope elements do not contribute to the rope response.
Net Area Effect and Degradation Model	The broken rope elements do not contribute to the rope response. Degradation of each rope element's properties is accounted for by using Eq. 4.1.
Theoretical Upper-Bound Response	The rope response is obtained by summing up the response of each rope element, ignoring the effects of degradation.
Degradation Model (Lower-Bound Response)	The rope is considered initially undamaged and degradation of each rope element's properties is accounted for by using Eq. 4.1.

The analysis presented in Fig. 5.6 was for a two-level damaged polyester rope with helical geometry in both levels. The following analysis is on damaged polyester-jacketed ropes that have parallel, unjacketed sub-rope constructions, where each sub-rope is built by twisting a certain number of strands together. For analysis purposes, the damage inflicted to each rope prior to loading is at the strand level. This damage is simulated by cutting (i.e., specifying a damage index $D = 1$) a certain number of strands to reduce the cross-sectional area by a prescribed percentage.

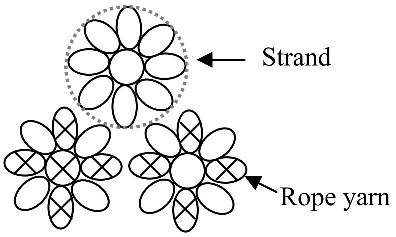

3 twisted strands
9 twisted rope yarns per strand
Rope diameter (*d*): 14 [mm]
Pitch of strand: 150 [mm]
Pitch of rope yarn: 81 [mm]
Damage inflicted at rope midspan

Damaged rope cross-section

×: Cut rope element

Fig. 5.5: Damaged cross-section of a two-level rope

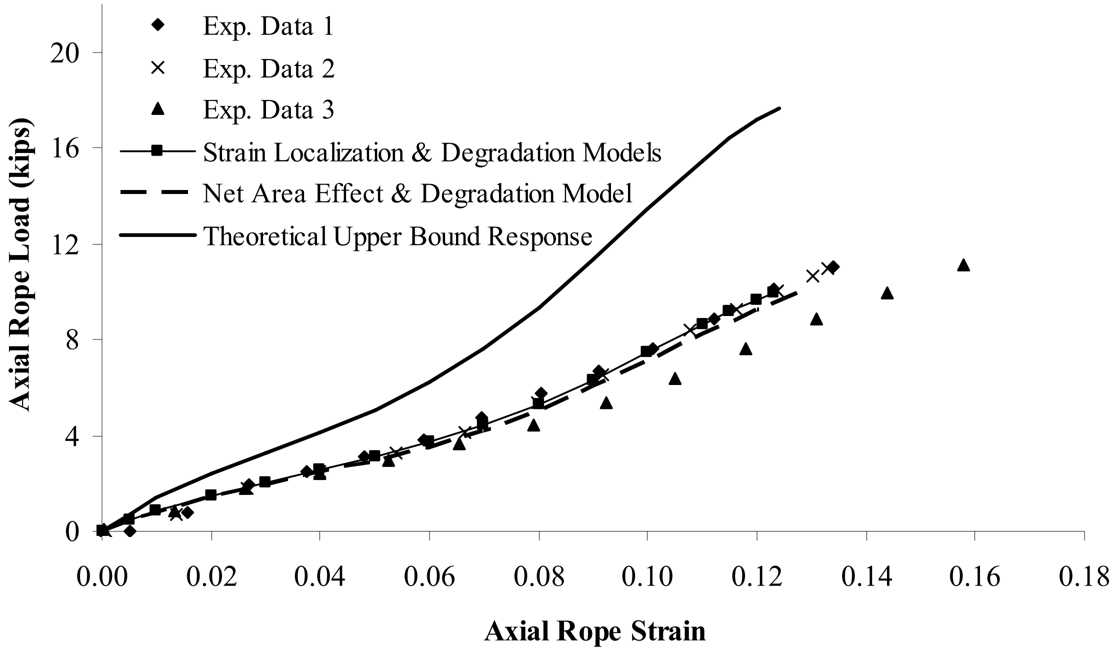

Fig. 5.6: Predicted responses of an initially damaged two-level rope

All damage is inflicted to adjacent sub-ropes near the exterior of the rope to simulate surface damage. For most of the analyses, damage is inflicted at the midspan location. If damage occurs near a rope splice, it is identified in the corresponding plot. Three different levels of initial damage (5%, 10%, and 15% of net area loss from the rope cross-section) are considered in the analyses along with different *L*/*d* ratios, where *L* is the rope length and *d* is the rope the rope diameter. Parameters are selected to study the potential influence of length effects on overall damaged rope response.

The numerical simulations of damaged rope behavior are compared with experimental data for ropes with a specified breaking strength of 35 Tonnes (77.2 kips) and 700 Tonnes (1543.2 kips). The ropes and the experimental results are documented in Ward, et al. (2006(a) and 2006(b)). For convenience, the rope constructions and simulated damage are illustrated in Figures 5.7 - 5.13. As stated before, the following analyses are for jacketed ropes that have parallel, unjacketed sub-rope constructions. Contractual agreements for the experimental program preclude association of specific results with individual rope manufacturers in external publications. Accordingly, test specimens are simply identified as Rope 1, Rope 2, Rope 3, etc. in the material presented below.

For analysis purposes, to study the potential non-uniform strain distribution along the damaged rope length, the confinement exerted on the rope by the external rope jacket is considered using the thin-walled tube approximation described previously. It is further assumed that the axial capacity of the jacket is equal to 3% of the initially undamaged rope breaking load. Because the actual value is not known and has not been measured, a small value that is believed to be representative of the rope jacket capacity has been approximated. Furthermore, results from parameter studies using different values for the assumed axial capacity of the jacket show small differences in the overall computed response of a rope. Only for those cases in which the jacket strength is ignored or is selected to be an unrealistically large value do the results deviate from those presented below.

For the analysis of each rope, four curves are presented: the theoretical upper-bound response, the net area effect and degradation model, the strain concentration and degradation model, and the degradation model. To obtain the predicted rope responses, a Poisson's ratio equal to 0.25 has been assumed. Assumptions associated with each of these cases are outlined in Table 5.1. In addition, a detailed study is presented for the effect of the *L*/*d* ratio on the residual strength and residual maximum axial strain of the damaged ropes. These two residual quantities are characterized as the ratio of the damaged to undamaged value of each parameter and are compared with the ones obtained from the experimental data to study their dependence on the *L*/*d* ratio. Figs. 5.7-5.25 below show schematics of damaged rope cross-sections, geometric properties of the ropes being analyzed, axial load response predictions, and comparisons of the damage-dependant response to the undamaged case.

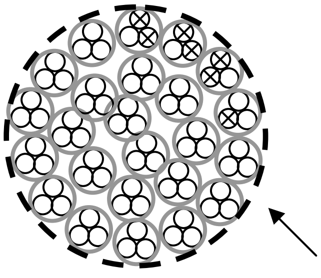

24 parallel unjacketed sub-ropes
3 twisted strands per sub-rope
70 twisted yarns per strand
Rope diameter (*d*): 32 [mm]
Specified Breaking Strength: 35 tonnes (77.2 kips)

Fig. 5.7: 35 Tonne rope with 24 subropes and simulated damage (10% of cross-section)

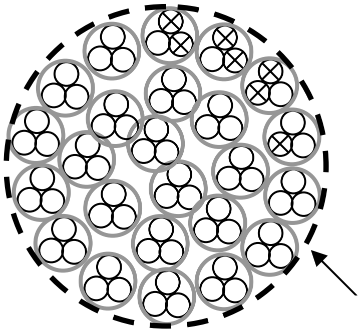

24 parallel unjacketed sub-ropes
3 twisted strands per sub-rope
22 twisted rope yarns per strand
70 twisted yarns per rope yarn
Rope diameter (*d*): 160 [mm]
Specified Breaking Strength: 700 tonnes (1543.2 kips)

Fig. 5.8: 700 Tonne rope with 24 subropes and simulated damage (10% of cross-section)

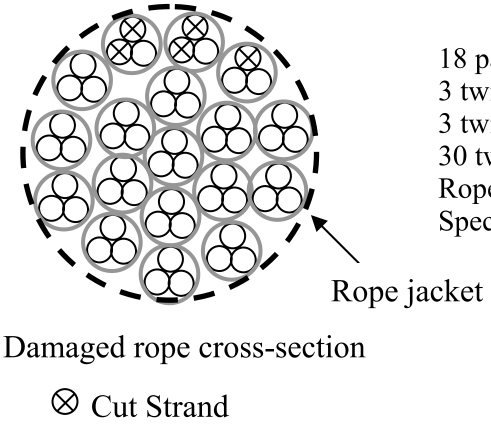

18 parallel unjacketed sub-ropes
3 twisted strands per sub-rope
3 twisted rope yarns per strand
30 twisted yarns per rope yarn
Rope diameter (*d*): 32 [mm]
Specified Breaking Strength: 35 tonnes (77.2 kips)

Fig. 5.9: 35 Tonne rope with 18 subropes and simulated damage (10% of cross-section)

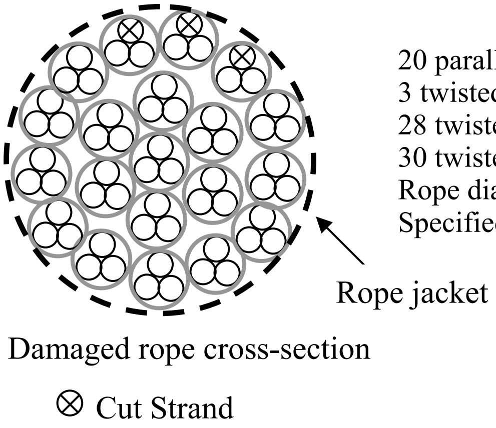

20 parallel unjacketed sub-ropes
3 twisted strands per sub-rope
28 twisted rope yarns per strand
30 twisted yarns per rope yarn
Rope diameter (*d*): 147 [mm]
Specified Breaking Strength: 700 tonnes (1543.2 kips)

Fig. 5.10: 700 Tonne rope with 20 subropes and simulated damage (5% of cross-section)

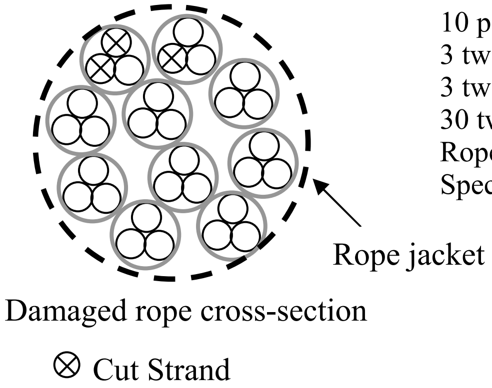

10 parallel unjacketed sub-ropes
3 twisted strands per sub-rope
3 twisted rope yarns per strand
30 twisted yarns per rope yarn
Rope diameter (*d*): 36 [mm]
Specified Breaking Strength: 35 tonnes (77.2 kips)

Fig. 5.11: 35 Tonne rope with 10 subropes and simulated damage (10% of cross-section)

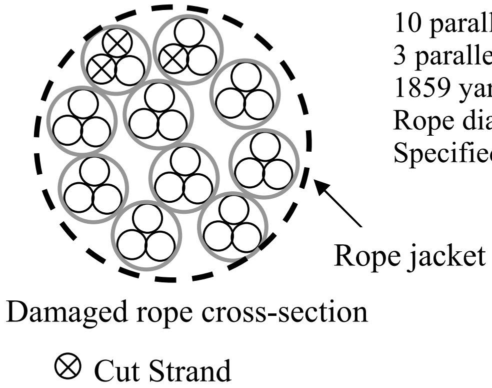

10 parallel unjacketed sub-ropes
3 parallel strands per sub-rope
1859 yarns per strand
Rope diameter (*d*): 166 [mm]
Specified Breaking Strength: 700 tonnes (1543.2 kips)

Fig. 5.12: 700 Tonne rope with 10 subropes and simulated damage (10% of cross-section)

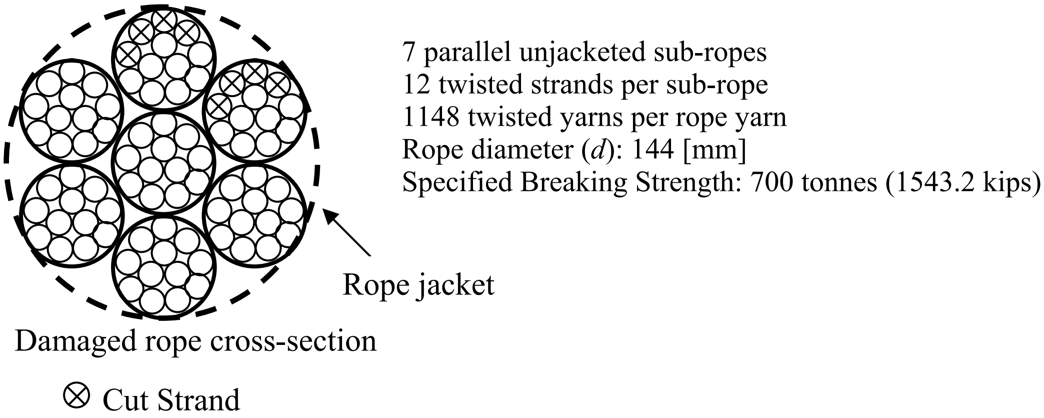

7 parallel unjacketed sub-ropes
12 twisted strands per sub-rope
1148 twisted yarns per rope yarn
Rope diameter (*d*): 144 [mm]
Specified Breaking Strength: 700 tonnes (1543.2 kips)

Fig. 5.13: 700 Tonne rope with 7 subropes and simulated damage (10% of cross-section)

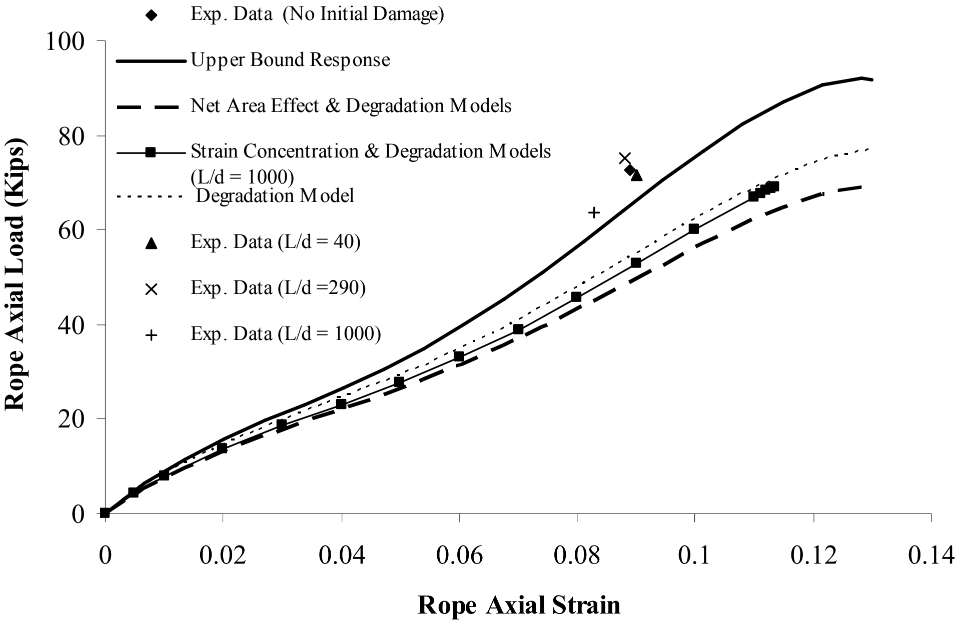

Fig. 5.14: Experimental data and predicted responses of Rope 1

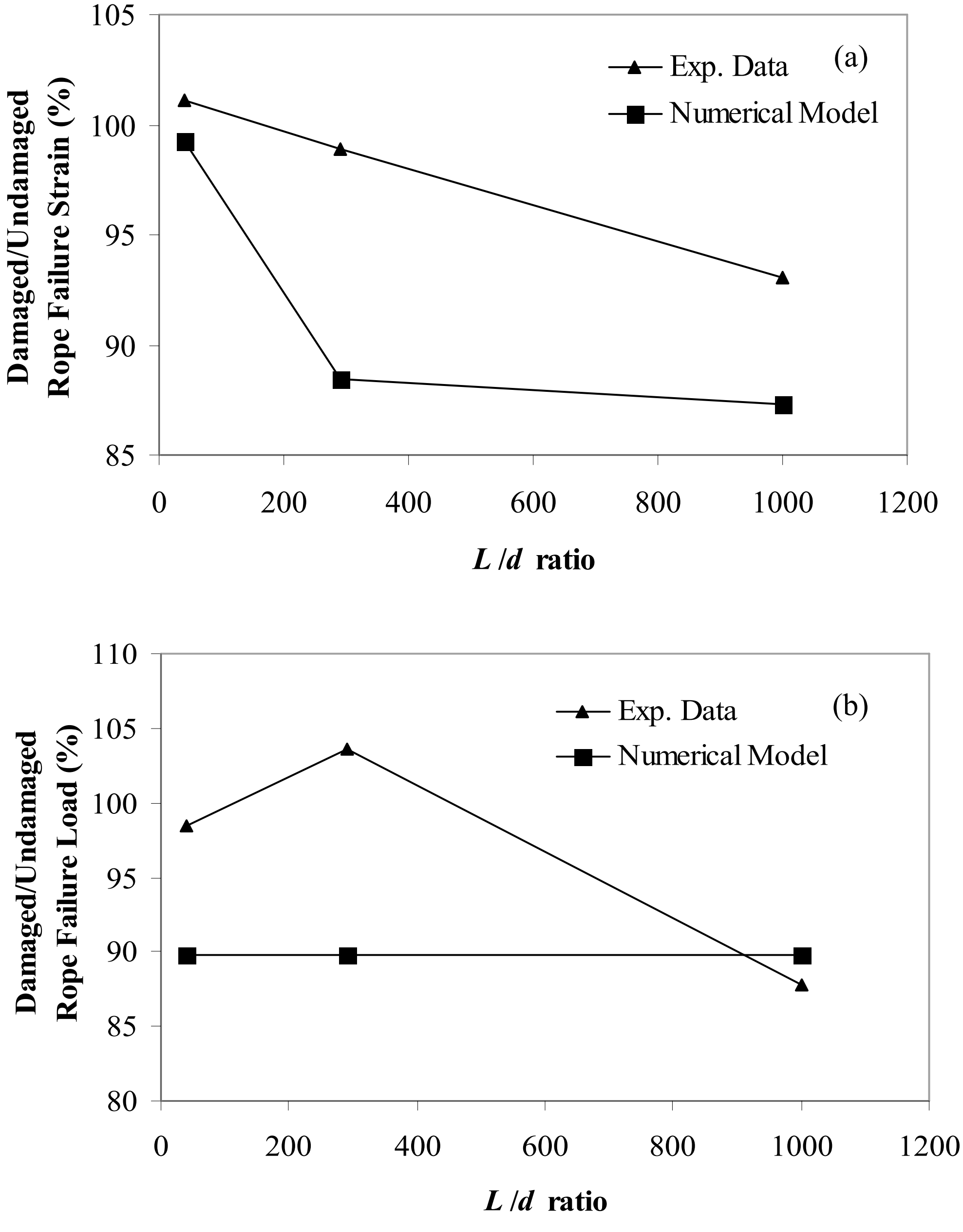

Fig. 5.15: Variation of the (a) residual failure strain and (b) residual strength of Rope 1 with respect to *L*/*d* ratio values

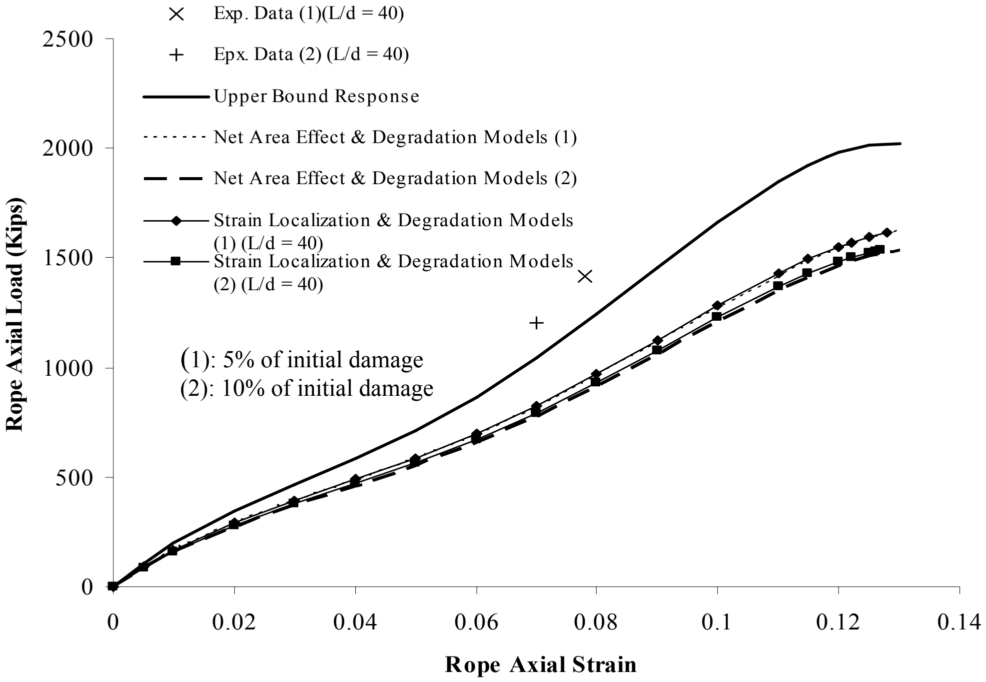

Fig. 5.16: Experimental data and predicted responses of Rope 2

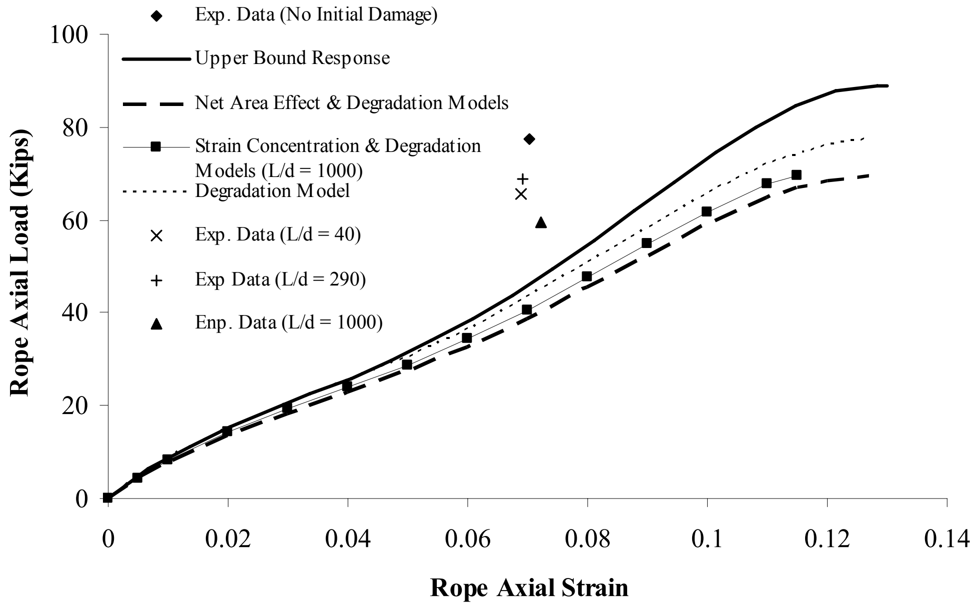

Fig. 5.17: Experimental data and predicted responses of Rope 3

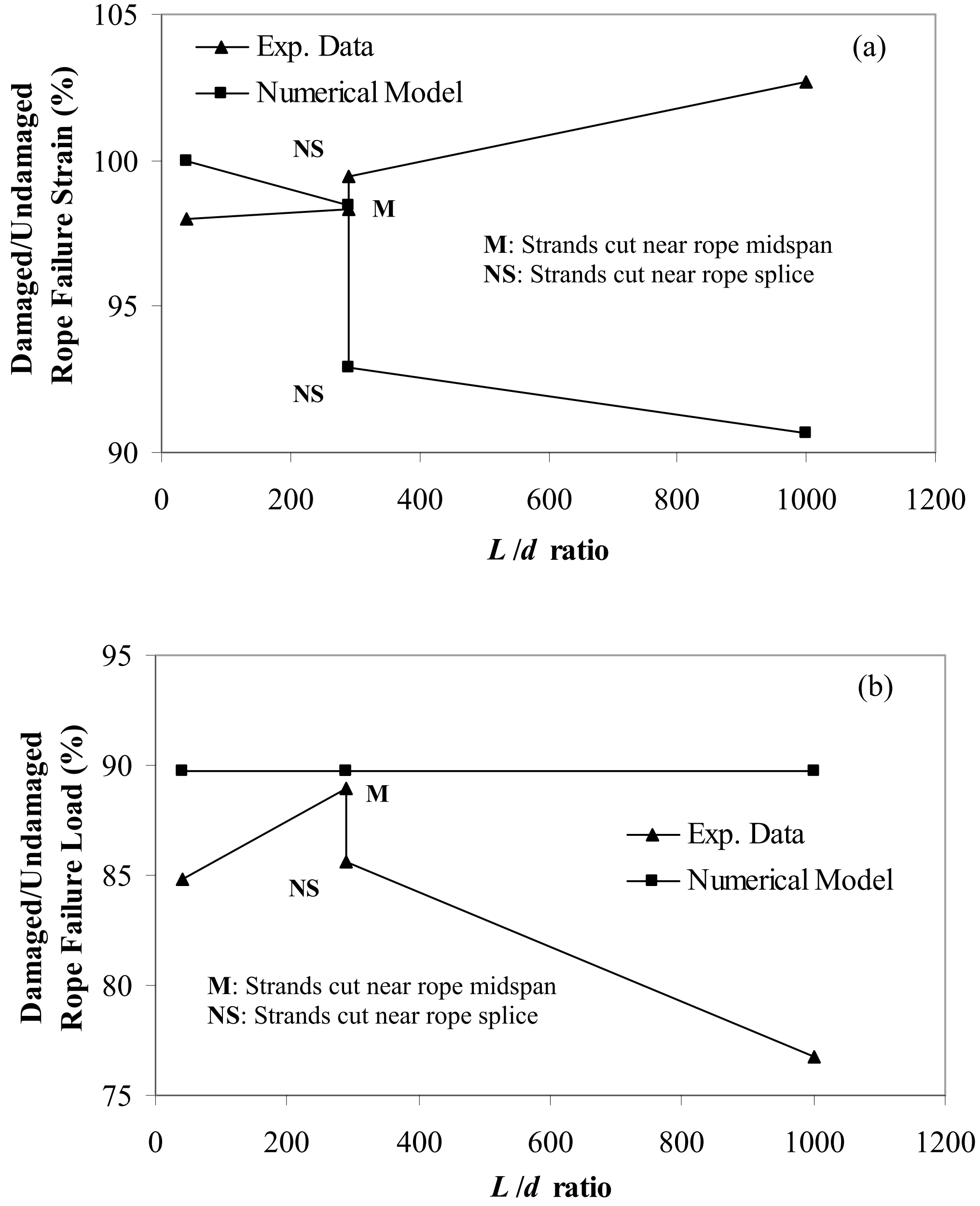

Fig. 5.18: Variation of the (a) residual failure strain and (b) residual strength of Rope 3 with respect to *L*/*d* ratio values

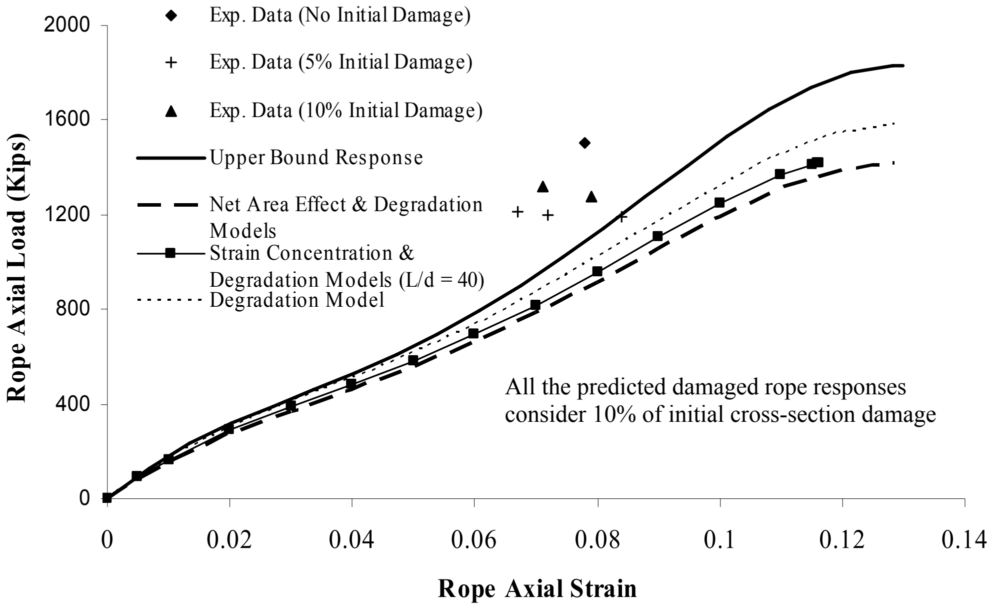

Fig. 5.19: Experimental data and predicted responses of Rope 4

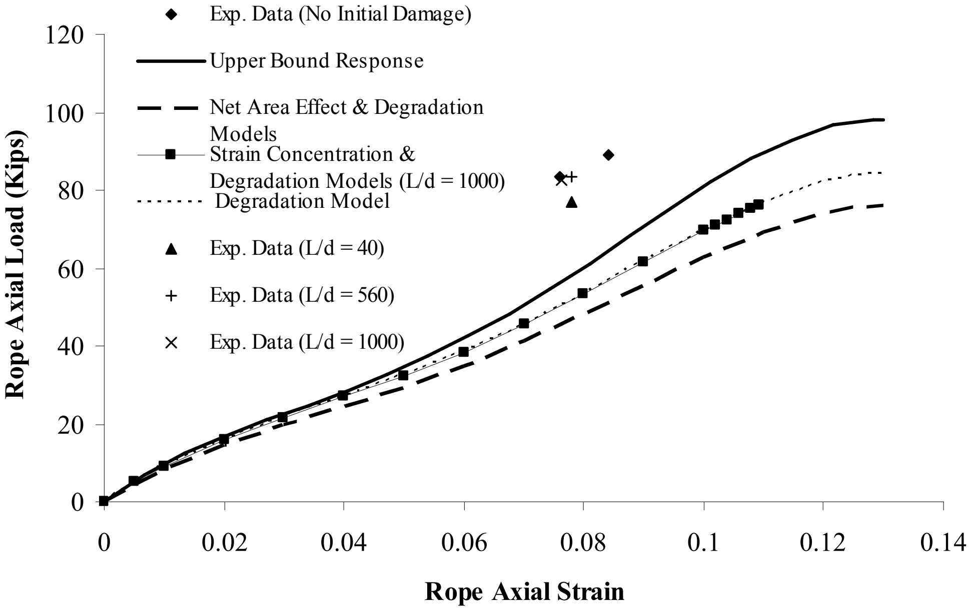

Fig. 5.20: Experimental data and predicted responses of Rope 5

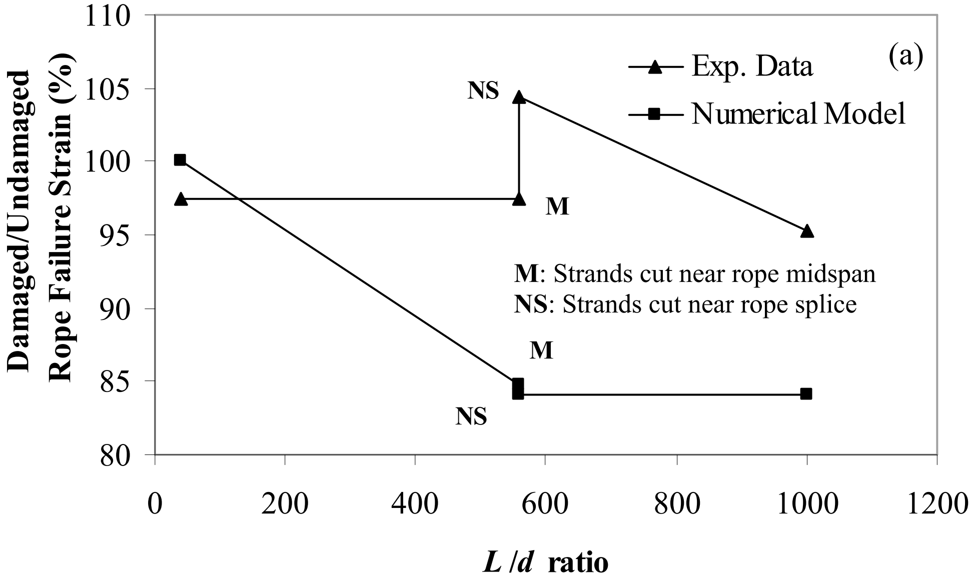

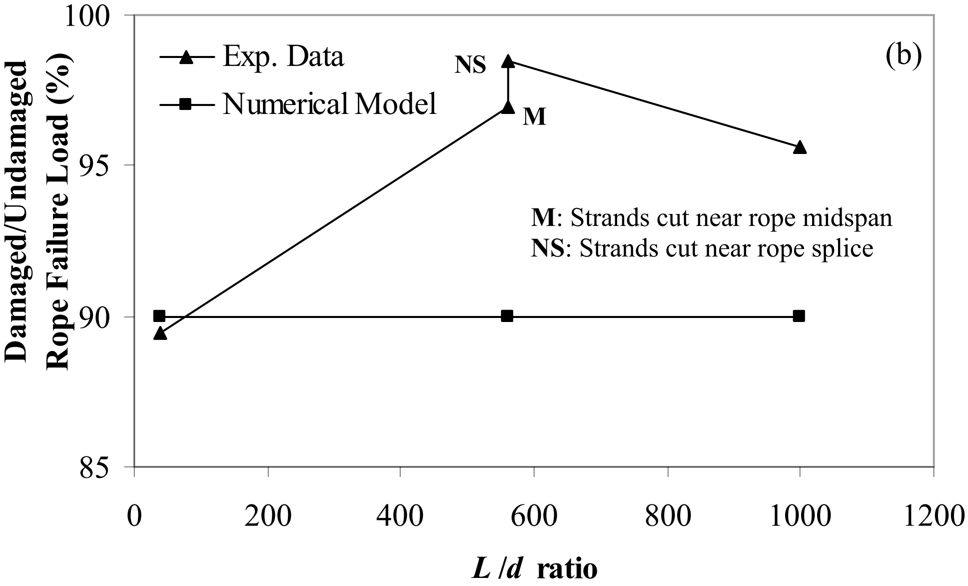

Fig. 5.21: Variation of (a) the residual failure strain and (b) residual strength of Rope 5 with respect to *L*/*d* ratio values

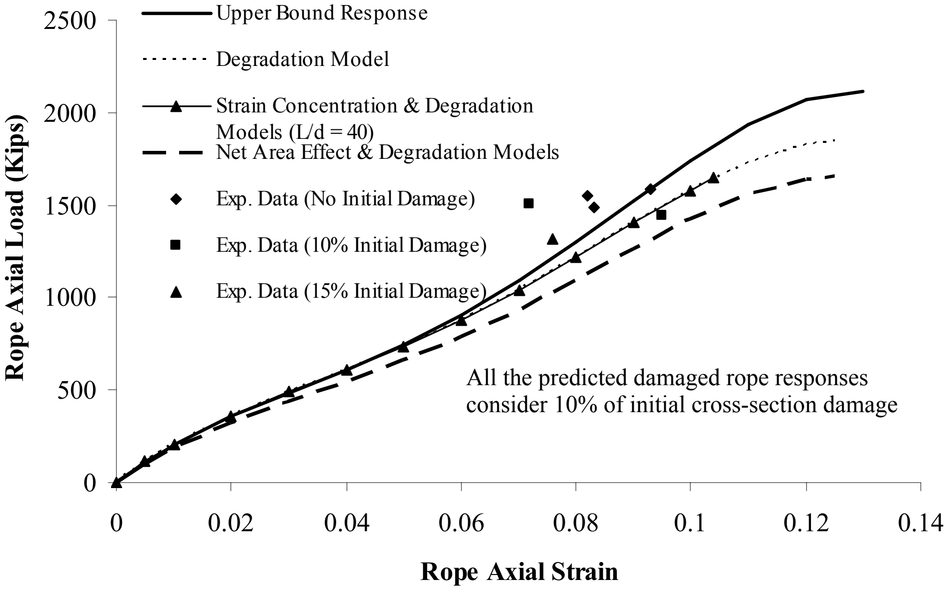

Fig. 5.22: Experimental data and predicted responses of Rope 6

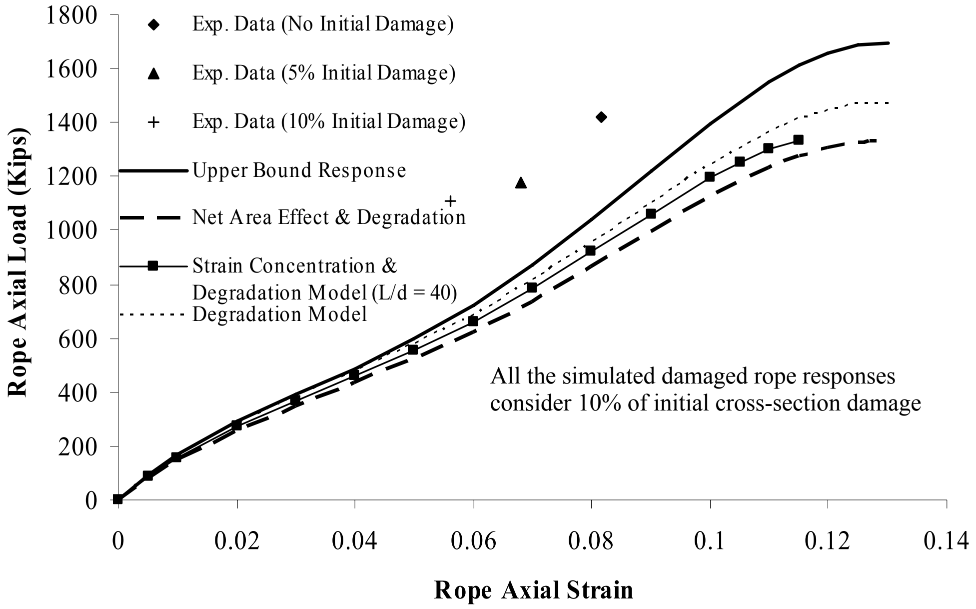

Fig. 5.23: Experimental data and predicted responses of Rope 7

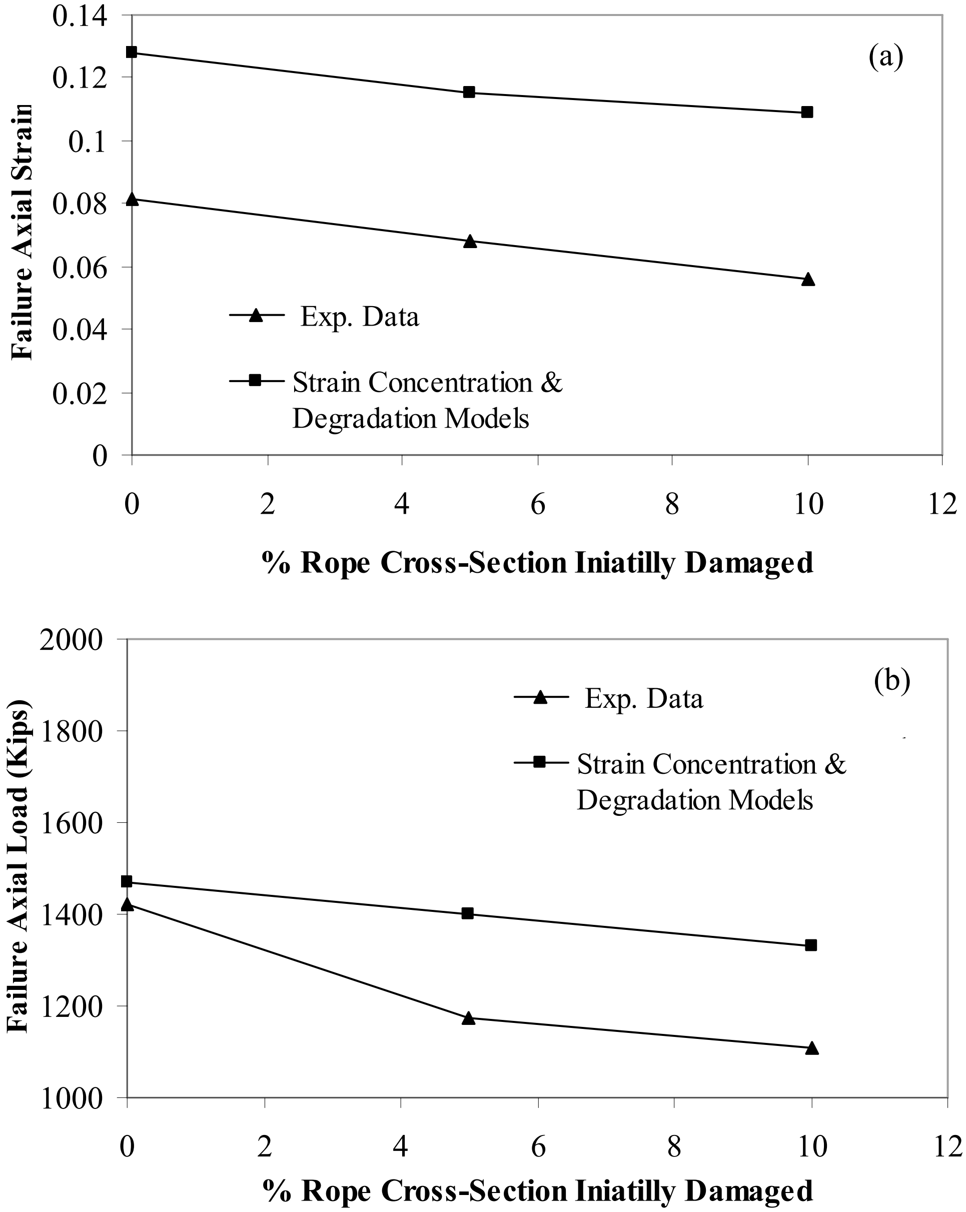

Fig. 5.24: Variation of the (a) failure axial strain and (b) residual axial strength of Rope 7 with respect to initial rope damage state

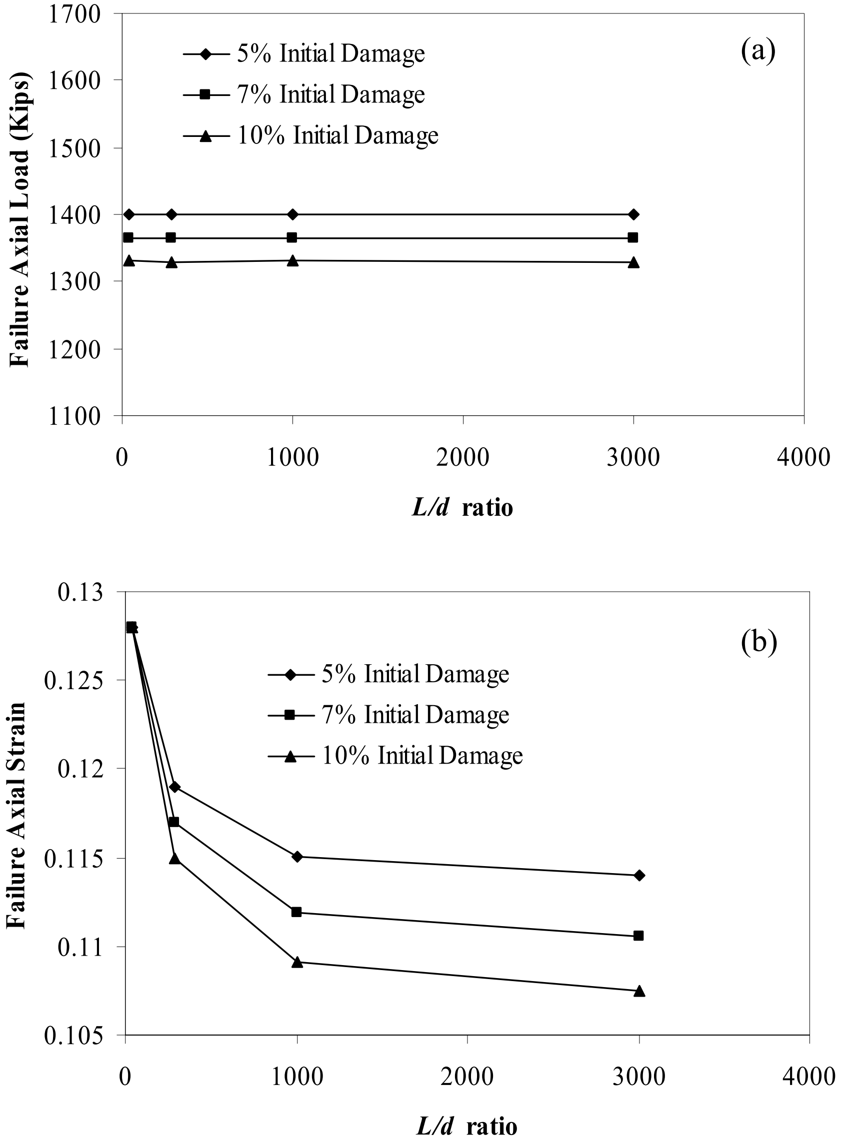

Fig. 5.25: Variation of the (a) failure axial load and (b) failure axial strain of Rope 7 with respect to L/*d* ratio for different initial rope damage states

The analyses suggest that the estimate of the breaking load (capacity) of initially undamaged ropes that is based upon the rope degradation model (Chapter 4) compares well with the experimental data (except for the rope response of Fig. 5.22 in which rope breaking load is overestimated by about 19%). A summary of the measured and predicted rope capacities shown in the previous graphs are summarized in Table 5.2. These results validate the calibration of the damage model using small-scale ropes as presented in Chapter 4.

Table 5.2 Summary of the initially undamaged rope capacities

Plot	**Max. Rope Capacity (Kips) Exp. Data**	**Max. Rope Capacity (Kips) Numerical Model (Predicted)**	**Predicted/Exp. Data Value**
Fig. 5.14	72.61	76.91	1.06
Fig. 5.17	77.49	77.29	0.997
Fig. 5.19	1503.13	1581.18	1.052
Fig. 5.20	86.22	84.45	0.979
Fig. 5.22	1542.86	1842.38	1.19
Fig. 5.23	1422.57	1469.93	1.033

The plots previously mentioned also suggest that the damaged rope response curve is bounded by the model that ignores degradation of rope properties (upper bound) and by the curve obtained through the use of the net area effect model (lower bound). If the length over which damage propagates along the rope ("damage length") approaches that of the rope length, the damaged rope response approaches its lower bound. Conversely, if the damage length is small compared to the rope length, the damaged rope response approaches its upper bound. This last observation is due to the fact that the value of the recovery length is a small percentage of the rope length, so the rope response is only slightly reduced relative to the undamaged case. As the damage length increases and broken rope elements develop admissible values for their recovery lengths, the strains along the rope are non-uniform, generating a strain localization region around the failure location. Based on the damage (deterioration) model, damage localization occurs as well. This damage localization causes the premature failure of rope elements and reduces the damaged rope breaking strength and maximum attainable deformation.

The predicted response of a damaged rope, including the strain localization effect, depends on the estimate of the “damage length”. This length, computed based on the recovery length of broken rope elements, depends only on the rope cross-section model and not on the rope length. Consequently, as the damaged rope length increases (with the length over which damage occurs remaining constant), the damaged rope response gets stiffer (approaching its upper bound curve), the rope strain at failure for the damaged rope decreases, and the damaged rope strength is not noticeably affected.

In the analyses presented in Section 5.4, the predicted damaged rope responses are compared with experimental data when they are available. Not only are the values of the maximum deformation and capacity compared, their dependence on the *L*/*d* ratios and percentages of the initial damage are also provided. With the exception of the rope response shown in Fig. 5.6, the experimental data plot above the theoretical upper bound rope response curve, which is the stiffest rope response that the numerical model can provide using the material properties that were established previously from the small-scale rope tests. The predicted rope axial failure strain overestimates the experimental value for all cases studied, except for the predicted rope response shown in Fig. 5.6. For the numerical model, the predicted value of axial failure strain decreases in a nonlinear fashion as the *L*/*d* ratio increases. Conversely, the experimental values do not show a clear trend that depends upon the *L/d* ratio. In fact, for some ropes (Rope 1 and Rope 5), the experimental values of the axial failure strain decrease as the *L/d* ratio increases, while for others (Rope 3), the axial failure strain increases with increasing *L/d* ratio.

In Tables 5.3 and 5.4, the predicted and experimental values of the axial load capacity for damaged ropes with specified breaking strengths (for the undamaged case) equal to 35 Tonnes (77.2 Kips) and 700 Tonnes (1543.2 Kips), respectively, are presented. The tables provide different values of the strength as a function of the *L*/*d* ratio for a 10% initial damage state. For the case of ropes with specified undamaged breaking strengths equal to 35 Tonnes, the maximum load capacities of Rope 1 and Rope 3 are accurately predicted by the numerical model (within a range of ± 5% of the experimental values) for values of *L*/*d* equal to 40 and 290. For these ropes, the experimental data show that the load capacity decreases as the value of *L*/*d* increases from 290 to 1000. This aspect of behavior is not captured by the numerical model (Figs. 5.15 and 5.18). With the numerical model, the values of the predicted rope capacities do not show a strong dependence on the *L/d* ratio. For Rope 5, the predicted maximum load capacity correlates well with the experimental data for a value of *L*/*d* equal to 40. For greater values of *L*/*d*, the maximum load capacity of the rope increases, but it remains nearly constant for values of *L*/*d* equal to 560 and 1000 (Fig. 5.21).

For ropes with specified breaking strengths equal to 700 Tonnes, the numerical model overestimates the measured damaged rope capacities for all the cases studied. Based on the experimental data, the damaged capacity of some ropes (Ropes 2, 4, and 6) shows some dependence on the *L*/*d* ratio (i.e., their load capacities decrease as the value of *L*/*d* increases). However, such is not the case for Rope 7, whose load capacity remains nearly constant for values of *L*/*d* equal to 40 and 290. As in the case of ropes with specified breaking strengths equal to 35 Tonnes, the predicted rope capacities obtained by the numerical model for the 700-Tonne ropes do not show a strong dependence on the *L*/*d* ratio.

In Fig. 5.24, the variation of the failure axial load and failure axial strain with respect to initial loss of rope cross-sectional area (0%, 5%, and 10%) of Rope 7 is presented. The predicted values overestimate the measured data for all cases studied. However, both the experimental and the predicted values for these quantities show the same trend: as the initial loss of rope cross-sectional area increases, both parameters decrease. Fig. 5.25 shows the predicted damaged rope capacities and failure axial strains for each initial damage state considered as a function of the *L*/*d* ratio. The predicted rope capacities do not show a strong dependence on the *L/d* ratio. Conversely, the failure axial strains decrease, showing a decreasing rate of change, as the *L*/*d* ratios increase.

Eventually, the predicted failure axial strains reach a minimum value for large values of the *L*/*d* ratio.

Table 5.3 Summary of damaged ropes capacities (10% of initial damage) with Specified Breaking Strength equal to 35 Tonnes (77.2 Kips)

Plot	Max. Rope Capacity (Kips) Exp. Data				Max. Rope Capacity (Kips) Numerical Model (Predicted)
	L*/*d	***L*/*d***	***L*/*d***	***L*/*d***	
	40	290	560	1000	
5.14	71.49	72.61		63.70	69.11
5.17	65.75	68.95		59.49	69.39
5.20	77.12		83.61	82.44	76.02

Table 5.4 Summary of damaged ropes capacities with Specified Breaking Strength equal to 700 Tonnes (1543.2 Kips)

Plot	Initial Damage	Max. Rope Capacity (Kips) Exp. Data		Max. Rope Capacity (Kips) Numerical Model (Predicted)
		L*/*d	***L*/*d***	
		40	290	
5.16	10%	1201.51	945.78	1536.95
5.19	10%	1296.31	994.28	1415.60
5.22	15%	1315.52	1101.41	1562.55
5.23	10%	1146.40	1111.13	1329.77

5.5 SUMMARY

In this chapter, a numerical model to account for the effect of broken rope elements on overall rope response is presented. This model relies on the ability of a broken rope element to pick up its proportionate share of axial load over a distance measured from the failure region. This distance is defined as the recovery length.

Numerical simulations were compared with experimental data obtained from static capacity tests on different types of rope constructions with varying amounts of initial damage. For the case of initially undamaged ropes, the proposed numerical model accurately predicted maximum load capacity, except for the case of Rope 6 (Fig. 5.22), whose load capacity was overestimated by approximately 19%. For the case of initially damaged ropes, the proposed numerical model did a good job predicting the capacity of the ropes with specified undamaged breaking strengths equal to 35 Tonnes, but it overestimated the capacity of the ropes with specified undamaged breaking strengths equal to 700 Tonnes. For these larger ropes, which contain significantly greater numbers of fibers than the smaller ropes, it is believed that variability in the material properties contributes to the error in the predictions. In addition, parameters used in the analyses were selected from test data on very small ropes. These ropes had a capacity that is only 0.3% of the capacity of the full-scale ropes. As such, small errors in testing and parameter selection can become magnified when results are extrapolated to specimens that are very large. Finally, lack of symmetry in the cross-section becomes more important as the rope size increases. Because the contribution to twisting by elements on the exterior of a large diameter rope is greater than it would be for a similarly sized component in a smaller diameter rope (due to the increased lever arm distance), cut components on the perimeter of a 700-Tonne rope can have a greater influence on the overall rope response than cut components on a 35-Tonne rope. It is believed that this aspect of behavior must be accounted for more accurately in the computational model. For all of the cases analyzed, the proposed numerical model overestimated the rope axial failure strains.

A detailed study was presented for the effect of the L/d ratio on the residual strength and residual maximum axial strain of damaged ropes. These two residual quantities were characterized as the ratio of the damaged to undamaged value of each parameter and were compared with the ones obtained from the experimental data. The numerical predictions of these two residual quantities showed a unique trend in their dependence on the *L*/*d* ratio: as the value of the *L*/*d* ratio increased, the value of residual maximum axial strain decreased, and the value of the residual strength remained nearly constant. The experimental data, however, did not show a clear trend. For some rope constructions, as the *L*/*d* ratio increased, the value of the residual maximum axial strain decreased, while for other ropes the maximum axial strain increased. In the case of the residual strength, as the *L/d* ratio increased for some ropes, the value of the residual strength decreased. The reduction was particularly significant for three of the four 700-Tonne ropes tested, and a recoil damage mechanism (which is not included in the computational model) was suggested as the cause (Ward, et al., 2006a). For other ropes, however, the residual strength remained nearly constant as a function of *L/d* ratio. Thus, because the ropes tested showed great variability in their response, more data are needed to validate observed trends in the behavior of damaged ropes. While the current model can be used to obtain reasonable estimates of rope response, improvements are still needed before it can be reliably used for detailed design calculations.

Most of the experimental data, including that for both the damaged and the undamaged ropes, plotted above the theoretical upper bound, which is the stiffest rope response expected. Some of the possible reasons for this inconsistency are the following: measurement error of some rope variables, variability in the rope properties used as input in the computational model, or a combination of these effects. As stated above, the numerical model overestimates the rope failure axial strain and accurately predicts the capacity of the damaged ropes with specified undamaged breaking strengths equal to 35 Tonnes. Thus, errors could have been made in computing the rope failure axial strains from the information obtained from the tests. More detailed information about the experimental data are needed to understand how rope strength capacities and rope failure strains were measured. For example, it is not clear which “gage length” was used when reporting rope failure axial strains and whether or not the entire rope length or some reduced length was utilized in the calculations. From the information provided on the testing program (Ward, et al., 2006(a)), it is clear that the actual strain was not in fact measured. Strain was inferred from movement of the cross-head on the loading assembly. In addition, because the rotation was not measured, it is difficult to know precisely how much of the overall rope response was from the actual stretching of the fibers. While observations may suggest that most of the measurement can be directly attributed to strain, small errors can have a noticeable impact on the computational model given the slope of the load-deformation curve near the onset of failure. Thus, even if the reported strain is only slightly different from the "actual" strain, it needs to be accounted for as a source of error in the computational model.

As indicated above, because the numerical model relies on accurate measurements of rope rotation (i.e., twist), these data are needed for properly defining the boundary conditions used for analysis. Aside from the potential sources of error associated with measurement of the variables used by the computational model, variability of rope properties may be playing an important role in the differences noted between the predicted and the measured rope behavior. Variations in the stress-strain relationships and values of the breaking loads and breaking strains of the rope elements play a significant role in the computational model. Thus, possible extensions to the model include treatment of variability in rope properties and a lack of symmetry of the cross-section.

CHAPTER 6
Summary and Conclusions

6.1 SUMMARY AND CONCLUSIONS

To study the behavior of synthetic-fiber ropes under a variety of loading conditions, a computational model was proposed that accounts for the change in structural properties and configurations of a virgin (i.e., undamaged) or initially damaged rope. The developed model includes both geometric and material nonlinearities, and it incorporates a damage index so that the strength and stiffness degradation of the rope elements throughout the loading history can be modeled. The proposed model also considers the capability of a broken rope element to keep contributing to rope response after fully developing its recovery length.

The computational model developed under this research relies on the displacement control method, and integration over the rope element cross-section is carried out numerically using Gaussian quadrature. The assumption of geometry preservation is employed to establish the kinematics of deformation for rope elements. Thus, helical components are assumed to remain helical following the application of load. Geometric nonlinearity is taken into account by using nonlinear strain/displacement equations for each rope element in terms of the global strain/displacement quantities of the rope. Rope geometry is updated at every load step. The nonlinear material behavior of synthetic-fibers is considered by using a polynomial representation (up to the fifth degree) of the normal and shear stresses in terms of their respective strain quantities. The extreme cases of real rope cross-sectional geometry are considered in the computational model development through packing and wedging geometry representations. The set of linearized differential equilibrium equations is reduced to a system of linear algebraic equations of order two using the assumptions related to the kinematics of deformation of rope elements.

As mentioned above, the effects of strength and stiffness degradation are modeled by means of a damage index *D*. The damage index is described by a linear combination of three processes: maximum deformation, work done by frictional forces, and the stress range experienced by a rope element. Each of these processes could have a nonlinear dependence on the damage variables used to quantify them. The proposed damage model that represents the evolution of the damage index throughout the load history was calibrated based on available experimental data. When the value of damage index equals one (i.e., $D = 1$), the damage length associated with the failed rope element is computed based on the estimate of its recovery length. If the value of this damage length is greater than the rope length, the failed rope element is assumed to no longer contribute to the total response of the rope. Conversely, if the value of the damage length is admissible, the failed rope element is assumed to contribute to rope response after fully developing its recovery length value. If such is the case, the rope is discretized into "sub-rope" elements based on the value of the recovery lengths computed. Each "sub-rope" is modeled as a two-noded axial-torsional element with two degrees of freedom at each node: axial displacement and axial rotation. This model captures the effect of having a weakened cross-section acting over a localized region defined by the recovery length. Strains are not uniformly distributed along the rope length, resulting in a potential strain localization region around the failure site, and, based on the damage model, damage localization may also occur. Any lack of symmetry in the rope cross-section due to the failure of rope elements is neglected.

Using the computational model developed under this research, several rope geometries were studied. Virgin (i.e., undamaged) ropes and initially damaged ropes were considered. In most cases, experimental data for a monotonically increasing load were available for comparison with the analytical predictions. The first example studied was a one-level, two-layer polyester rope. This study was employed to calibrate the damage model proposed by comparing the experimental data curve with the simulation curve without any source of damage. A parametric study of the damage model was carried out to study the effects of changes in the damage parameters on the damage evolution (and consequently on rope response). The analysis results demonstrated that the proposed exponential evolution of the damage index agrees well with the experimental data.

One drawback with the above damage model was that polyester rope elements experienced low levels of damage near the onset of failure (i.e., values much less than one). As previously mentioned, the failure of a rope element occurs when the damage index equals one, and there is a need to capture the rapid change in the damage index corresponding to the response just prior to component rupture. Accordingly, a perturbation method was used because it allowed for the degradation of rope properties to be represented as a continuous process. To verify the validity of the proposed damage model, two different types of analysis were carried out on small ropes: (1) analysis of a two-level, one-layer polyester rope, and (2) analyses of one-level, one-layer polyester ropes with one and three rope elements initially damaged, in which the failed components were assumed to not contribute to total rope response (net area effect model). Computed results showed that for the case of the two-level, one-layer polyester rope, the simulation curve overestimated by 6% the maximum rope capacity and by 1.5% the corresponding strain. For the case of the one-level, one-layer polyester rope with one rope element initially damaged (D = 1), the simulation curve overestimated by 2% the maximum capacity of the rope and by less than 1% the corresponding strain. Finally, for the case of the one-level, one-layer polyester rope with three rope elements initially damaged (D = 1), the simulation curve overestimated by 1% the maximum capacity of the rope and by less than 1% the corresponding strain.

The same two-level, one-layer polyester rope mentioned above was used to study the effect of failed rope elements on overall rope response. For this purpose, two models were used to predict the damaged rope response: the net area effect and degradation model and the strain localization and degradation model. Nine of the twenty seven rope elements (33% of the rope cross-section) were cut prior loading. The model with strain localization effects resulted in a stiffer rope response that corresponded better with experimental data and provided a smaller value of the rope breaking strain relative to the net area effect model. Both of these models, however, gave values of rope breaking strain and rope breaking load that were smaller than those indicated by the test data.

The proposed damaged model was also verified with the analyses of large-scale virgin and initially damaged polyester-jacketed ropes. Most of the studies considered a

10% loss of cross-sectional area for the initial damage state. Experimental data for ropes with a specified breaking strength (SBS) of 35 Tonnes and 700 Tonnes were available. For analysis purposes, all of these ropes were modeled as two-level ropes. At the first level, all ropes had parallel, unjacketed sub-rope constructions. Each sub-rope comprising the second level was built by twisting a specified number of strands together. Ropes with SBS values of 35 Tonnes were constructed by different rope manufacturers using the following configurations: 24 sub-ropes and 3 strands per sub-rope; 18 sub-ropes and 3 strands per sub-rope; and 10 sub-ropes and 3 strands per sub-rope. For the case of ropes with SBS values of 700 Tonnes, manufactured configurations included the following: 24 sub-ropes and 3 strands per sub-rope; 20 sub-ropes and 3 strands per sub-rope; 10 sub-ropes and 3 strands per sub-rope; and 7 sub-ropes and 12 strands per sub-rope. In addition, for ropes with SBS values of 35 Tonnes and 700 Tonnes, parametric studies were conducted to evaluate the effect of different *L*/*d* ratios (rope length normalized by rope diameter) on damaged rope response. The effects of different initial damage states (varied from 0% to 15% of rope cross-section) on the values of the rope breaking strain and rope breaking load were studied for ropes with SBS values of 700 Tonnes. .

Computed results showed that for the case of initially undamaged ropes, the simulation values of the rope breaking axial load compared well with experimental data, within a range of -2% to 6%, except for Rope 6 (see Chapter 5 for a description of the individual ropes) whose breaking axial load was overestimated by approximately 19%. The simulation values of rope breaking strain, however, overestimated the experimental data values for all cases studied. For the analysis of initially damaged polyester-jacketed ropes, the confinement effect of the jacket on rope elements was considered to determine if the broken rope elements contributed to rope response after fully developing their recovery length. For modeling purposes, the rope jacket was considered as a thin-walled tube having an axial capacity equal to 3% of the axial capacity of the corresponding initially undamaged rope. The predicted rope axial failure strain overestimated the experimental values for all cases studied. For the numerical model that included degradation and strain localization effects, the predicted value of axial failure strain decreased in a nonlinear fashion as the *L*/*d* ratio increased. Conversely, the experimental values did not show a clear trend that depended upon the *L/d* ratio. In fact, for some ropes, the experimental values of the axial failure strain decreased as the *L/d* ratio increased, while for others, the axial failure strain increased with increasing *L/d* ratio.

Considering the maximum damaged rope capacity, for some rope constructions with values of *L/d* ratio smaller than 290, the numerical model provided accurate predictions of response (within a range of ± 5% of the experimental values) for ropes with SBS values of 35 Tonnes. For these ropes, the test data showed that their load capacities decreased as the value of *L*/*d* increased from 290 to 1000. This aspect of behavior was not captured by the numerical model. In fact, the rope capacities predicted by the numerical model showed very little dependence on the *L/d* ratio. For the case of Rope 5, the predicted maximum load capacity correlated well with the experimental data for a value of *L*/*d* equal to 40. For greater values of *L*/*d*, the experimental data showed that the maximum load capacity of the rope increased, but, unlike some of the other ropes, it remained nearly constant for values of *L*/*d* equal to 560 and 1000 (10% greater than the value predicted by the numerical model).

For the case of ropes with SBS values of 700 Tonnes, the numerical model overestimated the damaged rope capacity for all the rope constructions considered. For some of these ropes (Rope 2, Rope 4 and Rope 6), the test data showed that their load capacities decreased as the value of *L*/*d* increased from 40 to 290. As in the case of the analyses of ropes with SBS values of 35 Tonnes, the numerical model did not capture this behavior. For the case of Rope 7, however, the maximum load capacity of the rope remained nearly constant for values of *L*/*d* equal to 40 and 290 (overestimated by 15% by the numerical model).

As previously mentioned, the effect of initial damage states (0%, 5%, and 10% of the rope cross-section) on the values of the rope breaking strain and rope breaking load was studied for a rope with an SBS value of 700 Tonnes (Rope 7). Although the experimental values of rope breaking strain and rope breaking load were overestimated by the numerical model, both experimental and predicted values for these quantities showed the same trend: as the initial loss of rope cross-sectional area increased, both parameters decreased. In addition, for each damage state, the dependence of the breaking axial strain and breaking axial load on the *L/d* ratio of the rope was studied. The rope capacities predicted by the numerical model showed very little dependence on the *L/d* ratio and the predicted value of the breaking axial strains decreased in a nonlinear fashion as the *L/d* ratio increased, converging asymptotically to a minimum value.

6.2 FUTURE STUDIES

The findings reported in this research are intended to demonstrate the need for having computational tools that accurately predict the response of damaged ropes in order to interpret and extend test data and to develop design guidelines. While this research represents an advancement over previous approaches to analyzing damage rope response, many aspects of this study can be modified or extended to improve the accuracy with which damaged rope response is computed. The following recommendations are given for further research on this topic:

1. *Experimental studies on bigger ropes to gain a better understanding of response under increasing monotonic load* – Information obtained from these studies can be used to verify or eventually modify the current damage model, the methods used to obtain damage evolution, and the assumptions made to simulate softening behavior. In addition, new issues that can affect rope behavior can be studied, including the following: rope diameter-rope length ratio, initial partially or fully damaged rope elements, non-symmetry in the cross-section, and variation in the arrangement of rope elements and rope splices.
2. *Incorporation of more accurate material models* – The current constitutive model ignores time-dependent behavior and approximates the known viscoealstic response of synthetic fibers through the use of an empirically fit fifth-order polynomial function. Thus, this approximate constitutive model can be extended to consider intrinsic viscoelastic behavior of synthetic fibers. A general nonlinear viscoelastic model can be developed that allows studying long-term behavior of synthetic ropes. In addition, a

new term to the damage model can be added that considers creep or relaxation failure.

3. *Evaluation and quantification of the effects of broken rope elements on rope response* – A new feature to the computational model can be added that considers the loss of symmetry and remaining strength in a rope due to the failure of rope elements.
4. *Verification of the assumptions made to develop the current computational model using three-dimensional finite element analyses*

APPENDIX

Softening Behavior Modeling

The analysis presented in this appendix is to demonstrate the validity of using just a one-term composite expansion to solve Eqs. (4.12) and (4.13) by the perturbation method technique. The two-term composite expansion of Eq. (4.12), including a non-zero value of the initial damage D_I, has the following form:

$$D(\eta) = D_I + \alpha_1 \eta^{\beta_1} + (1 - \alpha_1 \eta_u^{\beta_1} - D_I) e^{\frac{\eta - \eta_u}{\theta_1}} + \theta_1 (\alpha_1 \beta_1 \eta^{\beta_1 - 1} - \alpha_1 \beta_1 \eta_u^{\beta_1 - 1} e^{\frac{\eta - \eta_u}{\theta_1}}) \qquad \text{(A.1)}$$

and the two-term composite expansion of Eq. (4.13) including a non-zero value of the initial damage D_I has the following form:

$$D(\eta) = D_I + \omega_1 \eta + \omega_2 \eta^2 + \omega_3 \eta^3 + \left[1 - (D_I + \omega_1 \eta_u + \omega_2 \eta_u^2 + \omega_3 \eta_u^3)\right] e^{\frac{\eta - \eta_u}{\theta_2}} +$$

$$\theta_2 \left[2\omega_2 \eta + 3\omega_3 \eta^2 - (2\omega_2 \eta_u + 3\omega_3 \eta_u^2) e^{\frac{\eta - \eta_u}{\theta_2}} \right] \qquad \text{(A.2)}$$

where θ_1 and θ_2 are constants much smaller than 1 ($\theta_1, \theta_2 \ll 1$) determined by Eq. (4.18), and η is a dimensionless variable defined as $(\varepsilon - \varepsilon_t)/\varepsilon_b$. The Eqs. (A.1) and (A.2) are an extension of the one-term composite expansions given by Eqs. (4.16) and (4.17), respectively.

In Figs. A.1 and A.2, the evolution of the damage index $D(\eta)$ considering a power law and polynomial variation of their leading term, along with the damage parameters used, are presented. These curves were computed considering one-term and two-term composite expansions in order to evaluate the additional information (if there is any) gained by performing a two-term composite expansion.

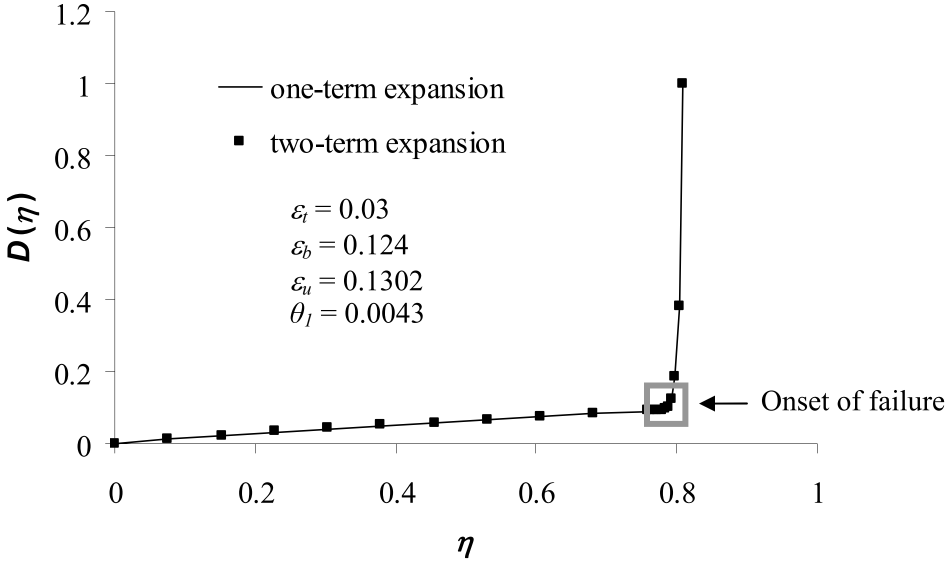

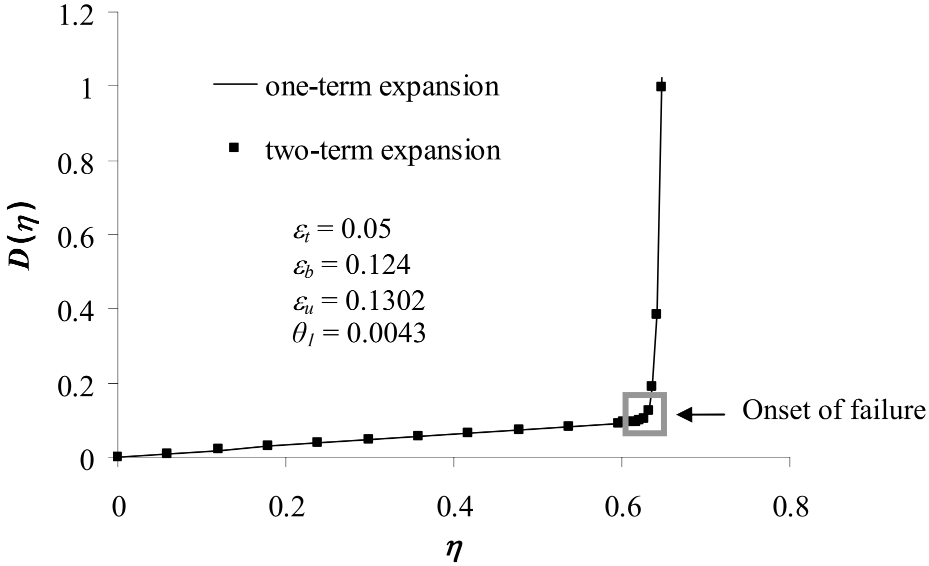

Fig. A.1 Power law evolution of the damage index

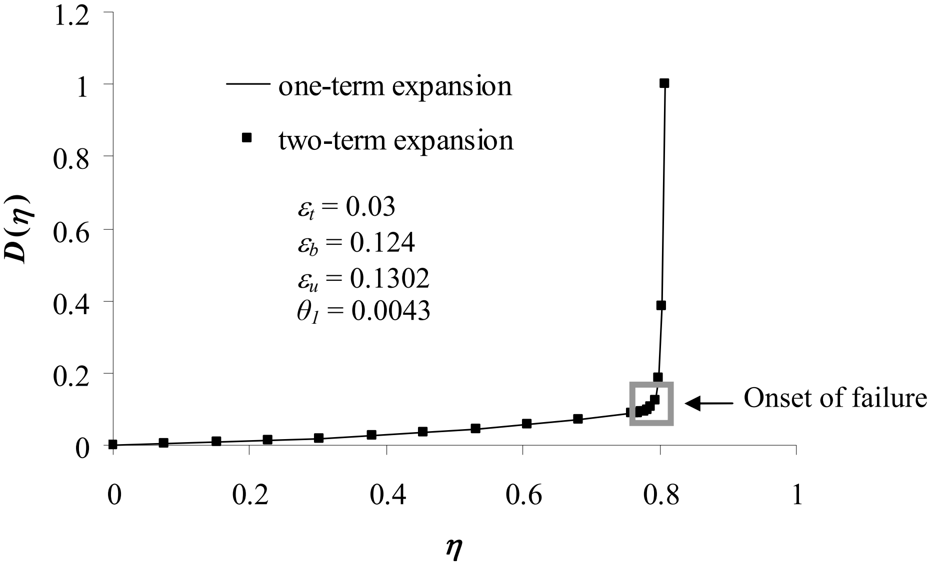

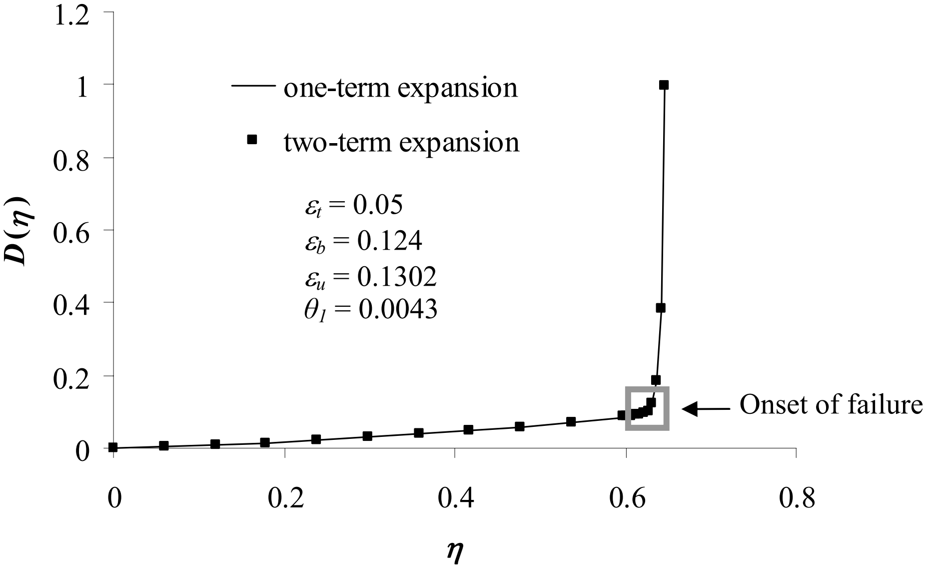

Fig. A.2 Polynomial evolution of the damage index

As can be seen in Figs. A.1 and A.2, for both damage models considered, a two-term composite expansion agrees quite closely with the results obtained from the one-term composite expansion. In addition, for each damage model, both composite expansions predict the same level of damage at the onset of failure of the rope elements.

REFERENCES

1. Banfield, S. and Casey, N., 1998, “Evaluation of Fibre Rope Properties for Offshore Mooring,” Ocean Engineering, Vol. 25, No 10, pp. 861-879.
2. Banfield, S., Hearle, J.W.S., Leech, C.M. and Lawrence, C.A., 2001, “Fibre Rope Modeller: A Cad Program for the Performance Prediction of advanced Cords and Ropes Under Complex Loading Environments,” Techtextil.
3. Bartle, R. and Sherbert, D., 1982, Introduction to Real Analysis, John Wiley & Sons Inc., New York, USA.
4. Beltran, J. F., Rungamornrat, J. and Williamson, E. B., 2003, “Computational Model for the Analysis of Damaged Ropes,” 13th International Offshore and Polar Engineering. Conference, Honolulu, Hawaii, USA., pp. 705-710.
5. Beltran, J.F. and Williamson, E.B., 2004, “Investigation of the Damage-Dependent Response of Mooring Ropes,” 14th International. Offshore and Polar Engineering. Conference, Toulon, France.
6. Beltran, J.F. and Williamson, E.B., 2005, “Degradation of Rope Properties Under Increasing Monotonic Load,” Ocean Engineering, Vol. 32, pp. 823-844.
7. Beltran, J.F. and Williamson, E.B., 2005, “Numerical Simulation of Damage Localization in Synthetic-Fiber Mooring Ropes,” 4th International Conference on Composite Materials for Offshore Operations, Houston, Texas, USA.
8. Blouin, F. and Cardou, A., 1989, “A Study of Helically Reinforced Cylinders Under Axially Symmetric Loads and Application to Strand Mathematical Modelling,” International Journal of Solid and Structures, Vol. 25, No 2, pp. 189-200.
9. Cardou, A. and Jolicoeur, C., 1997, “Mechanical Models of helical Strands,” Applied Mechanics Review, Vol. 50, No 1, pp. 1-14.

10. Chaplin, C.R and Tantrum, N., 1985, "The Influence of Wire Break Distribution on Stregth," Organisation Internationale pour l'Etude de l'Endurance des Cables (OIPEEC), Round Table Conference, June, Glasgow.
11. Chaplin, C.R., 1998, "Torsional Failure of Wire Rope Mooring Line During Installation in Deep Water," Engineering Failure Analysis, Vol. 6, pp. 67-82.
12. Chien, C.H. and Costello, G.A., 1985, "Effective Length of a Fractured Wire in Wire Rope," Journal of Engineering Mechanics, Vol. 111, No 7, pp. 952-961.
13. Cholewa, W., 1989, "Wire Fracture and Weakening of Wire Ropes," Wire Rope Discard Criteria: Round Table Conference: Swiss Federal Institute of Technology (ETH), Institute of Lightweight Structures and Ropeways, September, Zurich, Switzerland.
14. Costello, G.A., 1978, "Analytical Investigation of Wire Rope," Applied Mechanics Review, Vol. 31, No 7, pp. 897-900.
15. Costello, G.A., 1983, "Stresses in Multilayered Cables," Journal of Energy Resources Technology, Vol. 105, pp. 337-340.
16. Costello, G.A., 1990, Theory of Wire Rope, Springer-Verlag, New York, USA.
17. Davies, P., Grosjean, F., and Francois, M., 2000, "Creep and Relaxation of Polyester Mooring Lines," Offshore Technology Conference, OTC 12176, Houston, Texas, USA.
18. Del Vecchio, C.J.M., 1992, "Light Weight Materials for Deep Water Moorings," PhD Thesis, University of Reading, UK.
19. Fernandes, A.C., Del Vecchio, C.J.M. and Castro, G.A.V., 1999, "Mechanical Properties of Polyester Mooring Cables," International Journal of Offshore and Polar Engineering, Vol. 9, No 3, pp. 208-213.
20. Flory, J.F., 2001, "Defining, Measuring and Calculating the Change-in-Length Properties of Synthetic Fiber Rope," Ocean Conference Record (IEEE), Vol. 2, pp. 679-684.
21. Foster, G.P., 2002, "Advantages of Fiber Rope Over Wire Rope," Journal of Industrial Textile, Vol. 32, pp.67-75.

22. Ghoreishi, S., Messager, T., Cartraud, P. and Davies, P., 2004, "Assesment of Cable Models for Synthetic Mooring Lines," International Offshore and Polar Engineering Conference, Toulon, France.
23. Gjelsvik, A., 1991, "Development Length for Single Wire in Suspension Bridge Cable," Journal of Structural Engineering, Vol. 117, No 4, pp. 1189-1201.
24. Hankus, J., 1981, "Safety Factor for Hosting Rope Weakened by Fatigue Cracks in Wires," Organisation Internationale pour l'Etude de l'Endurance des Cables (OIPEEC), Round Table Conference, June, Krakow.
25. Hearle, J.W.S., 1969, "On the Theory of the Mechanics of Twisted Yarns," Journal of Textile Institute, Vol. 60, pp. 95-101.
26. Hobbs, R.E. and Raoof, M., 1982, "Interwire Slippage and Fatigue Prediction in Stranded Cables for TLP Tethers," Behavior of Offshore Structures, Vol. 2, pp. 77-99.
27. Holmes, M., 1995, Introduction to Perturbation Methods, Springer-Verlag, New York, USA.
28. Hooker, J.G., 2000, "Synthetic Fibre Ropes for Ultradeep Water Moorings in drilling and Production Applications," 2nd Offshore and Marine Technology, Singapore.
29. Hruska, F.H., 1951, "Calculation of Stresses in Wire Ropes," Wire and Wire Products, Vol. 26, pp. 766-767, 799-801.
30. Hruska, F.H., 1952, "Radial Forces in Wire Ropes," Wire and Wire Products, Vol. 27, pp. 459-463.
31. Hruska, F.H., 1953, "Tangential Forces in Wire Ropes," Wire and Wire Products, Vol. 28, pp. 455-460.
32. Huang, N.C., 1978, "Finite Extension of an Elastic Strand with a Central Core," Journal of Applied Mechanics, Vol. 42, No 4, pp. 852-857.
33. Jiang, W., 1995, "General Formulation on the Theories of Wire Ropes," Journal of Applied Mechanics, Vol. 62, pp. 747-755.
34. Jolicoeur, C., and Cardou, A., 1991, "A Numerical Comparison of Current Mathematical Models of Twisted Wire Cables Under Axisymmetric Loads," Journal of Energy Resources Technology, Vol. 113, pp. 241-249.

35. Jolicoeur, C., and Cardou, A., 1994, "Analytical Solution for Bending of Coaxial Orthotropic Cylinders," Journal of Engineering Mechanics, Vol. 120, No 12, pp. 2556-2574.
36. Jolicoeur, C., and Cardou, A., 1996, "Semicontinuous Mathematical Model for Bending of Multilayered Wire Strands," Journal of Engineering Mechanics, Vol. 122, No 7, pp. 643-650.
37. Karayaka, M., Srinivasan, S., Wang, S., 1999, "Advanced Design Methodology for Synthetic Moorings," Offshore Technology Conference, OTC 10912, Houston, Texas, USA.
38. Knapp, R.H., 1975, "Nonlinear Analysis of a Helically Armored Cable with Nonuniform Mechanical Properties," IEEE Ocean Conference, San Diego, California, pp. 155-164.
39. Knapp, R.H., 1979, "Derivation of a New Stiffness Matrix for Helically Armoured Cables Considering Tension and Torsion," International Journal for Numerical Methods in Engineering, Vol. 14, pp. 515-529.
40. Kumar, K. and Cocran, J.E., 1987, "Closed-Form Analysis for Elastic Deformations of Multilayered Strands," Journal of Applied Mechanics, Vol. 54, pp. 898-903.
41. Labrosse, M., Nawrocki, A. and Conway, T., 2000, "Frictional Dissipation in Axially Loaded Simple Straight Strands," Journal of Engineering Mechanics, Vol. 126, No 6, pp. 641-646.
42. Lagerstrom, P.A., 1988, Matched Asymptotic Expansions: Ideas and Techniques, Springer-Verlag, New York, USA.
43. Lanteigne, J., 1985, "Theoretical Estimation of the Response of Helically Armored Cables to Tension, Torsion and Bending," Journal of Applied Mechanics, Vol. 52, pp. 423-432.
44. Leech, C.M., 1987, "Theory and Numerical Methods for the Modeling of Synthetic Ropes," Communications in Applied Numerical Methods, Vol. 3, pp.407-713.
45. Leech, C.M., 2002, "The Modeling of Friction in Polymer Fibre Ropes," International Journal of Mechanical Sciences, Vol. 44, pp. 621-643.

46. Li, D., Miyase, A., Williams, J.G. and Wang S.S., 2002. "Damage Tolerance of Synthetic-Fiber Mooring Ropes: Small-Scale Experiments and Analytical Evaluation of Damaged Subropes and Elements," Technical Report, CEAC-TR-03-0101, University of Houston.
47. Linz, P., 1979, Theoretical Numerical Analysis: An introduction to Advanced Techniques, Dover Publications, New York, USA.
48. Lo, K.H., Xu, H. and Skogsberg, L.A., 1999, " Polyester Rope Mooring Design Considerations," International Offshore and Polar Engineering Conference, Brest, France.
49. Logan, J.D., 1997, Applied Mathematics, John Wiley & Sons Inc., New York, USA.
50. Love, A.E.H., 1944, Treatise on the Mathematical Theory of Elasticity, Dover Publications, New York, USA, Chap. 18.
51. Machida, S. and Durelli, A.J., 1973, "Response of a Strand to Axial and Torsional Displacements," Journal of Mechanical Engineering Science, Vol. 15, pp. 241-251.
52. Mandell, J.F., 1987, "Modelling of Marine Rope Fatigue Behavior," Textile Research Journal, June, pp. 318-330.
53. McConnell, K.G. and Zemke, W.P., 1982, "A Model to Predict the Coupled Axial Torsion Properties of ASCR Electrical Conductors," Experimental Mechanics, Vol. 22, pp. 237-244.
54. McKenna, H.A., Hearle, J.S.W. and O'Hear, N., 2004, Handbook of Fibre Rope Technology, Woodhead Publishing Ltd., Cambridge, England .
55. Najar, J., 1987, Continuum Damage Mechanics. Theory and Applications, Springer-Verlag, New York, USA.
56. Nawrocki, A. and Labrosse, M., 2000, "A Finite Element Model for Simple Straight Wire Rope," Computers and Structures, Vol. 77, pp. 345-359.
57. Nayfeh, A.H., 1973, Introduction to Perturbation Techniques, John Wiley & Sons Inc., New York, USA.
58. Phillips, J.W. and Costello, G.A., 1973, "Contact Stresses in Twisted Wire Cables," Journal of Engineering Mechanics Division, Vol. 99, pp. 331-341.

59. Ramsey, H., 1988, “A Theory of Thin Rods with Application to Helical Constituent Wires in Cables,” International Journal of Mechanical Sciences, Vol. 30, No 8, pp. 559-570.
60. Ramsey, H., 1990, “Analysis of Interwire Friction in Multilayer Cables Under Uniform Extension and Twisting,” International Journal of Mechanical Sciences, Vol. 32, No 9, pp. 707-716.
61. Raoof, M., 1991, “Wire Recovery Length in a Helical Strand under Axial-Fatigue Loading,” International Journal of Fatigue, Vol. 13, No 2, pp. 127-132.
62. Raoof, M. and Huang, Y.P., 1992, “Wire Recovery Length in Suspension Bridge Cable,” Journal of Structural Engineering, Vol. 118, No 12, pp. 3255-3267.
63. Raoof, M. and Kraincanic, I., 1995, “Recovery Length in Multilayered Spiral Strands,” Journal of Engineering Mechanics, Vol. 121, No 7, pp. 795-800.
64. Raoof, M. and Kraincanic, I., 1998, “Determination of Wire Recovery Length in Steel Cables and Its Practical Applications,” Computers & Structures, Vol. 68, pp. 445-459.
65. Reusch, F. and Estrin, Y., 1998, “FE-analysis of Mechanical Response of Simple Structures with Random Non-uniformity of Material Properties,” Computational Materials Science, Vol. 11, No 4, pp. 294-308.
66. Rungamornrat, J., Beltran, J.F. and Williamson E.B., 2002, “Computational Model for Synthetic-Fiber Rope Response,” 15th Eng. Mechanics Conference, ASCE, New York, USA.
67. Samras, R.K., Skop, R.A. and Milburn, D.A., 1974, “Analysis of Coupled Extensional-Torsional Oscillations in Wire Ropes,” Journal of Engineering Industry, Vol. 96, pp. 1130-1135.
68. Sathikh, S., Moorthy, M. and Krishnan, M. (1996), “Symmetric Linear Elastic Model for Helical Wire Strands Under Axisymmetric Loads,” Journal of Strain Analysis, Vol. 31, No 5, pp. 389-399.
69. Schrems, K. and Maclaren, D., 1997, “Failure Analysis of a Mine Hoist Rope,” Engineering Failure Analysis, Vol.4, No 1, pp.25-38.

70. Utting, W.S. and Jones, N., 1984, “A survey Literature on the Behaviour of Wire Ropes,” Wire Industry, pp. 623-629.
71. Velinsky, S.A., Anderson, G.L. and Costello, G.A., 1984, “Wire Rope with Complex Cross Sections,” Journal of Engineering Mechanics, Vol. 110, No 3, pp. 380-391.
72. Velinsky, S.A., 1985, “General Nonlinear Theory for Complex Wire Rope,” International Journal of Mechanical Sciences, Vol. 27, pp. 497-507.
73. Walton, J.M., 1996, “Developments in Steel Cables,” Journal of Constructions Steel Research, Vol. 39, No 1, pp. 3-29.
74. Ward, E.G., Ayres, R.R., Banfield, S., O’Hear, N. and Smith, C.E., 2005, “Experimental Investigation of Damage Tolerance of Polyester Ropes,” 4th International Conference on Composite Materials for Offshore Operations, Houston, Texas, USA.
75. Wempner, G., 1981, <u>Mechanics of Solids with Applications to Thin Bodies</u>, Sijthoof and Noordhoff, Rockville, Md.
76. Ward, E. G., Ayers, R. R., Banfield, S. J., O'Hear, N. (2006) “MMS and Joint Industry Project: Full Scale Experiments on Damaged Polyester Rope” Final Project Report prepared for Minerals Management Service and Joint Industry Project Participants, OTRC Library Number: 03/06JIP-FP-1.
77. Ward, E. G., Ayers, R. R., Banfield, S. J., O'Hear, N., Smith, C. E., Laurendine, T., (2006) “The Residual Strength of Damaged Polyester Rope”, Offshore Technology Conference, Houston, Texas, OTC Paper 18150.
78. Wu, H.C., 1993, “Frictional Constraint of Rope Strands,” Journal of Textile Institute, Vol. 84, No 2, pp. 199-213.